A MEASUREMENT OF THE PROTON ELASTIC FORM FACTORS FOR $1 \leq Q^2 \leq 3$ (GeV/c)^2

Thesis by

Robert Christian David Walker

In Partial Fulfillment of the Requirements

for the Degree of

Doctor of Philosophy

California Institute of Technology

Pasadena, California

1989

(Submitted February 20, 1989)

Dedicated to my family:

My father, William, who lead me;

My mother, Eleanor, who supported me;

My brother, Thomas, who guided me;

My sister, Diana, who lives through me.

Acknowledgments

This work would not have been possible without the help of a great many people. Special thanks goes to my thesis advisor, Dr. Brad Filippone, who spent hundreds of hours helping me through the experiment, data analysis, and writing of this thesis. His patience, dedication, and wisdom have shown me the best qualities a physicist can achieve. I would also like to thank the scientists and staff of the Kellogg Radiation Laboratory and SLAC Experiment E140 who made this experiment possible. In particular, the spokespersons for E140, Dr. Arie Bodek and Dr. Steve Rock, deserve credit for their many hours of help. Thanks also goes to Dr. Sridhara Dasu for his many contributions to the data analysis presented here. Dr. Dave Potterveld provided much of the software that assisted in writing this thesis, along with many helpful answers to my numerous questions over the years. Thanks to you all.

I would also like to thank my many friends, office mates, and room mates that I have had while at Caltech. Special thanks goes to Mike Hoenk, Tom Fric, and Doug Collins, who have provided many of the fond memories I take with me from Caltech. My love and gratitude also goes to Genesis Starr, who has greatly enriched my life here. My stay at Caltech could not have been as fulfilling without her friendship. My appreciation also goes to my "Pasadena parents," Shirley and John Fields, who gave me tremendous support and helped keep me sane.

Finally, I would like to thank my parents and family; for without their love and support none of this would have been possible.

Abstract

We report measurements of the proton form factors, G_E^p and G_M^p, extracted from elastic electron scattering in the range $1 \leq Q^2 \leq 3$ (GeV/c)^2 with uncertainties of <15% in G_E^p and <3% in G_M^p. The results for G_E^p are somewhat larger than indicated by most theoretical parameterizations. The ratio of Pauli and Dirac form factors, $Q^2(F_2^p/F_1^p)$, is lower in value and demonstrates less Q^2 dependence than these parameterizations have indicated. Comparisons are made to theoretical models, including those based on perturbative QCD, vector-meson dominance, QCD sum rules, and diquark constituents to the proton. A global extraction of the form factors, including previous elastic scattering measurements, is also presented.

Table of Contents

List of Figures

List of Tables

Chapter 1
Introduction

One of the fundamental problems addressed by nuclear and particle physics over the past 30 years is the underlying structure of the proton. It has been studied using both lepton and hadron probes of increasingly higher energy, leading to the quark/parton picture in force today. Elastic electron-proton scattering probes these constituents in a process which leaves them bound after the collision. The cross section for this process is described in terms of two functions, called the electric and magnetic form factors, G_E^p and G_M^p. At low momentum transfers, G_E^p is related to the Fourier transform of the proton charge distribution, while G_M^p contains information about its magnetic moment distribution. At large momentum transfers, the form factors give important information about the quark structure within nucleons, and therefore about the nature of the strong force at moderate inter-quark separation. It is this quality of the strong force which will be studied here.

1.1 Overview of Elastic Scattering

The Feynman diagram for elastic electromagnetic scattering of an electron from a spin-$\frac{1}{2}$ particle (proton) is shown to lowest order in α_{em} in Figure 1.1. The electron and proton, with initial four-momenta $\mathbf{p}$ and $\mathbf{P}$, respectively, exchange a single photon of momentum $\mathbf{q}$. The final state consists of the electron and proton with momenta $\mathbf{p}'$ and $\mathbf{P}'$, respectively. The requirements of momentum conservation at each vertex

and initial and final states that are on mass-shell for both the electron and proton give the constraints:

$$\mathbf{q}_\mu = \mathbf{p}_\mu - \mathbf{p}'_\mu \qquad \mathbf{P}'_\mu = \mathbf{P}_\mu + \mathbf{q}_\mu \tag{1.1}$$

$$\mathbf{p}_\mu \mathbf{p}^\mu = \mathbf{p}'_\mu \mathbf{p}'^\mu = m_e^2 \tag{1.2}$$

$$\mathbf{P}_\mu \mathbf{P}^\mu = \mathbf{P}'_\mu \mathbf{P}'^\mu = M_p^2 \tag{1.3}$$

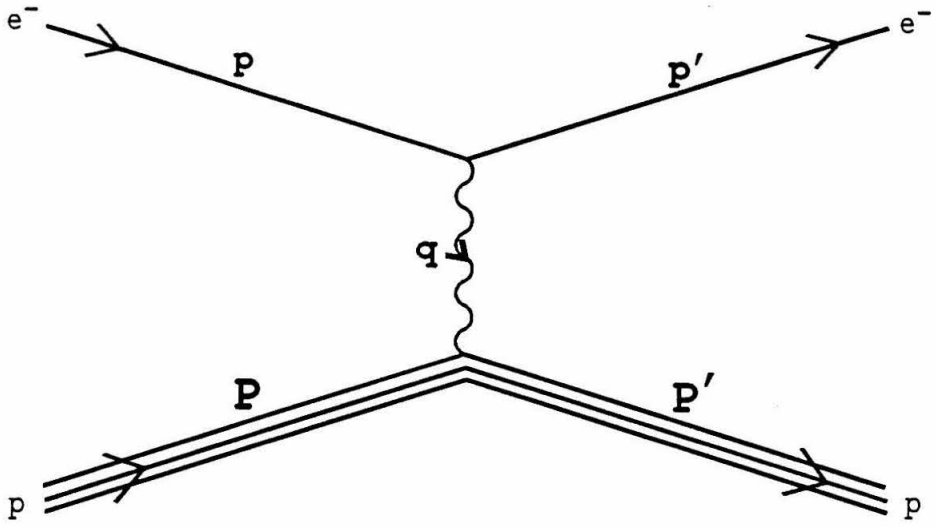

Figure 1.1 – Feynman diagram of elastic scattering of an electron from a proton in the single photon exchange approximation.

In the laboratory frame the electron has initial energy E_0, final energy E', and scattering angle θ; and the proton is initially at rest. If the mass of the electron is

ignored ($E_0 \gg m_e$, $E' \sin\theta \gg m_e$), the four momenta can be written:

$$\mathbf{p}_\mu = \begin{pmatrix} E_0 \\ 0 \\ 0 \\ E_0 \end{pmatrix} \qquad \mathbf{p}'_\mu = \begin{pmatrix} E' \\ 0 \\ E' \sin\theta \\ E' \cos\theta \end{pmatrix}$$
$$\mathbf{P}_\mu = \begin{pmatrix} M_p \\ 0 \\ 0 \\ 0 \end{pmatrix} \qquad \mathbf{P}'_\mu = \begin{pmatrix} M_p + \nu \\ 0 \\ -E' \sin\theta \\ E_0 - E' \cos\theta \end{pmatrix} \tag{1.4}$$

where $\nu \equiv E_0 - E'$ and the initial electron direction has been chosen along the z-axis with the final electron momentum in the y-z plane. The four momentum transfer squared, defined by $Q^2 \equiv -\mathbf{q}^2 \equiv \mathbf{q}_\mu \mathbf{q}^\mu$, is:

$$Q^2 = 4E_0 E' \sin^2(\theta/2) \tag{1.5}$$

and is completely determined by the electron kinematics. The constraint that the final hadronic state contains only a single proton, $W^2 \equiv \mathbf{P}'_\mu \mathbf{P}'^\mu = M_p^2$, leads to the equation:

$$x \equiv \frac{Q^2}{2M_p \nu} = 1 \tag{1.6}$$

This equation is again only a function of the electron kinematics and provides a relationship between the initial and final electron energy and scattering angle that is necessary in order to guarantee that a single proton, and nothing else, exists in the final hadronic state.

1.2 Derivation of Elastic Cross Section

The electron current is given by [1,2] :

$$j^{\mu} = -e\bar{\psi}(\mathbf{p}')\gamma^{\mu}\psi(\mathbf{p}) \tag{1.7}$$

where $\psi(\mathbf{p})$ is the wave function of an electron with four momentum $\mathbf{p}$. The proton current can be written as:

$$J^{\mu} = -e\bar{\Psi}(\mathbf{P}')\Big[F_1^p(Q^2)\gamma^{\mu} + \frac{\kappa_p}{2M_p}F_2^p(Q^2)i\sigma^{\mu\nu}\mathbf{q}_{\nu}\Big]\Psi(\mathbf{P}) \tag{1.8}$$

where the proton anomalous magnetic moment is $\kappa_p = \mu_p - 1 \approx 1.79$. Terms in the proton current that contain γ^5 are ruled out due to parity conservation, and a linear term in q^{μ} is ruled out by current conservation. The only invariant involved in the problem is Q^2, so F_1^p and F_2^p have been introduced as arbitrary functions of Q^2 only. These are called the Pauli and Dirac form factors, respectively, and they contain the information about the internal structure of the proton. The helicity-conserving scattering amplitude is described by F_1^p, while F_2^p describes the helicity-flip amplitude. They have been normalized at $Q^2 = 0$ to:

$$F_1^p(0) = F_2^p(0) = 1 \tag{1.9}$$

The differential cross section can be written [2] as:

$$\begin{aligned} d\sigma = |M|^2 &\frac{1}{4\Big((\mathbf{p}\cdot\mathbf{P})^2 - m_e^2M_p^2\Big)^{\frac{1}{2}}}(2\pi)^4\delta^4(\mathbf{p}'_{\mu} + \mathbf{P}'^{\mu} - \mathbf{p} - \mathbf{P}) \\ &\times\frac{d^3\mathrm{p}'}{(2\pi)^3 2E'}\frac{d^3\mathrm{P}'}{(2\pi)^3 2(M_p+\nu)} \end{aligned} \tag{1.10}$$

where the scattering amplitude M is related to the electron and proton currents [2] by:

$$\begin{aligned} T_{fi} &= -i \int j_\mu \Big(-\frac{1}{q^2}\Big) J^\mu d^4x \\ &= -i(2\pi)^4 \delta^4(\mathbf{p}' + \mathbf{P}' - \mathbf{p} - \mathbf{P}) M \end{aligned} \tag{1.11}$$

The differential cross section can be written in terms of the form factors, after integrating out the δ-functions that impose momentum conservation, as:

$$\begin{aligned} \frac{d^2\sigma}{d\Omega dE'} =& \frac{\alpha^2}{4E_0^2 \sin^4(\theta/2)} \frac{E'}{E_0} \Big[\Big(F_1^2 + \frac{\kappa_p^2 Q^2}{4M_p^2} F_2^2 \Big) \cos^2(\theta/2) \\ &+ \frac{Q^2}{4M_p^2} \Big(F_1 + \kappa_p F_2 \Big)^2 \sin^2(\theta/2) \Big] \delta\Big(E_0 - E' - \frac{Q^2}{2M_p} \Big) \end{aligned} \tag{1.12}$$

where the cross section has been averaged over initial spins and summed over final spins; *i.e.* an unpolarized beam and target have been assumed. (Note: the terms F_1 and F_1^p, etc., will be used interchangeably in order to avoid cumbersome notation, such as F_1^{p2}). The δ-function imposes the constraint that $x = 1$. Thus at fixed E_0 and θ the elastic cross section is a δ-function in E' and occurs at a value $E' = E'_{el} \equiv E_0 - Q^2/2M_p$.

The Sach's form factors, G_E^p and G_M^p, are defined in terms of F_1^p and F_2^p by:

$$G_E^p(Q^2) \equiv F_1^p(Q^2) - \kappa_p \tau F_2^p(Q^2) \tag{1.13}$$

$$G_M^p(Q^2) \equiv F_1^p(Q^2) + \kappa_p F_2^p(Q^2) \tag{1.14}$$

$$\tau \equiv \frac{Q^2}{4M_p^2} \tag{1.15}$$

Note the normalizations of $G_M^p(0)=\mu_p$ and $G_E^p(0)=1$. These are referred to as the electric and magnetic form factors, respectively, because in the non-relativistic limit

they can be related [2] to the Fourier transforms of the charge and magnetic moment distribution of the proton. If equation 1.12 is integrated over E', the elastic cross section is:

$$\frac{d\sigma}{d\Omega} = \left(\frac{d\sigma}{d\Omega}\right)_{mott} \frac{E'}{E_0}\left(\frac{G_E^2 + \tau G_M^2}{1+\tau} + 2\tau G_M^2 \tan^2(\theta/2)\right) \tag{1.16}$$

$$= \left(\frac{d\sigma}{d\Omega}\right)_{mott} \frac{E'}{E_0}\frac{1}{1+\tau}\left(G_E^2 + \frac{\tau}{\varepsilon}G_M^2\right) \tag{1.17}$$

$$\left(\frac{d\sigma}{d\Omega}\right)_{mott} \equiv \frac{\alpha^2 \cos^2(\theta/2)}{4E_0^2 \sin^4(\theta/2)} \tag{1.18}$$

where $\varepsilon = (1+2(1+\tau)\tan^2(\theta/2))^{-1}$ is the longitudinal polarization of the virtual photon

1.3 Experimental Goals

There are two properties about the previous equation that should be noted. The first is the existence of the kinematic variable τ that multiplies G_M^2 relative to G_E^2. When $\tau \ll 1$ (small Q^2), the cross section is dominated by G_E^p, but for $\tau \gg 1$, G_M^p dominates. This Q^2 dependence is related to the fact that the magnetic force ($\sim 1/r^3$) dominates at short distances relative to the electric force ($\sim 1/r^2$). Since it is the large Q^2 regime that is of interest here, G_E^p is relatively more difficult to extract from the cross sections than G_M^p.

The second thing of interest is the existence of the $\tan^2(\theta/2)$ term that multiplies G_M^2 but does not multiply G_E^2. If several measurements of the elastic cross section are performed at fixed Q^2 but different θ, it is possible to extract both $G_E^p(Q^2)$ and $G_M^p(Q^2)$; this is called a Rosenbluth separation.

Since G_E^p is only a small contribution to the cross section at large Q^2, uncertainties in the measured cross sections are magnified into larger fractional uncertainties in G_E^2. In order to limit the uncertainties in G_E^p, the following goals are the most important to achieve:

• Maximizing the range in θ of the cross section measurements at each value of fixed Q^2.

• Limiting the statistical uncertainties in $d\sigma/d\Omega$.

• Limiting random systematic fluctuations in $d\sigma/d\Omega$.

• Limiting the systematic uncertainties correlated with θ at fixed Q^2. This means limiting any systematic uncertainties correlated with E_0, E', θ, beam current, cross section magnitudes, time, etc., since all of these quantities change when θ is changed at a fixed value of Q^2.

It was this last point that was the most important in this experiment. Previous measurements [3,4] of G_E^p in this Q^2 regime were frequently dominated by systematic uncertainties. These were usually due to uncertainties in normalization between data taken at different laboratories, or normalizations between different small and large angle spectrometers. Improvements made to the Stanford Linear Accelator Center (SLAC) beamline and detectors in End Station A, in order to perform a Rosenbluth separation of deep inelastic scattering cross sections [5-7], made it possible to substantially reduce the systematic uncertainties in the elastic cross sections measurements. These improvements included precise measurements of the incident beam energy and angle and an understanding of the spectrometer acceptance over a wide range of E'. A single spectrometer was rotated around the target pivot to measure cross sections at a wide variety of angles, including intermediate angles as a check on systematic effects. The deep inelastic scattering experiment [5] which was scheduled to be performed in End Station A required that elastic scattering data be taken to calibrate the incident beam energy ($E_0 = E' + Q^2/2M_P$ at the elastic peak) as an additional technique to reduce systematic uncertainties. This is the data presented here. With a relatively small investment of time (the data presented here represents

$\approx$ 5 days of beam time), substantial improvements over previous elastic scattering measurements were possible, along with precise calibrations of the experimental apparatus.

Chapter 2
Experimental Apparatus and Data Acquisition

2.1 Upstream Beam System

Electron pulses from both the Main Injector and the Nuclear Physics Injector (NPI) at SLAC [8] were used in this experiment. The Main Injector is located at the beginning of the beamline approximately 2 miles from the experimental hall, utilizing all 30 "sectors" of the linac to deliver the maximum electron energy. Energies of between 1-21 GeV can be achieved with peak currents $\leq$ 40 mA. At the lower energies ($<$ 6 GeV), the peak current is reduced due to the effects of beam breakup along the accelerator line. The NPI [9] was installed to provide high current beams at these lower energies and is located 6 sectors from the linac exit. It can provide beams of $\approx$ 40 mA peak current with energies between 0.65 and 4.5 GeV, and was therefore used at beam energies $\leq$ 4.25 GeV. The Main Injector was used at the higher energies. Beam pulses were typically 1.6 μs in width and were operated at between 60-90 pulses per second (PPS).

The beam was directed into the "A-line" (Figure 2.1) for delivery to the experimental hall, End Station A (ESA), by the beam operators at SLAC's Main Control Center (MCC). The energy of the beam was defined in the "A-bend"; a set of eight identical dipole magnets that bent the beam in a horizontal plane (B10-B17). A set of slits (SL10 & SL11) then allowed only those electrons within the proper energy range to pass. By changing the width between the slits, the energy spread of the beam, which ranged from 0.1%-0.3% full width in this experiment, could be altered.

An additional identical dipole magnet, in series with the others, was maintained at MCC separate from the beamline. A rotating flip-coil was located at the nominal beam position inside this magnet and continuously monitored the field strength. The beam energy at the center of the A-bend slits was calculated and checked every few seconds, and its value was recorded on magnetic tape every few minutes. Additional quadrupole magnets were located in the A-bend and were used to minimize the beam spot size and divergence at the target position in ESA.

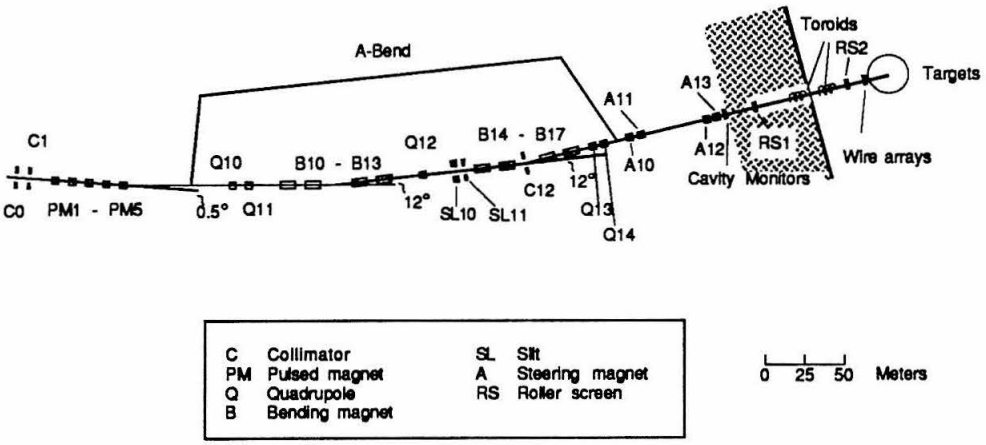

Figure 2.1 – Diagram of the A-line system used to transport the beam to ESA. The scale on the right is only approximate.

It was the responsibility of the experimenters to perform the final steering of the beam to the target. This was accomplished by sending the beam through two sets of vertical and horizontal bending dipole steering magnets (A10-A13) after it left

the A-bend. The first set of magnets was located $\approx$ 99 m upstream of the target; the second set was located $\approx$ 53.5 m upstream. A set of two resonant microwave cavities were located immediately following the second set of magnets to measure the horizontal and vertical beam position. Two secondary emission wire arrays were located in the beam path $\sim$ 1 m upstream of the target. One wire array had its wires oriented in the vertical direction, the other in the horizontal. The wires were made of pure aluminum 0.13 mm in diameter and were spaced 0.4 mm apart. An LSI minicomputer continuously monitored the beam position at the cavity monitors and wire arrays throughout the experiment. This computer also controlled the current to a set of smaller auxillary coils (trim coils) around the steering magnets and maintained the beam along the nominal beam axis continuously throughout the data taking. The beam steering system was calibrated after every energy change so the computer could properly adjust the current in the trim coils. Two zinc-sulfide (ZnS) roller screens, separated by $\sim$ 10 m, were located upstream of the target in ESA and could be rotated into the beamline at low beam pulse rates between data runs. The beam position could be observed on these roller screens by the experimenters through remote TV cameras. A ZnS target could also be inserted at the target position to allow the beam position to be observed. Thus the experimenters could confirm that the beam transport system was operating properly.

The total amount of incident charge in the beam was measured with a set of two identical ferromagnetic toroidal charge monitors placed around the beamline $\sim$ 10 m upstream of the target. When a pulse of electrons passed through the toroids, a time varying magnetic field was produced inside the ferromagnetic core. A wire was wrapped several times around the core and connected to an RC-circuit. A current was induced in this wire by the magnetic flux in the toroid and a damped resonant signal was created in this effective RLC-circuit with an amplitude proportional to the

total charge in the beam pulse. The RLC time constant was large compared to the width of a beam pulse. The output of the RC circuit was connected to a preamp located in a shielded box along the beamline $\sim$ 0.5 m from the toroid to minimize noise in the system.

The output signal from the preamp was carried from ESA to Counting House A (CHA) where the electronics, experimenters, and computers for this experiment were located. There the signal passed through another set of amplifiers and the amplitude was measured by two different electronic circuits (see Figure 2.2). To allow for the wide range of beam currents measured, the gain of the amplifiers was altered over a range from 1-100. The first and original circuit measured the value of the signal after a time delay from the start of the beam pulse. This time delay was chosen to minimize sensitivity to the width of the beam pulse. The second and more recently installed circuit integrated the signal over the second half period. Before the experiment began, the starting and stopping times of this integration were set to minimize the sensitivity to the width of the beam pulse and drifts in the timing circuit.

The toroids were calibrated by sending a pulse of charge through a wire that passed through the toroids (Figure 2.2). A capacitor, whose capacitance was measured before the experiment to an accuracy of 0.1%, was charged to a nominal voltage with a digital-to-analog converter (DAC) and was then discharged through the wire. An additional attenuator circuit was located near the toroids and could be remotely set to values of $\div 1, \div 10$, or $\div 100$, to allow for either large or small beam currents to be simulated. The resulting signal of the toroids was measured and the relationship between the incident charge and signal pulse height could be determined. A separate calibration system was used for each toroid, but occasionally the calibrators were temporarily switched so a cross calibration of the toroids could be performed. This

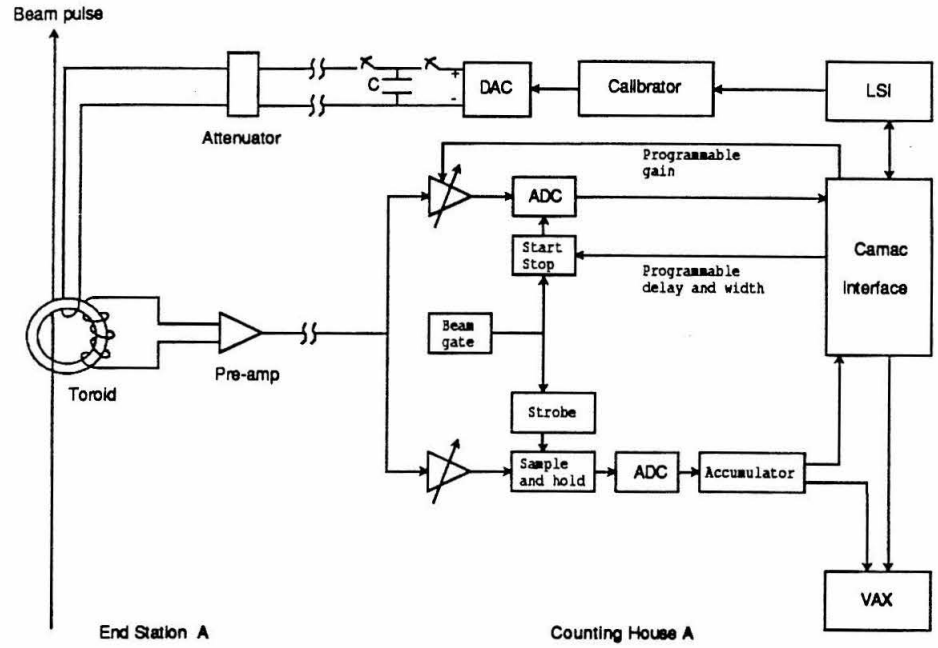

Figure 2.2 – The toroid circuit used to measure the incident charge. Both calibration and readout circuits are shown. Two independent, identical such systems were used in this experiment.

system was used to monitor any changes in the toroid system caused by temperature fluctuations, drifts in the amplifier gains, and shifts in the timing. Calibrations were done between data runs, which was typically every few hours. The calibrations were performed at gain and attenuator settings that roughly corresponded to the beam currents being used at that time of the experiment. Additional calibration runs were taken periodically at a variety of gains, DAC voltages, attenuator values, and output gain amplifier settings. These measured the linearity of the output circuit and checked for any changes in the calibration capacitors, DACs, or attenuators.

Beam quality was monitored with two plastic scintillators mounted with photo-tubes in ESA. One scintillator was mounted along the beam pipe upstream from the

target and was used to measure the "bad spill" caused by the beam halo. The second scintillator was placed $\sim$ 10 m from the target at a scattering angle of $\sim$ 70° and measured the time structure of the beam ("good spill"). An oscilloscope displayed the anode signals which were monitored by MCC as diagnostic tools in tuning the beam. Analog-to-Digial Converters were also used to measure the spill monitors and were recorded on magnetic tape. Ideally the "bad spill" was kept near zero while the "good spill" had a square wave structure 1.6 μs in width to minimize dead-time effects and energy fluctuations.

2.2 Targets

A cylindrical liquid hydrogen target (LH2) 20 cm in length [10] and 5.08 cm in diameter (Figure 2.3) with side walls, entrance, and exit windows made of 0.076 mm aluminum was used to scatter electrons for this experiment. An identical, empty dummy cell (DUM) with an additional 1.16 mm of aluminum radiator added to both the entrance and exit windows was used to measure endcap contributions to the scattering. Additional aluminum was added to make the radiation length of the empty cell roughly equal to that of the hydrogen cell, and to increase the scattering rate from the empty cell. A detailed list of the target materials and dimensions is presented in Appendix A.

Liquid hydrogen at 21°K and a pressure of 2 atm continuously flowed through the LH2 target. Heat deposited by the beam was removed by circulating the hydrogen through a heat exchanger with a liquid hydrogen bath. Contamination levels within the hydrogen were measured by mass spectroscopy to be $\approx$ 0.16% deuterium, $<$ 0.37% H_2O, and $\leq$ 0.1% other contaminants (per molecule). A liquid nitrogen cold trap filtered out any water from the gaseous hydrogen before it was liquefied and circulated into the target circulation system. A 4 cm diameter aluminum tube 0.025 mm thick

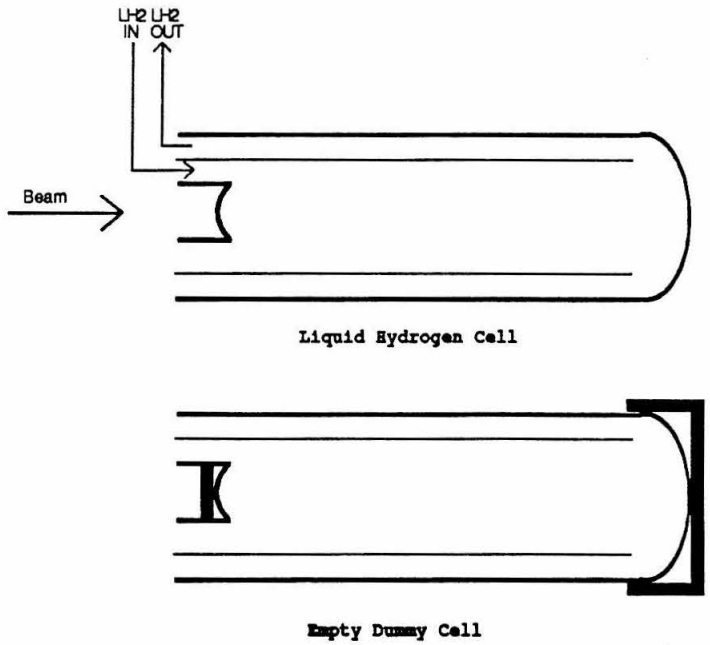

Figure 2.3 – The liquid hydrogen and dummy targets. Note the flow of the liquid hydrogen. Additional radiators were placed over the entrance and exit endcaps of the dummy cell.

was contained within the cell and was used as a flow guide. The hydrogen flowed into the target inside this flow guide and exited between the flow guide and the outer target wall. Circulation of the hydrogen was maintained by fan-like pumps at a flow rate $\gtrsim 1$ m/s. During part of the experiment the flow direction of hydrogen through the cell was accidentally reversed. The effects of this reversed flow are discussed in detail in Appendix C.

Vapor pressure bulbs and platinum resistors were located at the entrance and exit of the flow guides to measure the hydrogen temperature and pressure. The ingoing and outgoing hydrogen density was calculated from these measurements, and was monitored every 10 sec.

These targets, along with other deuterium and solid targets [11], were mounted on a remotely controlled carousel that could be moved vertically and rotated in a horizontal plane to place any desired target into the beam line. This assembly was contained under vacuum within a scattering chamber that was an aluminum cylinder with 2.54 cm thick walls, with entrance and exit windows as described below. An additional stack of lead shielding $\sim$ 20 cm thick surrounded the chamber in most places to minimize the amount of radiation escaping the target area into the ESA.

The beam entered the scattering chamber through a 5-in circular aperture made of 0.025 mm aluminum that isolated the chamber vacuum from the beamline vacuum. An extended snout attached to the scattering chamber allowed for electrons scattering at angles $\lesssim 50^\circ$ to exit the chamber through a thin 0.31 mm exit window. It also allowed the beam to exit the scattering chamber far enough downstream so that no electrons could scatter from the exit window into the spectrometer acceptance. The entire scattering chamber was mounted on a $\sim$ 8 ft diameter pivot area in ESA around which the spectrometer rotated. The targets were located directly above the center of the pivot along the beam line.

2.3 Spectrometer

After the electrons scattered from the target, they were detected in the 8 GeV spectrometer [12,13] in the ESA (Figure 2.4). Electrons were focused and momentum selected by a series of three quadrupole and two vertical-bend dipole magnets. Immediately after the last quadrupole magnet was a lead-shielded hut in which the particle detectors were located. The spectrometer could be rotated around the target pivot on a circular track to allow only those electrons which had scattered at the desired angle to reach the detectors.

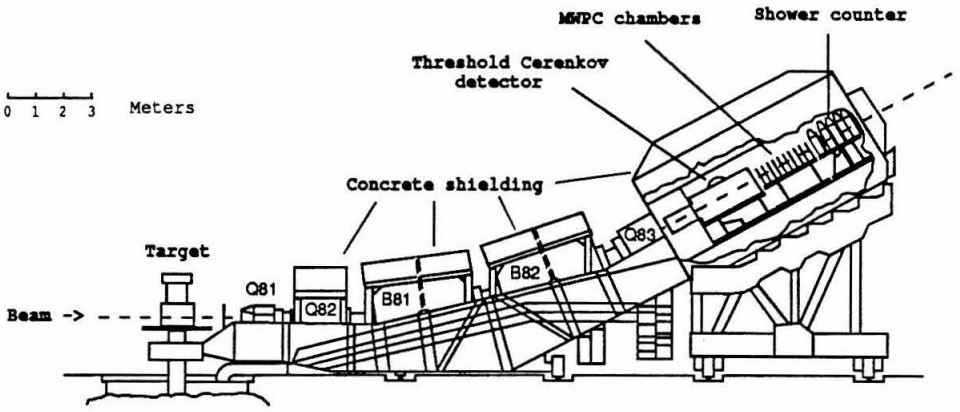

Figure 2.4 – The 8-GeV spectrometer.

The magnets of the spectrometer were tuned to focus particles with momentum E' and final angle θ to vertical and horizontal positions, respectively, in the detector hut (Figure 2.5). Measurements of the position of the particle track at the two focal planes, one plane for E' (also referred to as P for momentum) and one for θ, could be transformed, to first order, to a measurement of E' and θ. The slope of the track through these focal planes also yielded a measurement of the out-of-plane angle, ϕ, and the horizontal position along the spectrometer entrance window, X_{SP8}, of the particle trajectory at the target. The spectrometer had an acceptance of roughly $\pm 4\%$ in $\Delta P/P_0$, ± 8 mr in $\Delta\theta$, ± 30 mr in $\Delta\phi$, and ± 12 cm in X_{SP8}. Central values of $1 \leq E' \leq 8$ GeV and $11.5° \leq \theta \leq 48°$ were used in this experiment.

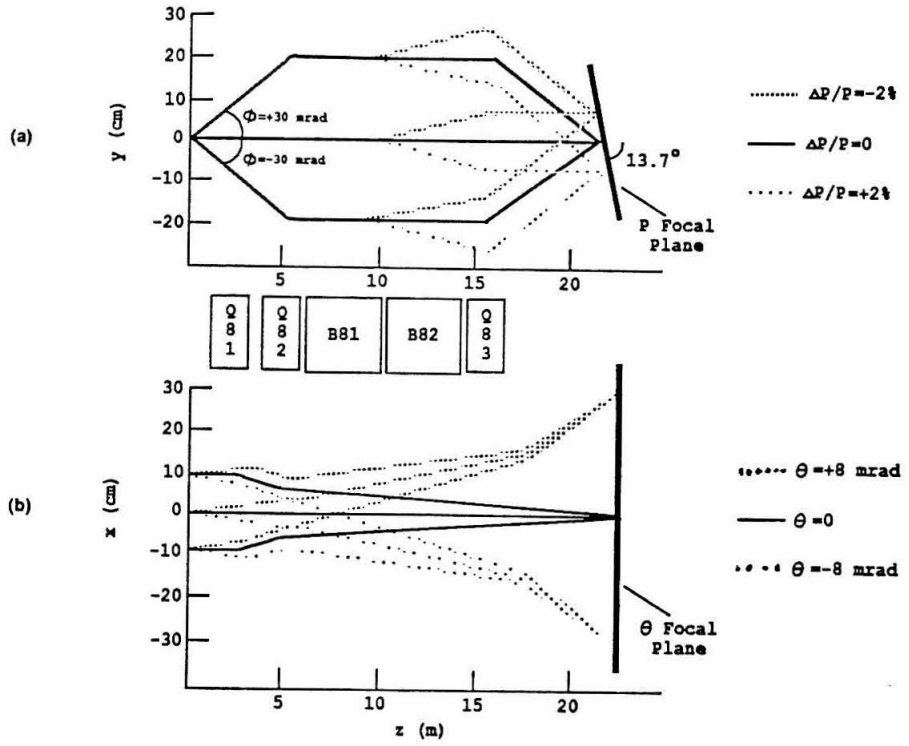

Figure 2.5 – The (a) E' and (b) θ focal properties of the 8-GeV spectrometer.

Optical properties of the spectrometer were previously measured [14,15] in 1967 using a dark current electron beam from the accelerator with the spectrometer set at an angle of 0° with respect to the beam axis. Any changes in the optical properties of the spectrometer over the range of momenta used needed to be well understood to eliminate systematic errors correlated with E'. Wire orbit measurements [16,17] were done from $0.5 \leq E' \leq 9$ GeV to calibrate the central ray of the spectrometer and to check for an E'-dependence to the transport coefficients. Results of the wire orbit study are presented in the Appendix B (E' calibration) and in the section on Acceptance in Chapter 3 (transport studies).

2.4 Detectors

The detector package was designed to detect electrons with > 99% efficiency and reject pions to one part in 10^5. It was also required to measure both the position and angle of the particle tracks to ± 2 mm and ± 1 mr, respectively, at the E' and θ focal planes. These constraints were achieved with three essential elements: a hydrogen-filled threshold Čerenkov counter, a set of ten multiwire proportional chambers, and a Pb-glass total absorption array (Figure 2.6). Three sets of plastic scintillators were also included to add to the spatial segmentation of the detectors, to be used as fast trigger elements, and to assist in pion identification and rejection.

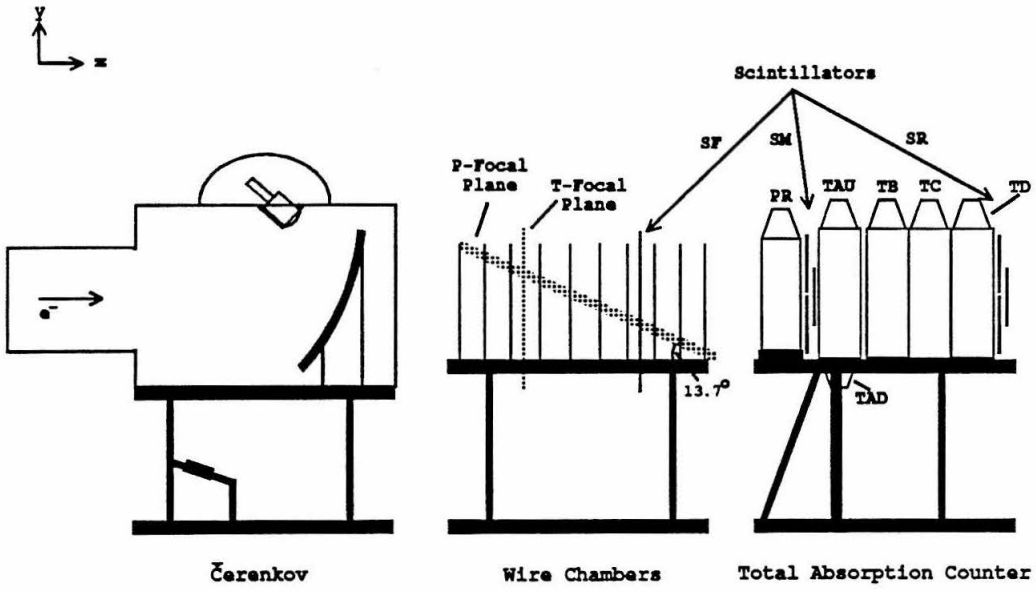

Figure 2.6 – The particle detector elements located in the 8-GeV spectrometer.

2.4.1 Čerenkov Counter

The Čerenkov counter entrance window was located at the end of the last quadrupole magnet of the spectrometer and was made as thin as possible to minimize the probability of pions causing "knock-on's" – electrons above the Čerenkov energy threshold that pions elastically scatter out of the aluminum window. The entrance and exit windows were made from aluminum and were 0.41 mm thick. The counter was 3.30 m long and was filled with hydrogen at atmospheric pressure with an index of refraction of 1.000140 [18]. Threshold energies for electrons and pions were 0.031 GeV and 8.4 GeV, respectively. Hydrogen gas was chosen to minimize the probability of pions producing knock-on's within the gas itself or creating scintillation light that could mimic an electron Čerenkov signal. It also contributed very little to the multiple scattering of the electrons and thus improved the resolution of the momentum and angle measurements, especially at low E'.

Some of the Čerenkov radiation emitted by electrons appeared in the ultraviolet spectrum. Emphasis was therefore placed on eliminating oxygen in the counter since oxygen absorbs ultraviolet light. The Čerenkov counter was purged weekly by evacuating to < 5 mm Hg pressure, filling with nitrogen, evacuating again, and refilling with hydrogen. Leaking of oxygen through the edges of the phototube face and the rubber O-ring against which it rested was limited by over-pressurizing the Čerenkov hood to 1.5 atm with nitrogen.

A curved mirror 53 by 90 cm in area was located 315 cm from the entrance window and was used to focus the Čerenkov radiation onto the face of a RCA 8854 phototube located at the top of the counter. The mirror was aluminum with a 0.64 cm backing of lucite and was resurfaced with a layer of MgF_2 to eliminate oxidation on the surface. It was aligned within the counter with a laser to insure that the

Čerenkov light was properly focused onto the phototube face. A wavelength shifter was applied to the face of the phototube to increase its sensitivity to the ultraviolet. The output pulse of the phototube was shortened to 20 ns by placing a 5 ns delay clip line on the anode output that was terminated by a 6 db attenuator.

2.4.2 Wire Chambers

Following the Čerenkov counter were ten planes of multiwire proportional chambers [19](Figure 2.7). The wires were made of 20 μm gold-plated tungsten and were spaced at 2 mm intervals. A "magic-gas" mixture of 65.75% argon, 30.00% isobutane ($(CH_3)_2CHCH_3$), 4.00% dimethyl acetal formaldehyde ($CH_2(0CH_3)_2$), and 0.25% bromotrifluoromethane ($CBrF_3$) continuously flowed through the chambers. The gas was contained within the chambers by windows made of 0.0762 mm of mylar coated with 0.0762 mm of aluminum. The typical operating voltage of the two cathode planes was 3.6 kV, with gaps between the anode wires and the planes of 4 mm in both directions. The catode planes were made of 0.051 mm of mylar coated with 0.0075 mm of aluminum. The chambers had an active region 35 cm in height and 93 cm in width, and spanned 1.81 m in the direction of the particle trajectory.

Chambers were numbered from one to ten sequentially along the direction of the scattered electrons. Even numbered chambers had wires oriented along the horizontal direction to measure the vertical track position. These were called "P-chambers" since they were used to measure the particle momenta. There were a total of 176 wires in each of these chambers. A vertical teflon support wire near the center of the chambers suspended the wires to keep them from sagging. This wire caused a $\sim$ 2 cm wide dead region near the center of each P-chamber. Staggering of the support wires guaranteed that no particle track could cross more than two of these dead areas. Chambers 1, 5 and 9 had the wires oriented at $-30°$ from the vertical; chambers 3 and 7 were

oriented at +30° (viewed along the particle trajectory). These chambers measured the horizontal track position in addition to including redundancy, so that multiple tracks could be identified and separated, and were called "T-chambers" (for theta). They contained 480 wires with 2 mm spacing; however, the wires were electrically tied together in pairs so effectively 240 wires with a 4 mm spacing were used. The spectrometer E' and θ focal planes were contained within the chamber area, as shown previously in Figure 2.6.

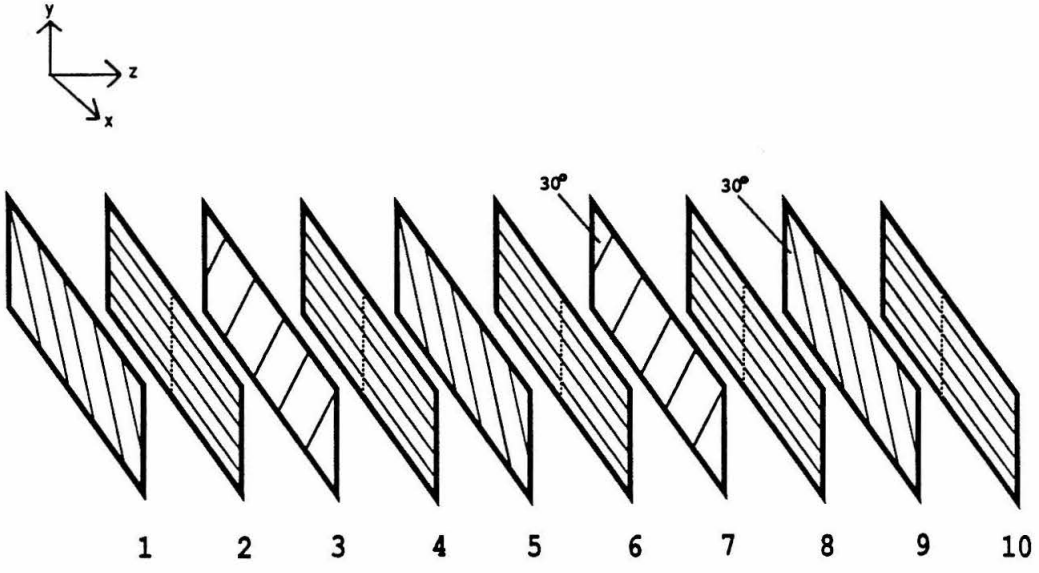

Figure 2.7 – The orientation of the wires in the wire chambers. The support wires in the P-chambers are shown.

2.4.3 Total Absorption Shower Counter

The Pb-glass total absorption counter is shown in Figure 2.8. It was segmented both in the horizontal direction and along the particle trajectory. Electrons incident on the Pb-glass have a high probability of emitting bremsstrahlung photons which then convert into e^+e^- pairs. These pairs will create more hard photons that create more pairs, resulting in an electromagnetic shower. Electrons and positrons will also create Čerenkov radiation which is detected by the phototubes mounted on the Pb-glass. Pions that enter the Pb-glass do not have a high probability of creating an electromagnetic shower because of their high mass. Instead, the hadronic showers they create will deposit only a portion of the pion's energy in the counter, and it will be deposited further towards the back of the counter, allowing for discrimination between pions and electrons.

The first row of six F2-type Pb-glass blocks [20] were made of 45% SiO_2, 45% PbO, 6% K_2O, and 3% Na_2O, and were used as a pre-radiator (PR) to start the electromagnetic shower before the electrons entered the rest of the counter. These blocks had a radiation length of 3.22 cm, a refractive index of 1.62, and were 32 cm tall, 15.8 cm wide and 10.4 cm thick (=3.2 r.l.). Aluminum blocks supported them 4 cm off the mounting table so they were vertically centered with the other taller Pb-glass blocks used in the other rows. The maximum particle trajectory angle in the spectrometer was $\pm 2.5°$ from the central axis, so the PR row was rotated by 5° around the vertical to eliminate the possibility of particles passing through the cracks between the blocks. XP 2041 phototubes were placed at the top of the blocks to detect Čerenkov radiation from the electromagnetic showers.

The next 4 rows of SF5-type Pb-glass [21] were 40 cm high, 14.6 cm wide, and 14.6 cm thick (=6.8 r.l.). The first three rows had 7 blocks, the last row had 6.

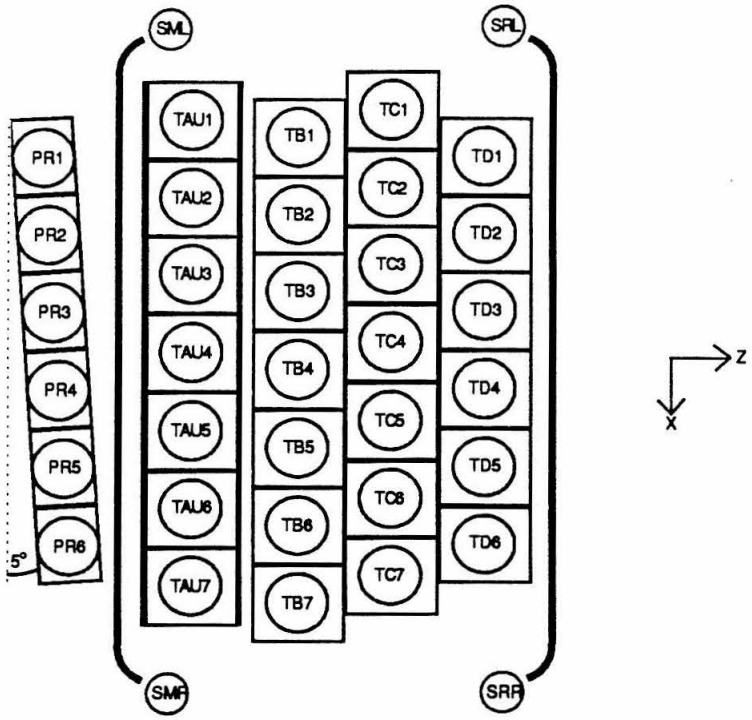

Figure 2.8 – The Pb-glass total absorption counter. Two of the rows of scintillators are also shown.

Each row was staggered relative to the next so that the cracks between the blocks did not overlap. Phototubes were placed on the top of each block. Since the shower maximum occurred near the first row of blocks, an additional phototube was placed on the bottom of each of these blocks to maximize the shower detection efficiency and resolution. The rows were labeled TA, TB, TC and TD, from front to back; the top and bottom phototubes in the first row were called TAU and TAD, respectively. Individual phototubes were numbered 1-7 (or 1-6) from left to right when viewed along the particle trajectory. Clip lines were also placed on these phototubes to limit the signal pulses to 20 ns. The total thickness of the shower counter was 30.4 r.l. The FWHM resolution of the Pb-glass array was found to be $18\%/\sqrt{E'}$.

2.4.4 Plastic Scintillators

Plastic scintillators were used to detect all minimum ionizing particles. One row of 6 vertical scintillators were located between wire chambers 7 and 8. Three horizontal scintillators were located between the shower rows PR and TA. These provided additional vertical segmentation to the detectors. A particle that created a shower in the PR would also give a larger pulse height in these scintillators than a single minimum ionizing particle would. This increased the detector's electron efficiency and pion rejection. A final set of three horizontal scintillators were located behind TD. These scintillators would detect those pions or muons that transversed the entire shower counter, while electrons would be totally absorbed in the counter. The three sets of scintillators were labeled SF, SM and SR, respectively.

2.5 Electronics

2.5.1 Fast Electronics

Raw detector signals from the phototubes on the detectors were carried to the electronics in the CHA $\sim$ 100 m away by fast heliax cables (for trigger components) or regular coaxial cables (for other components). Pulses from each of the wires in the wire chambers were amplified, discriminated, and fed into a dual 450 ns delay flip-flop circuit. This delayed signal could be latched into a bit register by a coincident "fast-latch" signal $\sim$ 75 ns from the event trigger to record the pattern of "hits" in the wire chambers. Commercially available CAMAC and NIM modules were used for the electronics in CHA. Attenuators were used to reduce by 50% the signals from the shower counter rows PR, TAU, TAD and TB at $E' > 4$ GeV to keep the signals from saturating the electronics at large momenta but still have reasonable resolution at small momenta.

A simplified schematic of the electronics is shown in Figure 2.9. The electronic signals were divided using linear fan-out components. One output of the fan-outs went to a set of Analog-to-Digital Converters (ADC's) to record pulse height information. The other output was fed through discriminators to the trigger logic and other electronic elements; the discriminator threshold settings are given in Table 2.1. The outputs of the discriminators were 0.7 V pulses with widths of 20 ns. These pulses were sent to scalers, fast latches, and as stop gates to Time-to-Digital Converters (TDC's). In addition, the raw signals of individual components in each "row" of counters (SF1-6, PR1-6, TAD1-7, etc.) were linearly added together to form single pulses for each row (SF, PR, TAD, etc.). These pulses went to ADC's and discriminators; then to scalers, latches, and TDC's. The trigger components (Č, SF, SM, PR, TAD) were also sent to a fast trigger circuit to generate a trigger pulse.

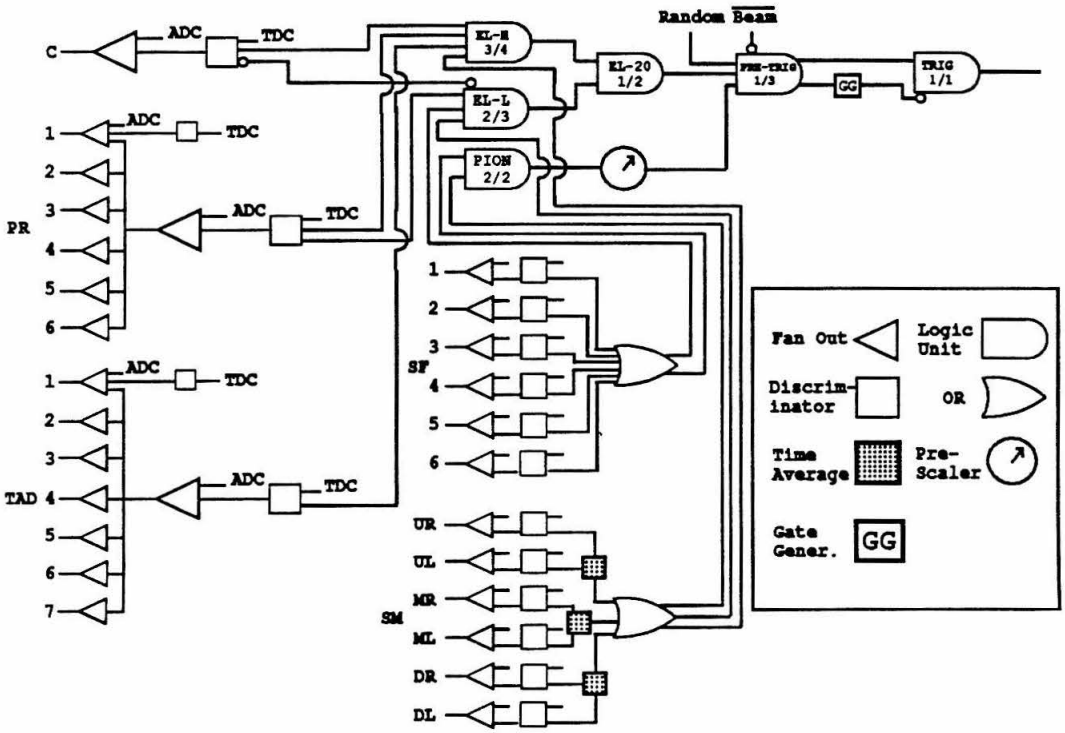

Figure 2.9 – A simplified diagram of the electronics used.

Component	Discriminator (mV)
Č	40
SF	40
PR	60
SM	40
TAU	60
TAD	60
TB	30
TC	40
TD	40
SR	40

Table 2.1 – The discriminator threshold settings for the various detector components.

2.5.2 Trigger

The trigger was designed to fulfill several different purposes. It was necessary that it be more than 99.9% efficient for electrons over the entire range of momenta measured, $1 \leq E' \leq 8$ GeV. Deep inelastic data [11] that was taken in parallel with this experiment was run with π/e backgrounds of up to 100:1; thus the trigger needed to have a pion rejection of $> 99\%$ to keep the trigger rate from being dominated by background pion events. Pion backgrounds were not significant for the elastic data presented here, however. It was also of interest to have a limited measurement of the detector response to pions so the detector performance could be better understood.

There were three basic components to the trigger. Electron High (EL-H) was composed of a 3-out-of-4 (3/4) coincidence between Č, PR, SM, and TAD. Each of these components had a high efficiency for electrons at high momenta. Since none of the components was absolutely required, this combination had a very high efficiency

for electrons. Č, PR and TAD also had good rejection of pions, so pion backgrounds did not significantly effect the trigger rate. However, at low momenta the electron shower in the shower counter was sometimes contained within the PR row of lead glass, and the EL-H trigger was effectively reduced to a 3/3 coincidence of Č, PR and SM, with a corresponding reduction in efficiency. Electron Low (EL-L), which consisted of 2/3 of PR, SF and SM in coincidence with Č, was instituted to give increased efficiency at low momenta. The inclusion of SF instead of TAD increased the electron efficiency to acceptable levels, and the absolute requirement of Č made the trigger insensitive to pions. A logical OR of these two triggers (EL-H and EL-L) was formed to create the electron trigger (EL-20).

During the time of the trigger pulse (20 ns), the electronics were not able to accept additional events. In order to measure the effect of this dead-time on the trigger rate, additional pulses (EL-40, EL-60, and EL-80) were formed that were identical to EL-20 except for a longer pulse width (40, 60, and 80 ns, respectively). The ideal trigger rate for a pulse width of 0 ns could be deduced from an extrapolation of the scaler rates of these pulses. A backup measurement of the electronics dead-time was included by creating signals that were a 3/3 coincidence of PR, TAD, and Č (PTC-20, PTC-40, PTC-60, PTC-80).

Another component of the trigger was added to systematically measure the pion background without a significant increase in the dead-time. A coincidence of SF and SM was formed, referred to as PION, that was efficient for any minimum ionizing particle passing through the detector package. This signal was then pre-scaled by a factor of 2^8 (PION-PRE) and included in the trigger. Pre-scaling kept this component from contributing significantly to the dead-time. These events were only used for studying the detector response to pions.

A random pulse generator signal (RANDOM) fired approximately every 10 sec and was also included to monitor the pedestals of the electronics components. The coincidence of any of the three trigger components (EL-20, PION-PRE, RANDOM) with a beam gate generated a pre-trigger (PRE-TRIG). Limitations in the speed at which the computer could log data on magnetic tapes made it necessary to limit the trigger rate to once per beam pulse. PRE-TRIG therefore went through a circuit which would allow the trigger (TRIG) to fire only once per beam pulse. The trigger provided the gates for the ADC's, generated start pulses for the TDC's, reset the latches, and interrupted the VAX computer to perform the event data logging. It also generated a gate signal for reading out the wire chambers.

2.5.3 Data Acquisition System

The main computer for the data acquisition system was a VAX 11-780 computer. This computer accumulated all the necessary hardware data and stored it on magnetic tape. Information that needed to be monitored on a periodic basis, such as the spectrometer magnets, high voltage power supplies, accumulated scaler and toroid values, and the target positions were controlled through CAMAC interfaces. The VAX could also correct any drifts in the spectrometer magnets or high voltage power supplies. However, because of the high pulse rate ($\leq$ 180 pps), other dedicated computers were necessary for accumulating pulse-by-pulse information.

Information from the beam steering system and the new toroid accumulators were read by an LSI-11 minicomputer. In addition, it corrected the beam steering, cleared the toroid electronics, and controlled the toroid calibration system. The VAX 11-780 computer would periodically ($\sim$ 5-10 min) receive the accumulated information from the LSI-11 and record it on magnetic tape.

Whenever the electronics was triggered, a computer interrupt to a PDP-11 was generated. This PDP-11 would read out all the ADC, TDC and latch information from the electronics along with the wire chambers hits and record it in a buffer. The PDP-11 was able to handle this information at a rate of 180 Hz, and the buffer was large enough to store many event blocks at the same time. The VAX 11-780 could then read out the information from this event buffer and store it on magnetic tape.

2.6 Run Plan

Extraction of the elastic form factors from the measured elastic cross sections required that data be taken at different scattering angles with Q^2 held fixed. Physical blocking of the spectrometer by the downstream beam pipe limited the minimum spectrometer angle to $\geq 11.5°$. Scattering angles $> 48°$ were ruled out because the spectrometer acceptance for events scattered from the ends of the target was reduced, resulting in unacceptably large systematic corrections. In addition, the exit snout attached to the scattering chamber only extended to $\approx 50°$. Final electron energies were limited by the spectrometer magnets to be $1 \leq E' \leq 8$ GeV/c. Changes in the incident beam energy E_0 would typically take 4-12 hours, while changes in the spectrometer momentum and angle could typically occur in 5-20 minutes. It was therefore desirable to minimize the number of changes in E_0. The incident and final energy and scattering angle were constrained by the kinematics of elastic scattering to have $x = Q^2/2M_p\nu = 1$.

From these constraints, a run plan was developed (Table 2.2). The small values of the cross sections for $Q^2 > 3$ (GeV/c)^2 made it impossible to gather enough statistics without expending what was considered to be an unacceptably large amount of beam time. A data point at $Q^2 = 1$ (GeV/c)^2 was included to provide a calibration point with previous experiments and as a check of the systematic uncertainties. Additional

elastic data with reduced statistics was taken at each incident energy used for the inelastic data as a calibration of the incident energy. This data was taken at Q^2 of 1, 2, 2.5, or 3 $(GeV/c)^2$ whenever possible and was included in this analysis.

Q^2 $(GeV/c)^2$	E_0 GeV	E' GeV	θ Deg	Peak I mA	e^-/pls	Time hrs
1.000	1.600	1.067	45.000	4.35	0.10	0.62
1.000	2.400	1.867	27.326	1.30	0.10	0.62
1.000	3.250	2.717	19.374	0.58	0.10	0.62
2.000	2.400	1.334	46.557	40.00	0.07	0.86
2.000	2.800	1.734	37.437	31.88	0.10	0.62
2.000	3.250	2.184	30.783	19.36	0.10	0.62
2.000	4.000	2.934	23.824	10.23	0.10	0.62
2.000	5.500	4.434	16.465	4.21	0.10	0.62
2.000	6.250	5.184	14.272	3.02	0.10	0.62
2.000	7.000	5.934	12.598	2.26	0.10	0.62
2.000	7.500	6.434	11.685	1.91	0.10	0.62
2.500	2.800	1.467	45.912	40.00	0.03	2.06
2.500	3.250	1.917	36.927	40.00	0.05	1.16
2.500	3.750	2.417	30.446	40.00	0.09	0.70
2.500	4.250	2.917	25.949	25.00	0.08	0.75
2.500	7.000	5.667	14.421	7.26	0.10	0.62
2.500	8.250	6.917	12.014	4.75	0.10	0.62
3.000	3.250	1.651	43.910	40.00	0.02	3.99
3.000	4.000	2.401	32.456	33.75	0.03	2.11
3.000	6.250	4.651	18.487	23.75	0.09	0.72
3.000	7.000	5.401	16.194	19.97	0.10	0.62
3.000	8.250	6.651	13.428	12.77	0.10	0.62

Table 2.2 – Elastic data run plan.

2.7 On-Line Data Taking Procedure

The beam current was adjusted during each run to limit the number of triggers per pulse to be no more than 0.1, limiting dead-time corrections to $< 10\%$. Frequently the rate was much less than this due to limitations in the maximum peak

current available. Gain amplifiers on the charge monitors were then set so the monitors were operating in the linear region and toroid calibration data would be taken. The spectrometer was rotated in a clockwise direction to the desired angle and the momentum was set so that the center of the spectrometer corresponded to $x = 1$. Hysteresis effects were avoided by always setting the spectrometer magnets from lower to higher momenta, and degaussing whenever it was necessary to go back down to a lower momentum. The beam was observed on the roller screens to confirm that it was steered properly onto the LH2 target, which was then inserted into the beam line, and data taking began. Typically 20,000 electron counts were logged at each of the main kinematic points; 2000-10,000 electrons were recorded during the additional energy calibration runs. An additional 200-500 counts were measured with the 20 cm DUM target in the beam to measure the background from scattering off the endcaps.

Chapter 3
Data Analysis-I

Transformation of the online data recorded on the magnetic tapes into the elastic form factors follows a series of distinct tasks. The first task was to make an event-by-event analysis to determine if the trigger was caused by a scattered electron passing through the detector. This was determined principally from the Čerenkov and shower counter information. Scattering kinematics ($\Delta P/P_0$, $\Delta\theta$, $\Delta\phi$) of the event were extracted from the wire chambers. This event data was then combined with other non-event information, such as the target density, integrated beam charge, detector efficiency, and dead-time, in order to determine the cross sections. Finally, the elastic form factors were extracted from the measured cross sections. Details of the event and non-event analysis are presented in this chapter. The cross section measurement and form factor extraction are presented in the following chapter.

3.1 Event Analysis

3.1.1 Tracking

Track Fitting

The pattern of wire hits in the wire chambers were recorded as a pattern of 1's and 0's, a 1 indicating a hit, a 0 indicating none. This data was then analyzed to determine the possible electron tracks that passed through the wire chambers. Due to the large number of wires and the three different orientations of the chambers, finding all possible tracks in the chambers was difficult. The task was simplified, however,

due to the low multiplicity of events in the chambers (~ 1), and the low probability of finding spurious tracks.

First, all possible tracks between hit wires in different pairs of P-chambers were calculated. Tracks that were clearly spurious, *i.e.* those that were far outside of the spectrometer acceptance, were ignored. The other P-chambers were checked for any wire hits within ± 4 wires of each of the tracks. This yielded the vertical coordinates of all possible tracks. Using this information, a similar process was followed with the T-chambers to find all possible tracks in the horizontal direction. In an initial pass of the data, searches were made for only those tracks that had associated hits in at least 7 of the 10 chambers, including 3 P-chambers and 3 T-chambers. This constraint limited the number of spurious tracks that could be found. If no tracks were found in this pass, a second search was made for tracks that had associated hits in at least 6 chambers, including 2 P-chambers and 2 T-chambers. This second search was included to reduce the inefficiency caused by the P-chamber support wires and was rarely needed. However, it was a much more CPU intensive search because of the greater number of spurious tracks that were found. If after these searches only one track was found, it was recorded as the particle track. Special cases of zero or multiple tracks are discussed below.

0-track events

Occasionally a clear electron trigger had occurred, *i.e.* a large pulse height existed in both the shower counter and the Čerenkov, but no track was found in the wire chambers. A measurement of the individual efficiencies of each chamber, including the effects of the support wires in the P-chambers, indicated that $< 0.1\%$ of electrons that pass through the chambers should fail to leave a clean track. Yet 1-2% of all clean electron triggers yielded no tracks. A detailed, event-by-event, analysis

of a few hundred of these events was done by hand, and the results indicated that the wires near the top of the P-chambers were fired in a large percentage of these events. Since the active area of the wire chambers (35 cm × 93 cm) was smaller than the active trigger area (53 cm × 90 cm for the Čerenkov, 40 cm × 102 cm for the TA), it was concluded that these events were caused by electrons that were in the active trigger area but scraped the top of the wire chambers and were outside the fiducial region (see below). Thus they were not "good" events to be included in the analysis. Monte-Carlo calculations of the spectrometer acceptance indicated that events such as these were expected to occur. These events were excluded from the analysis, and no efficiency correction was included for them.

Multi-track events

In the case that multiple tracks were found in the wire chambers, it was desirable to purge any tracks that were spurious or caused by pions and to try to find the "real" electron track associated with the trigger. Multiple tracks were found in approximately 10% of all events. Purging was done by forcing the multiple tracks to pass through a series of cuts until the "best" track was determined. Once the procedure had eliminated all but one track, the purging was stopped. If it was not possible to eliminate all but one track, one of the remaining tracks was chosen at random. In the case when two (or more) electrons did actually pass through the detectors within the same 20 ns period, it was also desirable to include only one of the tracks in the analysis since the correction for multiple events is already included in the correction for the electronics dead-time (see dead-time section). The hierarchy of multiple track purging was:

• Tracks whose value of $|X_{SP8}|$ was greater than $\approx$ 50 cm were eliminated since they did not point back to the spectrometer entrance.

• Tracks that did not intersect an area of the shower counter with a large shower pulse were presumed to be spurious or pions.

• Tracks whose values of $\Delta P/P_0$, $\Delta\theta$, or $\Delta\phi$ were outside the spectrometer acceptance were purged.

• Tracks that did not intersect a PR block with a large pulse height or an SF scintillator with a pulse corresponding to a minimum ionizing particle were presumed to be spurious or pions.

• Pairs of tracks that had horizontal and vertical positions within 6 mm and 16 mm, respectively, of each other were assumed to be caused by the same particle. The track with the greatest number of hit chambers, or the best χ^2 for the track fitting if the number of hit chambers was the same, was kept; the other track was purged. Only 1% of real double track events, which were themselves only a small percentage of the total number of events, were expected to be purged from this cut.

The number of events with multiple tracks after purging was usually $< 0.1\%$.

Track Reconstruction

Coordinates in the spectrometer hut were defined by: z-along the nominal particle trajectory, y-the direction of the vertical bend of the magnet, and x-perpendicular to the y-z plane in a right-handed coordinate system (Note: the target quantities X_{tgt}, Y_{tgt}, and Z_{tgt} were defined in a left-handed coordinate system). The particle track was parameterized in terms of its horizontal and vertical position along a plane z = constant (x and y) located between wire chambers 5 and 6, and its projected slope in the x-z and y-z planes (dx and dy). These parameters were then transformed into the particle characteristics at the target, which were the track location at the spectrometer entrance (X_{SP8} and Y_{SP8}, defined in a left-handed system like the target

coordinates), the track angles ($\Delta\theta$ and $\Delta\phi$), and the particle's fractional momentum ($\Delta P/P_0$). Only four quantities were measured by the wire chambers, so it was necessary to eliminate one of the target quantities from the analysis in order to get a one-to-one mapping between the spectrometer and target coordinates. It was therefore assumed that the particle track originated along the beam axis in the vertical direction (Y_{SP8}=0). The beam spot size was $\lesssim$ 3 mm in the vertical direction, so this was a good assumption. The target quantities reconstructed were thus $\Delta P/P_0$, $\Delta\theta$, $\Delta\phi$, and X_{SP8}. To first order, the quantities are related by:

$$\begin{aligned} \Delta P/P_0 &\propto y & \Delta\theta &\propto x \\ \Delta\phi &\propto dy & X_{SP8} &\propto x - dx \end{aligned} \tag{3.1}$$

The units of the positions and angles are cm and mr, respectively; the units of $\Delta P/P_0$ are in %. The full set of second order reverse transport coefficients, including modifications after a more careful analysis [22] of the 1967 dark current optics data [14,15] was performed, are given in Table 3.1.

3.1.2 Shower Counter

Electron events could be discriminated from pion events based on the amount of energy that was deposited in the shower counter. Raw signals from each phototube that were recorded by the ADC's were converted into a measurement of the shower energy of each event. The wire chamber information was used for each event to determine the path the particle followed through the shower array. The ADC pulse height signals from each phototube were proportional to the total energy deposited in each block; however, the proportionality constants were different because of the different gains of each phototube. It was necessary to determine these constants so the signal heights for each block along the particle's path could be linearly summed

	$\Delta P/P_0$	$\Delta\theta$	$\Delta\phi$	X_{SP8}
x	-0.00205	0.19387	-0.03694	4.55362
dx	0.00245	0.02408	0.03954	-4.29185
y	-0.34275	0.00050	-0.02689	-0.06007
dy	0.00074	-0.00419	-0.92820	-0.00142
$x \cdot x$	-0.00013	0.00051	0.01063	0.01756
$x \cdot dx$	0.00012	-0.00103	-0.01993	-0.03237
$x \cdot y$	0.00059	0.01485	0.00034	-0.00492
$x \cdot dy$	0.00005	-0.00098	0.00056	0.00133
$dx \cdot dx$	0.00000	0.00051	0.00930	0.01543
$dx \cdot y$	-0.00059	-0.01421	-0.00037	0.00850
$dx \cdot dy$	-0.00003	0.00082	-0.00052	-0.00106
$y \cdot y$	0.00020	-0.00012	-0.00525	-0.00411
$y \cdot dy$	0.00136	0.00003	-0.00083	-0.00019
$dy \cdot dy$	0.00004	0.00001	-0.00009	-0.00005
1	0.00044	0.00169	0.00171	0.16211

Table 3.1 – Second order reverse transport coefficients for the 8-GeV spectrometer which give the target coordinates of an event in terms of the particle's track coordinates in the wire chambers. Units are in %, mr, or cm, where appropriate.

as a measurement of the total energy deposited. Corrections were also made for the effects of light attenuation within the blocks.

The ADC pulse height signals from each phototube along the particle's path, plus the phototubes from the nearest adjacent blocks, were included in the sum to determine the energy deposited by each event. Adjacent blocks were included in order to capture any leakage due to the transverse spread of the shower in the Pb-glass array. Enough rows of blocks were included to contain at least 98% of the longitudinal penetration of the shower in the lead glass [20]. The calibration coefficients for each phototube were determined using an iterative method of minimizing the shower

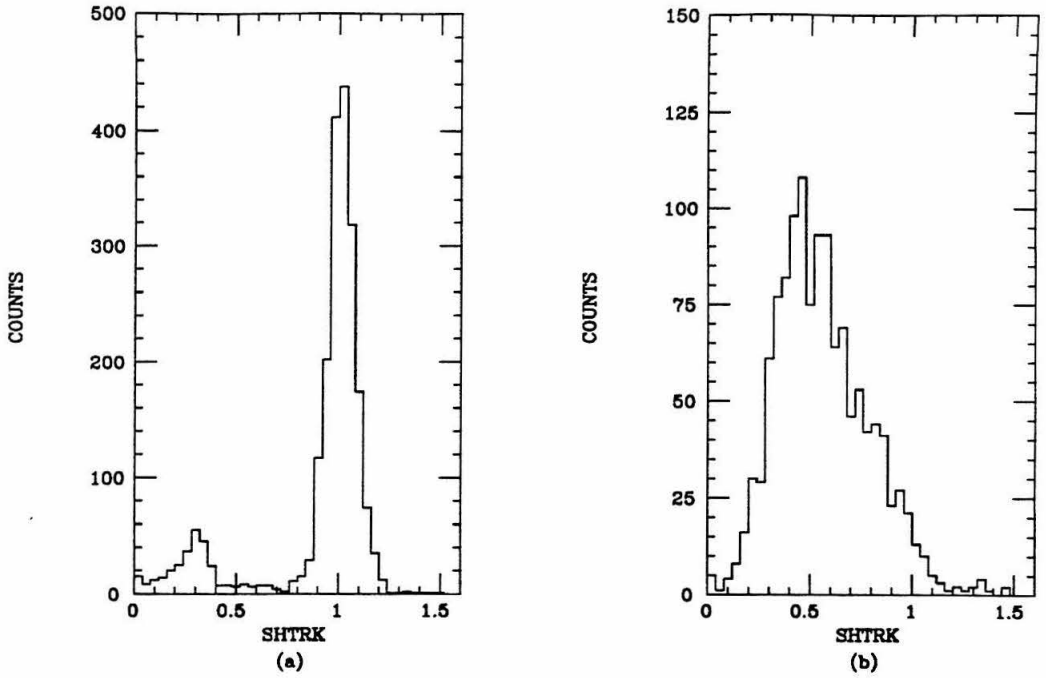

Figure 3.1 – (a) A high pion background (inelastic data) spectrum in the shower counter requiring a Čerenkov pulse above an ADC channel of 50. (b) The same spectrum requiring a Čerenkov pulse below an ADC channel of 50.

spectrum width while requiring that the spectrum peak be located at a value of 1.0 (when normalized by E'). Corrections were made for the effects of light attenuation in the vertical direction within the lead glass blocks. The attenuation was assumed to be linear in the distance between the track and the face of the phototube. The attenuation coefficients were determined by measuring the shift in each of the ADC spectrum peaks as a function of the distance of the tracks from each phototube and determining a first-order linear correction. The ADC pulse heights were scaled by the particle's momentum E' so the location of the shower spectrum peak was independent of E', in addition to the correction for the 50% attenuators that were inserted

in the signal cables for data taken at values of $E' > 4$ GeV. The normalized energy (SHTRK) was thus:

$$\text{SHTRK} = \sum_{i=1}^{N_{row}} \sum_{j=j_{blk}^{i}}^{j_{blk}^{i}\pm 1} C_{ij}[1 - a_{ij}(y_i^{trk} - y_{ij}^{tube})] \times \frac{ADC_{ij}}{E'} \tag{3.2}$$

where N_{row} is the number of rows of shower counter phototubes included, j_{blk}^{i} is the block in each row the track intersects (with the + or − of ± chosen depending on which adjacent block is closest to the particle track), C_{ij} is the phototube calibration constant, a_{ij} is the light attenuation coefficient, y_i^{trk} is the y position of the track in row i, y_{ij}^{tube} is the vertical position of each phototube, and ADC_{ij} are the measured ADC values of each block. N_{row} was 4 (PR, TAD, TAU, and TB) for $E' < 5$ GeV, and was 5 (PR, TAD, TAU, TB and TC) for higher momenta.

A SHTRK spectrum, taken with deep inelastic data at $E' = 1.08$ GeV and a background rate of $\pi/e \approx 30$, is shown in Figure 3.1(a). This spectrum only includes those events that fired the Čerenkov counter. The large electron peak at SHTRK≈ 1 is clearly seen, with the low energy pion tail. Figure 3.1(b) is the same spectrum, but only includes those events that did not fire the Čerenkov. This shows the response of the shower counter to pion events. Figure 3.2 shows a typical spectrum cut on the Čerenkov under elastic running conditions ($E' = 1.734$ GeV) where the pion backgrounds are small. The line is a gaussian fit to the electron spectrum. The resolution of the shower counter was found to be $\approx 18\%/\sqrt{E'}$. This E' dependence is expected from the statistics of the electromagnetic shower (# of photo-electrons $\propto$ # of particles in shower $\propto E'$).

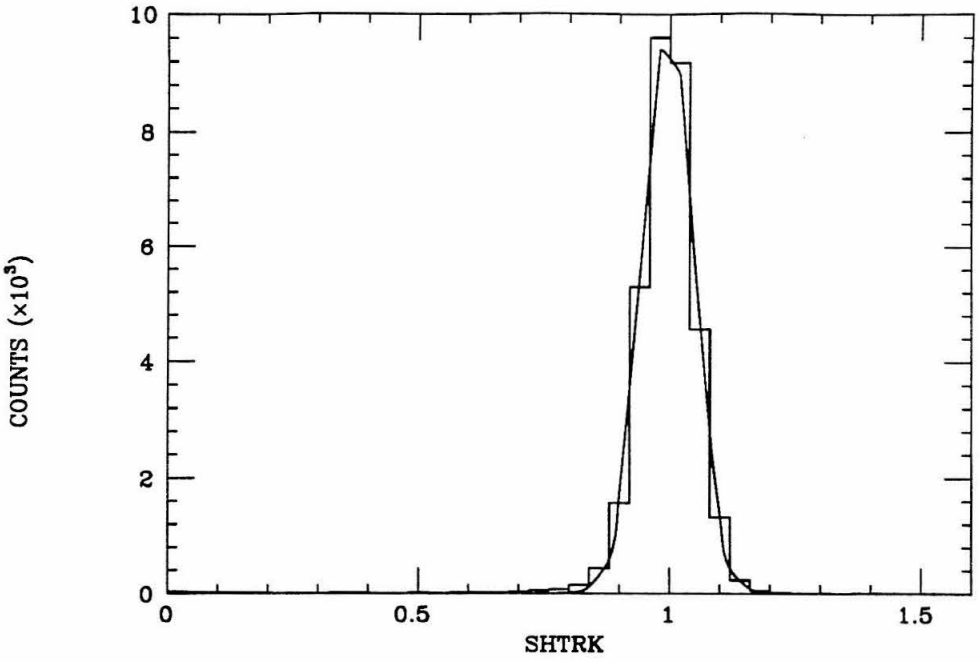

Figure 3.2 – An elastic data spectrum in the shower counter, cut on a large Čerenkov pulse height. The solid line is a gaussian fit.

3.1.3 Čerenkov

In Figure 3.3 a typical Cerenkov spectrum under the elastic scattering conditions is shown. The curve is a Poisson fit to the electron peak and indicates that 7.72 ± 0.12 photoelectrons were typically produced in the phototube. This was consistent with the estimate of 7-9, which was predicted from the number of photons emitted by an electron [18] passing through 3.30 m of hydrogen gas ($\sim$ 46) and assuming a photo-conversion efficiency of 15-20%.

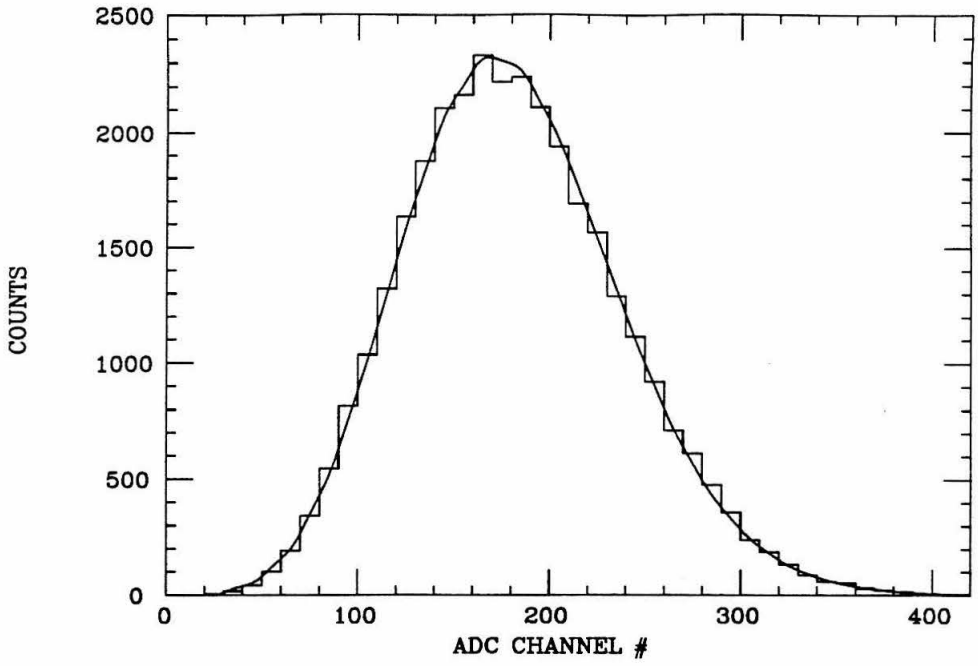

Figure 3.3 – The Čerenkov pulse height spectrum for an elastic data sample. The curve is a Poisson fit to the spectrum indicating ≈ 8 photoelectrons.

3.1.4 Electron Identification and Event Histogramming

The definition of an electron event incorporated all of the above components and is stated here for completeness:

• Electron Trigger. Only events that fired the EL-20 component of the trigger were included.

• One-Track. It was required that one particle track be found in the wire chambers.

• Good Fiducial. A fiducial region was defined within the detector area and only those particles that passed through this region were included in the analysis. This

cut was included in the definition of the acceptance function; it was therefore not necessary to include it in the efficiency correction. The fiducial region was defined by an area on the face of the PR from -43.67 to 43.7 cm in x and -11.07 to 13.07 cm in y, relative to the nominal axis in the hut. This corresponded to a 3.5 cm inset from the edges of the shower array.

• High Čerenkov. The Čerenkov pulse height was required to register above an ADC channel of 50.

• High Shower Energy. The energy deposited in the shower counter was required to have SHTRK> 0.70.

Electron events were then accumulated in a 3-dimensional histogram with coordinates ($\Delta P/P_0$,$\Delta\theta$,$\Delta\phi$). The $\Delta P/P_0$ dimension had 40 bins, ranging from -4% to 4%, with bin widths of 0.25%. The $\Delta\theta$ dimension had 24 bins, ranging from -8 mr to 8 mr. The central 8 bins were 1 mr in width; the edge bins were 0.5 mr in width. The $\Delta\phi$ dimension consisted of 14 bins, ranging from -40 mr to 40 mr. The central 4 bins were 10 mr in width; the edge bins were 4 mr in width. Edge bins were made smaller than the central bins to reduce errors caused by the acceptance function correction, which changed rapidly at the edges.

3.2 Non-event Analysis

3.2.1 Acceptance

Physical apertures within the spectrometer blocked the passage of electrons that were not within the spectrometer acceptance. In a simple model, electrons that are emitted at a specific value of ($\Delta P/P_0$, $\Delta\theta$, $\Delta\phi$, X_{tgt}, Y_{tgt}) will have either a 100% probability of reaching the detector hut or a 100% probability of being blocked by the

spectrometer apertures and magnets. In this case the acceptance function is a five-dimensional function that takes on a value of 1 in the area with perfect acceptance, and 0 in the area of perfect rejection. In practice, however, multiple scattering, the finite resolution of the wire chambers, and the assumption that Y_{tgt}=0 smears out the edges of the acceptance function. In order to include a large amount of statistics in the data analysis it was necessary to correct the edges of the acceptance for the efficiency of electrons within these regions to reach the detector area. It was also necessary to correct the absolute value of the acceptance for any dependence on E', θ, or the target length (*i.e.* Z_{tgt}).

Determination of Acceptance Function

Corrections for the spectrometer acceptance were made with a histogram binned in $\Delta P/P_0$, $\Delta\theta$, and $\Delta\phi$, just as the event kinematics were stored. Each bin in the acceptance function, ACC3($\Delta P/P_0$,$\Delta\theta$,$\Delta\phi$), contained the efficiency for detecting electrons with measured target characteristics $\Delta P/P_0$, $\Delta\theta$, and $\Delta\phi$.

The acceptance function was generated from the deep inelastic data that was taken in parallel with this experiment and analyzed by S. Dasu [11]. Data from an Fe target (effectively a zero length target) at a variety of kinematics were measured and binned in histograms of $\Delta P/P_0$, $\Delta\theta$, and $\Delta\phi$. A model of the distribution of events across the acceptance was generated for each run from the kinematic dependence of the cross section based on a modified fit to deep inelastic deuterium data [23], and included corrections for the Fermi motion of the nucleons, the non-zero value of $R = \sigma_L/\sigma_T$ [6] the EMC effect [7] radiative corrections [11], and charge symmetric backgrounds [24]. A histogram of the "expected" number of counts in each bin (HIST3$_{exp}$) was generated from this model and was normalized to the measured histogram (HIST3$_{meas}$) in the central region of the acceptance where the efficiency was

expected to be effectively equal to 1. Both of these histograms were then summed over all runs. Runs in which the cross section had a strong kinematic dependence across the acceptance or large background contributions were excluded. A total of $\sim 10^6$ deep inelastic scattering events were measured and included in this analysis. By comparing the two summed histograms, $\mathrm{HIST3}_{exp}$ and $\mathrm{HIST3}_{meas}$, the efficiency of each bin could be determined. The acceptance function was thus defined as:

$$\mathrm{ACC3}(\Delta P/P_0,\Delta\theta,\Delta\phi) \equiv \frac{\mathrm{HIST3}_{meas}(\Delta P/P_0,\Delta\theta,\Delta\phi)}{\mathrm{HIST3}_{exp}(\Delta P/P_0,\Delta\theta,\Delta\phi)} \tag{3.3}$$

The value of the acceptance function versus $\Delta P/P_0$, $\Delta\theta$, and $\Delta\phi$ (summed over the other two variables in each case) is shown in Figure 3.4.

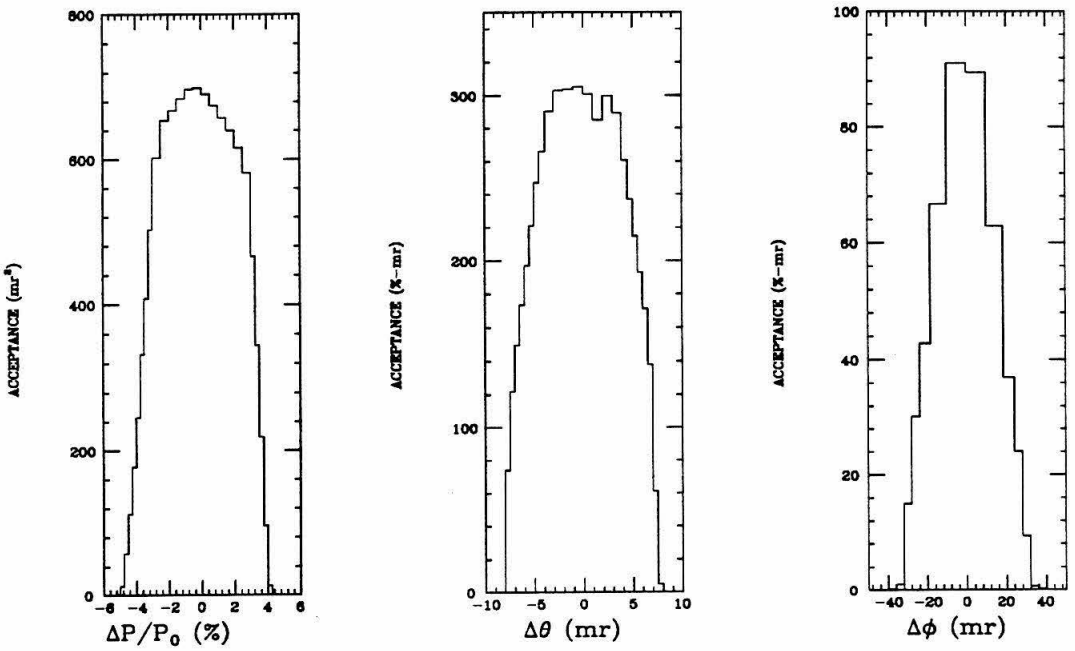

Figure 3.4 – The acceptance function measured with deep inelastic data vs. $\Delta P/P_0$, $\Delta\theta$, and $\Delta\phi$. Each histogram is summed over the entire range of the other two variables.

From the acceptance function it was determined what region of the acceptance would be included in the analysis. Events from the far edges of the acceptance were excluded because of the large efficiency corrections that were necessary. Data was included only from the region $-3 < \Delta P/P_0 < 3\%$, $-6 < \Delta\theta < 5$ mr, and $-24 < \Delta\phi < 24$ mr. The one-dimensional projection of the acceptance function versus each of these three variables, with these cuts applied, is shown in Figure 3.5. It should be noted that most of the elastic scattering events occur at the elastic peak ($\Delta P/P_0 \approx 0$), with the elastic tail extending below ($\Delta P/P_0 < 0$).

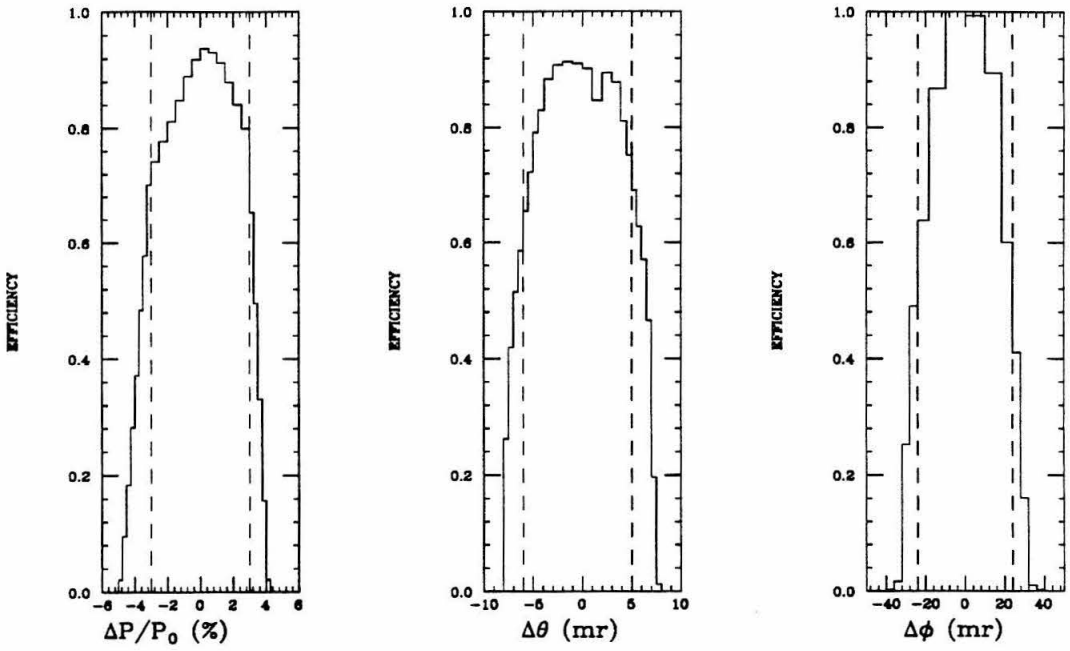

Figure 3.5 – The acceptance function with the cuts used in this analysis: $-3 < \Delta P/P_0 < 3\%$, $-6 < \Delta\theta < 5$ mr, $-24 < \Delta\phi < 24$ mr. The dashed lines show the values of the cuts used for each of the variables.

The acceptance function extracted from the deep inelastic data included data taken from a range of spectrometer momentum ($1 < E' < 8$ GeV/c) and scattering angles ($11.5° < \theta < 48°$). It was also taken exclusively from a near 0-length target. Systematic effects caused by the extended LH2 target or the changes in the spectrometer momentum and angle settings must also be included.

Corrections to Solid Angle

A Monte-Carlo simulation program of the 8-GeV spectrometer transport properties was written by D. H. Potterveld [25] and was modified for this analysis. In this simulation a uniform distribution of events in $\Delta P/P_0$, $\Delta\theta$, and $\Delta\phi$ was produced at the target pivot position. Events were generated over a large enough area to completely cover the spectrometer acceptance. They were also generated uniformly along the target length, and were assumed to be distributed in a two-dimensional gaussian in the lateral beam direction, with $\sigma_x = \sigma_y = 1$ mm. These events were then transported through the spectrometer using forward transport coefficients generated with the SLAC program TRANSPORT [26]. The forward transport coefficients [9] from the target to the spectrometer hut are given in Table 3.2. Each event was checked to see if it collided with any of the apertures within the spectrometer. If it did intersect one of the apertures, it was presumed to be lost. If the event reached the spectrometer hut, it was linearly transported through the detectors, including multiple scattering effects of the Čerenkov detector (windows, gas and mirror). The track trajectory within the wire chambers was then recorded. A random number generator was used to simulate the expected wire chamber resolution (based on the wire spacing) of $\sigma_x = 2.3$ mm, $\sigma_y = 1$ mm, $\sigma_{dx} = 2.8$ mr, and $\sigma_{dy} = 1.25$ mr. The measured trajectory characteristics were then transformed to the target characteristics using the reverse transport coefficients that were used in the event analysis. These events

were recorded in a three-dimensional histogram in $\Delta P/P_0$, $\Delta\theta$, and $\Delta\phi$. This histogram was normalized to the total number of events initially generated at the target in each bin.

	x	dx	y	dy
$\Delta P/P_0$	0.000	0.000	-2.907	0.203
$\Delta\theta$	4.575	4.893	0.000	0.000
$\Delta\phi$	0.000	0.000	-0.014	-1.090
X_{SP8}	0.028	-0.189	0.000	0.000
Y_{SP8}	0.000	0.000	-0.928	0.000

Table 3.2 – Forward transport coefficients generated with the program TRANSPORT. These coefficients transform the target quantities to the position and angle of the track at the focal planes (to first order).

An acceptance function for a zero-length target at $E' = 3$ GeV was generated with the Monte-Carlo. These conditions roughly corresponded to the conditions under which the acceptance function was extracted from the data. This served as the normalization function for measuring systematic effects. All of the following acceptance functions are shown relative to this normalization function with the acceptance cuts, as discussed previously, applied.

Surveys of the 8-GeV spectrometer indicated that the magnets and spectrometer did not move or rotate significantly when the spectrometer was rotated in θ, so no θ dependence of the acceptance was anticipated for a zero-length target. However, such an effect might occur for an extended target. The Monte-Carlo simulation was used to generate the acceptance function for a 20 cm target with the spectrometer set

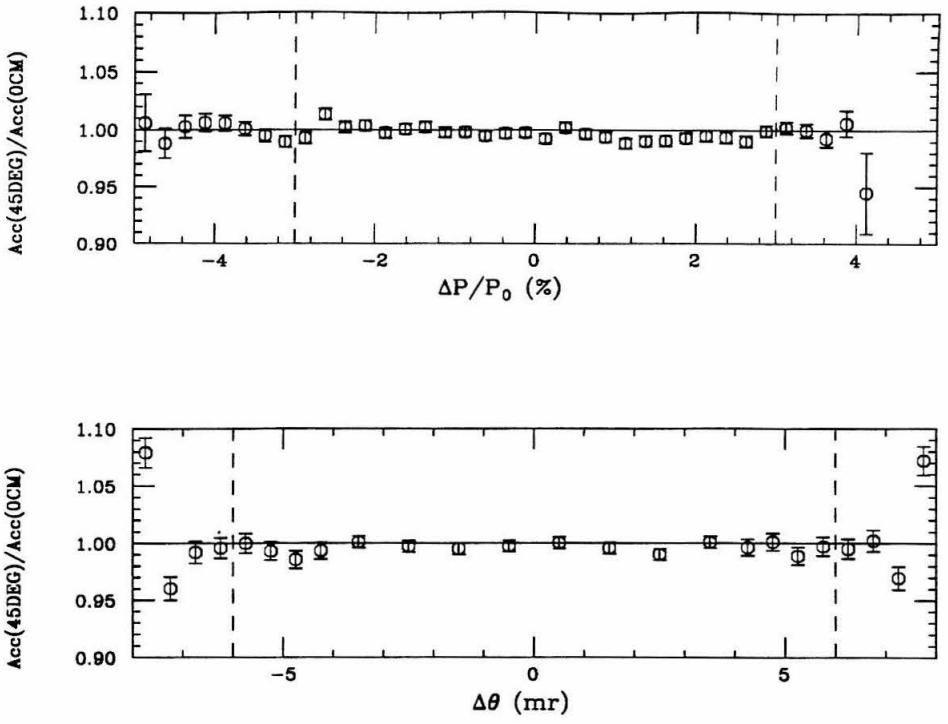

Figure 3.6 – The Monte-Carlo acceptance function for a 20 cm target with a spectrometer angle of 45° relative to the nominal acceptance shown versus $\Delta P/P_0$ and $\Delta\theta$.

at 45°. Events that are initiated from the target ends have a reduced efficiency for reaching the target hut. This effect can be seen in Figure 3.6 versus $\Delta P/P_0$ and $\Delta\theta$. A slight reduction in efficiency was measured, but was independent of $\Delta P/P_0$ and $\Delta\theta$ within the acceptance cuts used. Deviations at the extreme values of $\Delta\theta$ can be seen, however. At this setting of the spectrometer angle the reduction in the overall acceptance was 0.32%.

A similar analysis was done with other settings of the spectrometer angle. The reduction due to the effective target length (measured along X_{tgt}, as seen from the spectrometer) was largest at the largest scattering angle. This is shown for different values of the spectrometer angle in Figure 3.7. A linear fit of this data was made

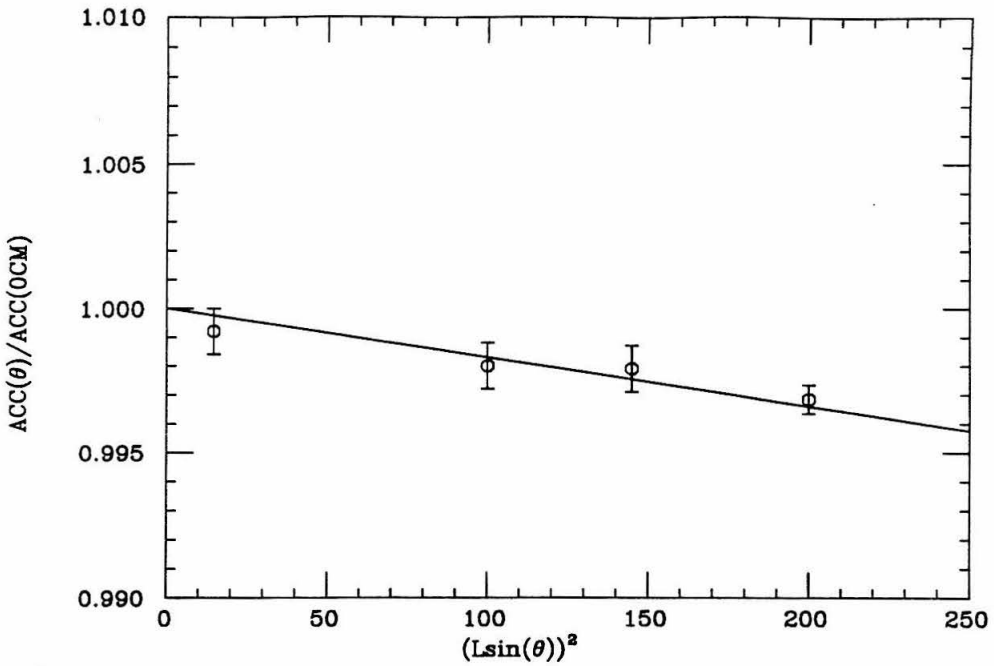

Figure 3.7 – The reduction of the spectrometer acceptance due to target length effects, as determined from the Monte-Carlo, shown versus the θ dependent variable $[L\sin(\theta)]^2$, with L = 19.972 cm. The solid line is the linear fit described in the text, with a value of $x = 1.7 \times 10^{-5}$ cm^{-2}.

using the functional form Acc$\propto (1 - x[L\sin(\theta)]^2)$, where $L = 19.972$ cm and x was a free parameter. Other functional forms for the θ dependence were tried, but this form yielded the best description of the data, and was the most reasonable form. The fit yielded a value of $x = (1.7 \pm 0.2) \times 10^{-5}$ cm^{-2}, with χ^2/dof= 0.3. An analysis of deep inelastic data taken in parallel with this experiment with a 20 cm deuterium cell (nearly identical to the LH2 target) measured [27] a value of $x = (3.4 \pm 7.5) \times 10^{-5}$ cm^{-2}, which is consistent with the Monte-Carlo value.

Although the target length effect was found to be nearly independent of the $\Delta P/P_0$ and $\Delta\theta$ cuts applied, it had a strong dependence on the $\Delta\phi$ cut. This is shown

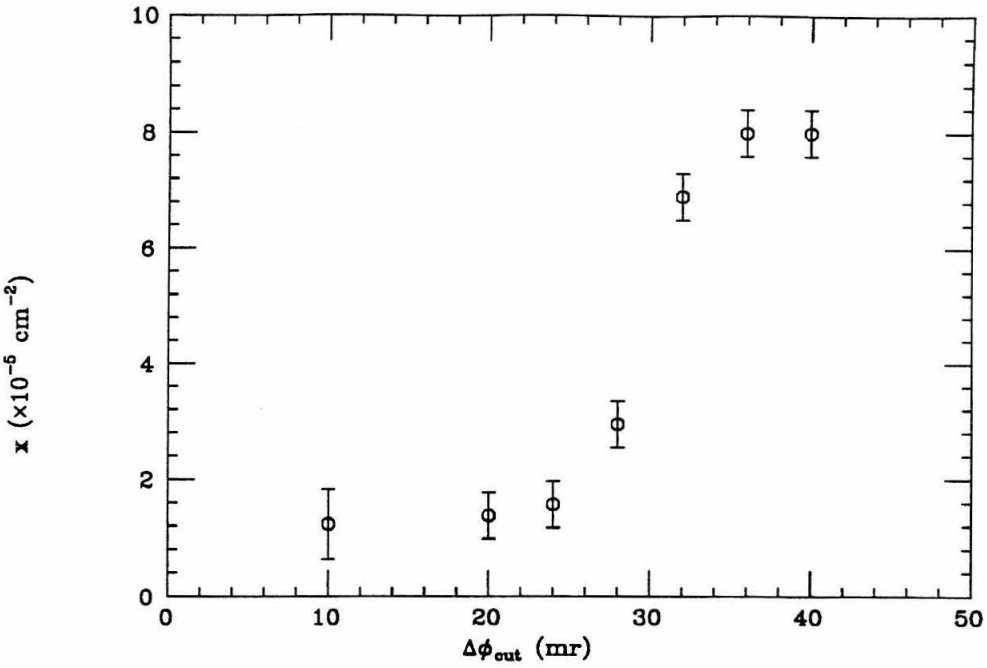

Figure 3.8 – The acceptance parameter x (defined in the text) as a function of the $\Delta\phi_{cut}$, measured by the Monte-Carlo.

in Figure 3.8 where the parameter x, as defined above, is plotted versus the absolute value of the $\Delta\phi$ cut applied ($-\Delta\phi_{cut} \leq \Delta\phi \leq \Delta\phi_{cut}$). A sharp decrease between 24 mr and 36 mr can be seen. This was a motivating factor in the determination of the $\Delta\phi$ cuts of $\pm$24 mr.

The acceptance could depend on the value of E' through two different effects. Multiple scattering at low E' could have potentially altered the acceptance function. The Monte-Carlo was used to simulate the acceptance function at $E' = 1$ GeV/c and $E' = 8$ GeV/c, and no significant changes were discovered. The transport coefficients could also have changed with E' as the field strengths in the spectrometer magnets changed, causing saturation or changes in the fringe fields. This was measured with

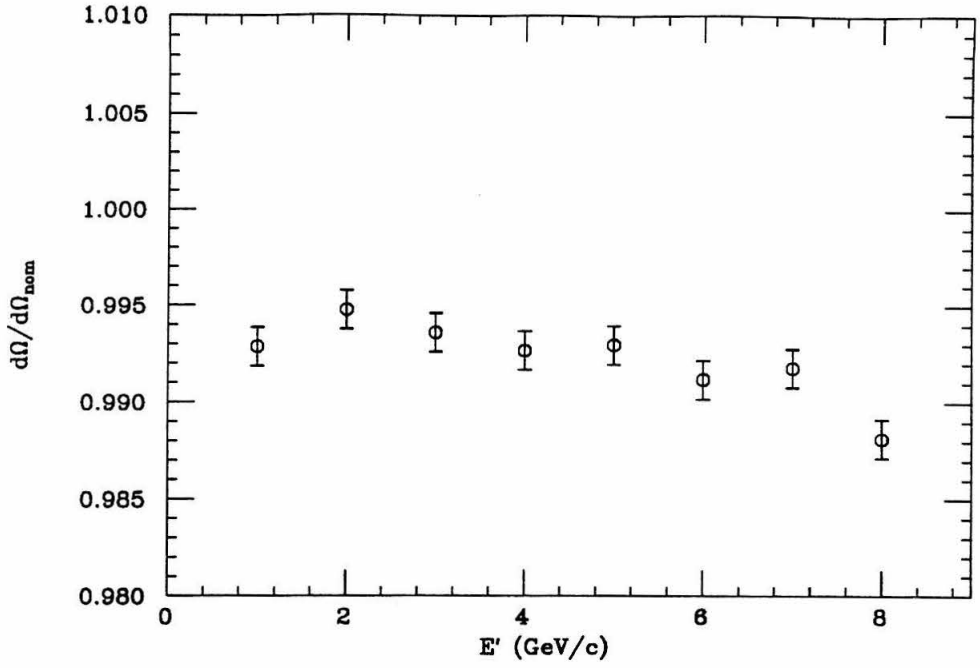

Figure 3.9 – The solid angle, $d\Omega$, vs. E' from the wire order data relative to the value assumed in the event-by-event analysis.

the wire orbit technique [16,17]. The value of the solid angle $d\Omega$, defined as proportional to the product of the transport coefficients $\langle \Delta\theta_{tgt} \mid x_{wc} \rangle \langle \Delta\phi_{tgt} \mid dy_{wc} \rangle$, is shown in Figure 3.9 as a function of E' relative to the value of the transport coefficients used in the event analysis. It was found that the absolute normalization of the solid angle changed by $\sim 0.7\%$, and varied with E' by $\sim 0.5\%$.

3.2.2 Efficiency and Dead-Time

The efficiency for detecting electrons in each of the detector elements must be measured. Corrections were also necessary for the time the electronics and computer were "dead" and not capable of recording electron events. These corrections are discussed here.

Efficiency

A Poisson fit to the Čerenkov spectrum of electrons (see Čerenkov section) indicated the number of photoelectrons was ~ 8 with a peak position at ADC channel 160. Below the ADC cut of channel 50, the area of the Poisson curve was 0.25%, indicating an efficiency of 99.75%. The Čerenkov efficiency was monitored on a run-by-run basis by analyzing events that deposited a large amount of energy in the shower counter and did not require the Čerenkov to fire the trigger. These runs indicated an efficiency of $\approx 99.7\%$. An analysis of pion events (low SHTRK) in a deep inelastic run indicated the pion rejection for this cut was $\sim 10^4 : 1$.

The wire chamber efficiency was determined by measuring the efficiency of each individual chamber and then computing a total efficiency factor. Individual chamber efficiencies were calculated versus x_{hut} to include the localized effects of the P-chamber support wires. On an event-by-event basis, it was determined if a given chamber was necessary for finding the track. If the chamber hit was necessary, the event was not included in the efficiency calculation. For those events that did not require that chamber, the percentage of events that had an associated chamber hit (± 4 wires from the track intersection) was calculated. These efficiencies were stored in a histogram binned in x_{hut} with a bin width of 1 cm. Individual efficiencies for a P-chamber and T-chamber are shown in Figure 3.10. The average efficiency of each chamber was $\sim$ 90-95%. The total wire chamber efficiency computed was 99.9% (Figure 3.10(c)), including the effect of the P-chamber support wires of $\sim 0.06\%$.

The efficiency of the wire chambers was also measured on a run-by-run basis for electrons that pass near the center of the detectors (*i.e.* those events that had large pulse heights in the Čerenkov and the middle counters of SF, SM, PR, and TA). This eliminated events near the edges of the detectors. The ratio of 0-track/1-track events

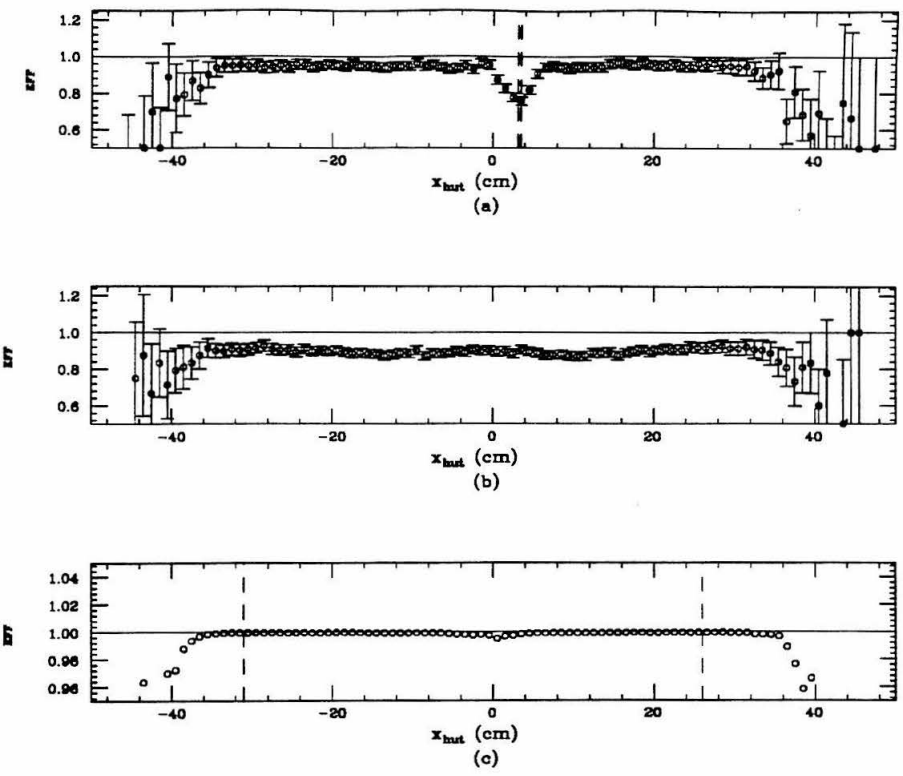

Figure 3.10 – The measured efficiencies of (a) a P-chamber, (b) a T-chamber, and (c) the entire wire chamber tracking system, shown vs. x_{hut}.

under these conditions was a measure of the wire chamber efficiency and indicated an efficiency of 99.9%, in agreement with the previous analysis.

The SHTRK spectrum, shown in the event section, was cut at a normalized value of 0.7 with the electron peak at a value of 1.0. Assuming a gaussian distribution of events with a FWHM resolution of $18\%/\sqrt{E'}$ (as measured), the efficiency was $\geq 99.94\%$ for $E' \geq 1$ GeV. A run-by-run estimate of the SHTRK efficiency was also performed by cutting events on 1-track, Čerenkov, and a requirement that the track be in the center of the detector area ($|\Delta P/P_0| < 3.5\%$, $|\Delta\theta| < 6$ mr, and $|\Delta\phi| < 28$ mr). It was assumed that all of the counts with $0.5 <$ SHTRK < 0.7 were electrons

that failed the SHTRK cut. This gave a lower bound on the efficiency of 99.8%, in agreement with the gaussian analysis.

The trigger efficiency was calculated from the efficiencies of each of the individual components, and was $\approx$ 99.9988%. Thus any inefficiency due to the trigger was negligible.

Dead-Time

Dead-time due to the electronics was determined by comparing the scaler rates of a coincidence of PR, TAD, and Č (PTC) with 20, 40, 60 and 80 ns gate widths. Scalers EL-20, 40, 60 and 80 were not used due to problems in the electronics that caused EL-20 and EL-40 to double pulse. A linear extrapolation of these scaler rates to 0 ns yielded the ideal scaler rate with no dead-time, as shown in Figure 3.11. The electronics dead-time ranged from between 0.00 to 0.75%, and was consistent with expectations based on the measured electron rate and a 20 ns pulse width.

The fact that the computer was limited to recording only one event per pulse also created a dead-time effect. After each computer trigger occurred, a veto pulse was created which lasted for the rest of the beam pulse. The rates of PTC-20 and PTC-40 were counted along with the rates of PTC-20 and PTC-40 in coincidence with no veto pulse (PTC-20V and PTC-40V). The ratio of the rates PTC-20/PTC-20V and PTC-40/PTC-40V measured the computer dead-time. These two measurements always agreed to 0.2% and were consistent with the measured electron rate per beam pulse. They were averaged to compute the total computer dead-time.

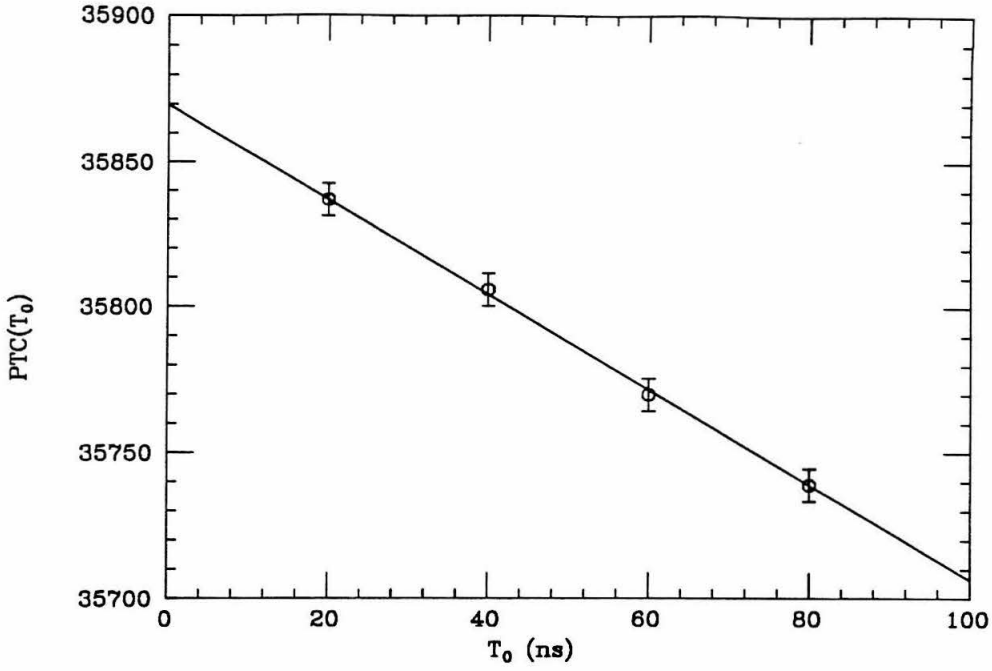

Figure 3.11 – A typical plot of PTC with 20, 40, 60 and 80 ns dead-times shown vs. the dead-time.

3.2.3 Target Density

As the beam passed through the hydrogen in the LH2 target it deposited energy, resulting in heating that reduced the target density. The average density was determined by measuring the temperature and pressure of the circulating hydrogen as it entered and exited the target. This measurement is shown without any beam heating effects (measured while the dummy target was in the beamline) in Figure 3.12(a). At one point during the experiment, the pressure of the recirculating hydrogen was increased, which increased the density by 1.2%. The average density measured while the LH2 target was in the beam is shown in Figure 3.12(b). The shift of the density

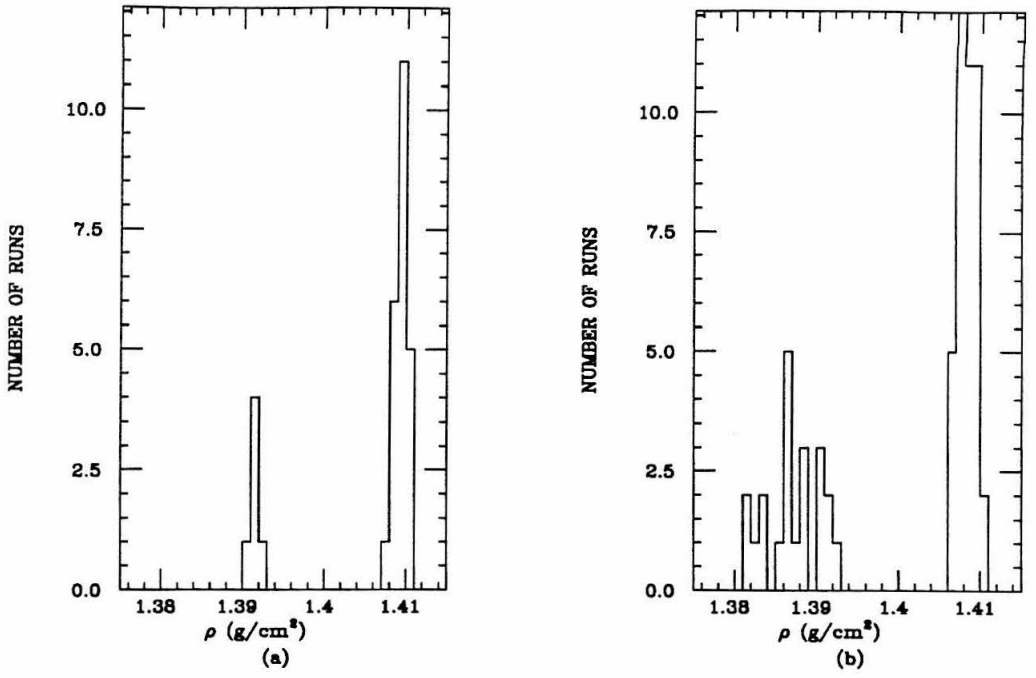

Figure 3.12 – The average hydrogen density. The hydrogen flow pressure was altered during the experiment, shifting the average density from the lower peak to the higher peak. (a) The measured hydrogen density when data was taken with the dummy target. (b) The measure hydrogen density when the LH2 target was in the beamline.

to lower values is shown, although the average density was never altered by more than 0.7%.

The beam could also cause local density fluctuations by depositing enough energy along the beam axis to cause the liquid hydrogen to boil, creating small bubbles. As these bubbles expand during the 1.6 μs pulse, the hydrogen density for electrons that arrive later in the beam pulse is lowered. Such local effects were not well measured by the average hydrogen density. Comparisons of the measured hydrogen cross sections at different beam currents and repetition rates, however, were sensitive to these effects. There was only one kinematic setting at which cross sections were measured with

significantly different (and large) beam currents. This data sample was limited due to the difficulty encountered in achieving high beam currents during most of the experiment. No significant limit on local beam heating effects could be determined from this data.

A much better, and more realistic, limit could be determined by including the entire hydrogen elastic data set in the analysis of beam heating effects. Due to the low beam currents that were used during most of the experimental run, the average peak current, $\langle I \rangle$, and ε were not well correlated. Local beam heating effects could be determined by dividing the measured cross sections by a model of the kinematic dependence and performing a linear fit to the peak current of the form $a - b\langle I \rangle$, where a was a normalization parameter and b indicated any beam heating effects. By using a variety of models the sensitivity of the beam heating parameter b to the choice of the elastic form factors used could be determined. Conversely, this method also demonstrated the sensitivity of the extracted form factors to local beam heating effects.

Three different models for the form factors were used in this method. The first used the values of the form factors extracted from this experiment, assuming no beam heating effects, which indicated that $G_E^p/G_D > 1$. Values of $a = 1.000 \pm 0.003$ and $b = (0.7 \pm 2.2) \times 10^{-4}$ $(\mathrm{mA})^{-1}$ were extracted, with $\chi^2/\mathrm{dof}=0.9$. By fixing $a = 1$ a value of $b = (0.5 \pm 1.4) \times 10^{-4}$ $(\mathrm{mA})^{-1}$ was extracted with $\chi^2/\mathrm{dof}=0.9$. Models using the fit to the form factors of Höhler [28] ($G_E^p/G_D < 1$) and the dipole approximation ($G_E^p/G_D = 1$) were also used (see Theory section). With these fits the value of the normalization parameter a differed from 1 by up to a few percent, as expected. But the measured values of the boiling parameter were $b = (0.6 \pm 2.2) \times 10^{-4}$ $(\mathrm{mA})^{-1}$ (for Höhler) and $b = (0.7 \pm 2.2) \times 10^{-4}$ $(\mathrm{mA})^{-1}$ (for the dipole); the χ^2/dof were 1.3

and 1.1, respectively. The small value of b and the increased value of χ^2/dof for the different fits indicated that $\langle I \rangle$ and ε were not well correlated, and the limits on the boiling effect were not sensitive to the values of the form factors used in this method. The maximum boiling effect was limited to 0.7% at 37 mA, with a maximum effect of 0.3% at a normal operating current of 15 mA. Similar results were obtained for an analysis of the beam heating effects correlated with the average current rather than the peak current.

3.2.4 Incident Charge

The total charge incident on the target during each run was measured using the two independent toroidal charge monitors. Six different readouts of the toroids (three for each monitor) were accumulated on a pulse-by-pulse basis and periodically stored on magnetic tape. This gave a rough measurement of the total number of peta-electrons (PE$\equiv 10^{15}\ e^-$) that were incident on the target. Corrections for drifts in the gains and the calibrators were necessary to achieve a more accurate measurement. Analysis of the toroid calibration runs was necessary to determine these corrections.

Data from the toroid calibration runs were periodically accumulated. These runs measured time-dependent drifts in the gain of the toroids, as well as the gain relative to a nominal setting ($\equiv$ 1). They also measured the non-linearity of the toroid readout circuit with respect to the pulse charge passing through the toroids, and provided redundancy for self-calibration of the calibrator elements themselves (the DAC and attenuator). Cross calibrations were periodically performed by switching the calibrators between their two respective toroids.

A systematic study of the calibrations was performed in the offline analysis. Errors in the software for the two newer readout systems made this data unreliable; it was therefore decided to only use the older readouts in the data analysis. These

readouts have a long history of reliability. The analysis indicated that the toroid gain amplifiers were generally stable over time at the 1% level. However, a few occasional, sudden shifts in the gains of the toroids did occur. The largest such shift, $\sim$ 15%, occurred near the middle of the experiment when the beam was momentarily badly mis-steered. It was discovered that an electronic chip in both readout systems had burned out. This chip allowed for the polarity of the signal pulse to be switched and was redundant with other elements of the system. It was decided to simply replace this chip with a set of copper wires, causing an increase in the gain of the toroids. Intensive calibration data were taken at this period of time, and the shift in the gain was well measured.

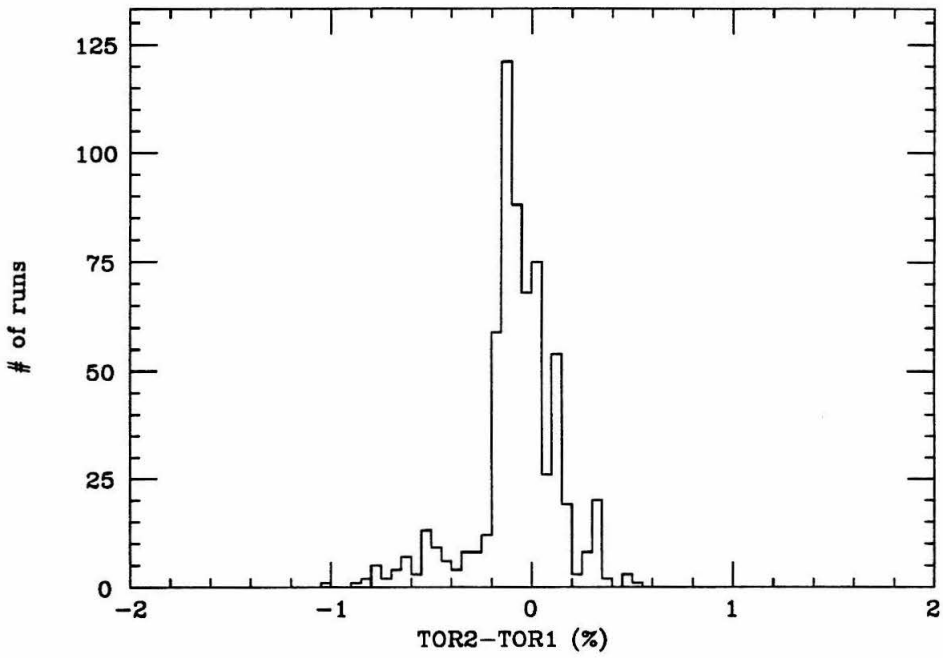

Figure 3.13 – Comparison of the two independent toroid readouts (TOR2 and TOR1). The average of the two readouts was used in the analysis. The readouts agreed to $-0.08 \pm 0.21\%$ on average.

Corrections for time dependent drifts were made by linearly interpolating the calibration corrections taken immediately before and after each run. The time between these calibration runs was ~ 8 hours, and the gains were typically stable over such time periods to $\sim 0.2\%$. Non-linearities in the gain amplifiers were determined by periodically measuring the gains with many different calibration charges, and then interpolating for the average beam pulse charge used during the run. This correction was $\sim 0.1\%$. The calibration attenuators were measured to deviate from their nominal values by $\sim 0.1\%$ and were linear ($\leq 0.1\%$ level). The DAC's were calibrated before and after the experiment with a DVM and were shown to be highly linear. The average of the corrected values of the two independent toroids was used as the measure of the total incident charge, and the readouts agreed to typically $-0.08 \pm 0.21\%$ (see Figure 3.13).

Chapter 4
Data Analysis-II

In this section the process of converting the event information into the the cross sections will be described. Corrections were made for the acceptance, target density, detector efficiencies, and dead-time effects. Contributions to the scattering from the aluminum within the target were subtracted. Effects of higher order (in α_{em}) radiative processes were also included. The form factors were then extracted from the cross sections using a Rosenbluth separation technique. Systematic uncertainties will be discussed at the end of the chapter.

4.1 Histogram Analysis

4.1.1 $\Delta\phi$ Sum

The histogram generated by the Pass-1 analysis was binned in $\Delta P/P_0$, $\Delta\theta$, and $\Delta\phi$. Due to the slight kinematic dependence of the cross section on $\Delta\phi$, this was the first variable that was integrated out. The histogram was summed over $\Delta\phi$ for $\Delta\phi_{lo} \leq \Delta\phi \leq \Delta\phi_{hi}$, with $\Delta\phi_{hi} = -\Delta\phi_{lo} = 24$ mr. The ($\Delta P/P_0$,$\Delta\theta$,$\Delta\phi$) event histogram was thus converted into a ($\Delta P/P_0$,$\Delta\theta$) histogram. The acceptance function was similarly converted from 3-dimensions into 2-dimensions.

The physical scattering angle, θ_{scatt}, was a combination of the in-plane angle, $\theta_0+\Delta\theta$, and the out-of-plane, angle $\Delta\phi$. They were related by:

$$\cos(\theta_{scatt}) = \cos(\theta_0 + \Delta\theta)\cos(\Delta\phi) \tag{4.1}$$

To lowest order θ_{scatt} depends only on $\Delta\phi^2$. Thus for $\Delta\phi \ll 1$ knowledge of the average value of $\Delta\phi^2$ is sufficient to correct for this dependence. An array in $\Delta\theta$ of the average value of $\Delta\phi^2$ was stored so this correction could be performed later in the analysis. This histogram was defined as:

$$\mathrm{PHI2}(\Delta\theta) = \frac{\sum_{i,j} \mathrm{HIST3}(\Delta P/P_{0i},\Delta\theta,\Delta\phi_j)\Delta\phi_j^2}{\sum_{i,j} \mathrm{HIST3}(\Delta P/P_{0i},\Delta\theta,\Delta\phi_j)} \tag{4.2}$$

The typical value of PHI2 was $\sim$ (14 mr)^2, which was in agreement with a Monte-Carlo simulation of the spectrometer acceptance. The correction to the cross section due to PHI2 was usually small ($\sim$ 0.5%), and was performed in this manner because it was desirable to place the acceptance cuts along constant values of $\Delta\theta$ and $\Delta\phi$, rather than along lines of constant θ_{scatt}.

4.1.2 $\Delta P/P_0$ Integral

The ($\Delta P/P_0$,$\Delta\theta$) histogram was summed over $\Delta P/P_0$ to obtain the elastic cross section as a function of $\Delta\theta$. It was necessary to integrate over the elastic tail caused by higher order radiative effects. There were, however, background processes at low values of $\Delta P/P_0$ which must be excluded. It was also desirable to limit the $\Delta P/P_0$ integration to the region where the acceptance corrections were small, and eliminate those regions where events were contributed only from scattering from the aluminum endcaps.

The lower bound of the integration, p_{lo}, was set to a minimum $\Delta P/P_0$ value of -3% to avoid the low efficiency acceptance edges. The threshold for π-production occurred at a value of missing mass squared $W^2 = (M_p + M_\pi)^2 \approx 1.152$ (GeV/c)^2. Thus p_{lo} was also limited to be above a value which corresponded to $W^2 = 1.12$ (GeV/c)^2. This allowed for a clear separation of the elastic scattering events from inelastic events, including resolution effects. The high $\Delta P/P_0$ cut, p_{hi}, was chosen to

correspond to a constant W^2 far enough above the elastic peak, $W^2 = M_P^2 \approx 0.88$ $(\mathrm{GeV/c})^2$, to include the entire elastic peak width caused by resolution effects. The values of p_{lo} and p_{hi} were always placed at the edges of the histogram bins to avoid making approximations that are necessary when placing cuts within bins, and they were calculated for each value of $\Delta\theta$. Corrections were then made for the acceptance efficiency of each bin. The number of events, and the associated uncertainty, used for calculating the elastic cross section for each $\Delta\theta$ bin was defined by:

$$\begin{aligned} \mathrm{N}_{el}(\Delta\theta) &= \sum_{\Delta P/P_{0i}=p_{lo}(\Delta\theta)}^{p_{hi}(\Delta\theta)} \frac{\mathrm{HIST2}(\Delta P/P_{0i},\Delta\theta)}{\mathrm{ACC2}(\Delta P/P_{0i},\Delta\theta)} \\ [\Delta\mathrm{N}_{el}(\Delta\theta)]^2 &= \sum_{\Delta P/P_{0i}=p_{lo}(\Delta\theta)}^{p_{hi}(\Delta\theta)} \frac{\mathrm{HIST2}(\Delta P/P_{0i},\Delta\theta)}{[\mathrm{ACC2}(\Delta P/P_{0i},\Delta\theta)]^2} \end{aligned} \tag{4.3}$$

4.1.3 $\Delta\theta$ Average

Corrections were made to the elastic scattering cross section in each $\Delta\theta$ bin for the kinematic dependence of the cross section relative to the center of the acceptance ($\Delta\theta$=0). This made the expectation value of the cross section independent of $\Delta\theta$, so the values could then be averaged across the acceptance based on their statistical weight resulting in the cross section value at $\Delta\theta$=0. The raw cross section (including an overall constant, CR_0, that includes dead-time, target thickness, etc.) was:

$$\begin{aligned} \frac{d\sigma}{d\Omega}_{raw} &= \mathrm{CR}_0\sigma_0 \\ \sigma_0 &= \frac{\sum_i \frac{\sigma_i}{\Delta\sigma_i^2}}{\sum_i \frac{1}{\Delta\sigma_i^2}} \end{aligned} \tag{4.4}$$

where:

$$\begin{aligned} \sigma_i &= \frac{1}{(\Delta\phi_{hi} - \Delta\phi_{lo})} \frac{\mathrm{N}_{el}(\Delta\theta_i)}{\delta\theta_i} \frac{\sigma_{el}^{model}(\theta_0)}{\sigma_{el}^{model}(\theta_i)} \\ \Delta\sigma_i &= \frac{1}{(\Delta\phi_{hi} - \Delta\phi_{lo})} \frac{\Delta\mathrm{N}_{el}(\Delta\theta_i)}{\delta\theta_i} \frac{\sigma_{el}^{model}(\theta_0)}{\sigma_{el}^{model}(\theta_i)} \\ \theta_i &= \cos^{-1}[\cos(\theta_0 + \Delta\theta_i)\cos\left(\sqrt{\mathrm{PHI2}(\Delta\theta_i)}\right)] \end{aligned} \tag{4.5}$$

where σ_{el}^{model} is the e-p elastic scattering cross section using a dipole approximation for the form factors including the effect of the p_{lo} cut of the radiative tail, and $\delta\theta_i$ is the width of the $\Delta\theta$ bin in mr. Corrections for the value of $\langle\phi^2\rangle$ were included in the definition of θ_i. In order to make the analysis of the dummy target runs consistent with the way the Al endcap contributions were handled in the LH2 target runs, the dummy runs were averaged using the same model cross section as the LH2 runs, and the statistical weighting factor, ΔN_{el}, was estimated using the dipole cross section for hydrogen and the acceptance function evaluated at $x = 1$.

4.2 Calculation of Raw Cross Sections

The target thickness, incident charge, dead-time corrections, and efficiencies, were contained within the constant CR_0 in the previous section, defined by:

$$CR_0 = \frac{1}{0.60225} \frac{DT}{(Beam \cdot Eff \cdot t_{LH2} \cdot Acc_{cor})} \tag{4.6}$$

where DT is the electronics and computer dead-time, $Beam$ is the total incident charge (in units of PE$\equiv 10^{15}$ electrons), Eff is the efficiency of the electron cuts and trigger, t_{LH2} is the thickness of the hydrogen in the LH2 target (g/cm^2), and Acc_{cor} includes the corrections for the reduction of the acceptance at large spectrometer angles due to the target length and the momentum dependence of the spectrometer optics described in previous sections. The constant in the denominator was calculated from Avogadro's number and the relevent units such that the final cross sections were measured in nb/sr. In order to treat the measurement of the dummy target runs consistent with the treatment of the aluminum endcap backgrounds of the hydrogen runs, t_{LH2} was set equal to 19.972 cm $\times$0.0.0707 g/cm^3 for the dummy target runs.

4.3 Subtraction of Aluminum Background

After the computation of the elastic cross section for each run, the contribution to the scattering rate from the Al endcaps and flow guides was subtracted. It was necessary to normalize the subtraction to the scattering rate above the elastic peak region of the LH2 runs in order to determine the amount of material the deformed flow guides contributed to the target thickness. After the determination of this normalization, the measured contribution of the aluminum scattering from the dummy target in the elastic region was subtracted from the elastic cross section of the LH2 target. The effect of this material was also included in the calculation of the radiative corrections to an accuracy of $\approx 0.2\%$. Typical corrections to the cross sections for the aluminum background (under the conditions of the reversed hydrogen flow) was $3.0 \pm 0.3\%$; the typical effect of the deformed flow guides on the radiative corrections was $2.0 \pm 0.2\%$, and was negatively correlated with the background subtraction, resulting in a smaller combined uncertainty in the total correction for the aluminum background. Details of this subtraction are presented in Appendix C.

4.4 Radiative Corrections

Corrections for higher order processes in α_{em}, which affect the scattering amplitude beyond the single photon exchange that was assumed in the introduction, were also included. Bremsstrahlung, vacuum polarization, vertex, ionization, and two photon exchange effects were included as corrections to the principle scattering vertex itself, as were radiative processes within the rest of the target material. The procedure for calculating the radiative corrections is outlined in Appendix A. A single number, $RCOR$, related the ideal one-photon exchange cross section to the higher order cross section that was measured:

$$\frac{d\sigma}{d\Omega} = \frac{1}{RCOR} \times \frac{d\sigma}{d\Omega_{raw}} \tag{4.7}$$

This correction depended on the scattering kinematics, target geometry, and the $\Delta P/P_0$-cut applied to the elastic tail. The kinematics corresponded to the values (E_0, θ_0) at the center of the spectrometer acceptance. A list of the radiative corrections is shown in Appendix D.

4.5 Combining Runs of Similar Kinematics

In order to extract the form factors from the cross section measurements using the Rosenbluth separation technique, it was necessary to have cross section measurements at the same value of Q^2 but different values of ε. Actual data, however, is frequently taken at similar, but slightly different, values of Q^2 or ε due to slight inaccuracies in the setting of the beam energy or spectrometer angle during the data taking. The distribution of the Q^2 and ε values is shown in Figure 4.1, represented by the crosses. Small corrections were applied to each cross section to account for the difference between the actual kinematics, (Q_i^2, ε_i), and the "average" kinematics (Q_0^2, ε_0) of each of the kinematic data subsets, represented by the circles in the preceding figure. These corrections were made using a model cross section assuming a dipole form of the form factors:

$$\frac{d\sigma}{d\Omega_i}(Q_0^2, \varepsilon_0) = \frac{d\sigma}{d\Omega_i}(Q_i^2, \varepsilon_i) \times \frac{\sigma^{dipole}(Q_0^2, \varepsilon_0)}{\sigma^{dipole}(Q_i^2, \varepsilon_i)} \tag{4.8}$$

The size of these corrections was usually $< 1\%$.

Different runs at each (Q_0^2, ε_0) were then averaged together, weighted by their statistical uncertainty, to arrive at a single measured cross section at each kinematic point. The average χ^2/dof of these averages was 1.03. Values of the cross sections at each kinematic setting are given in Appendix D.

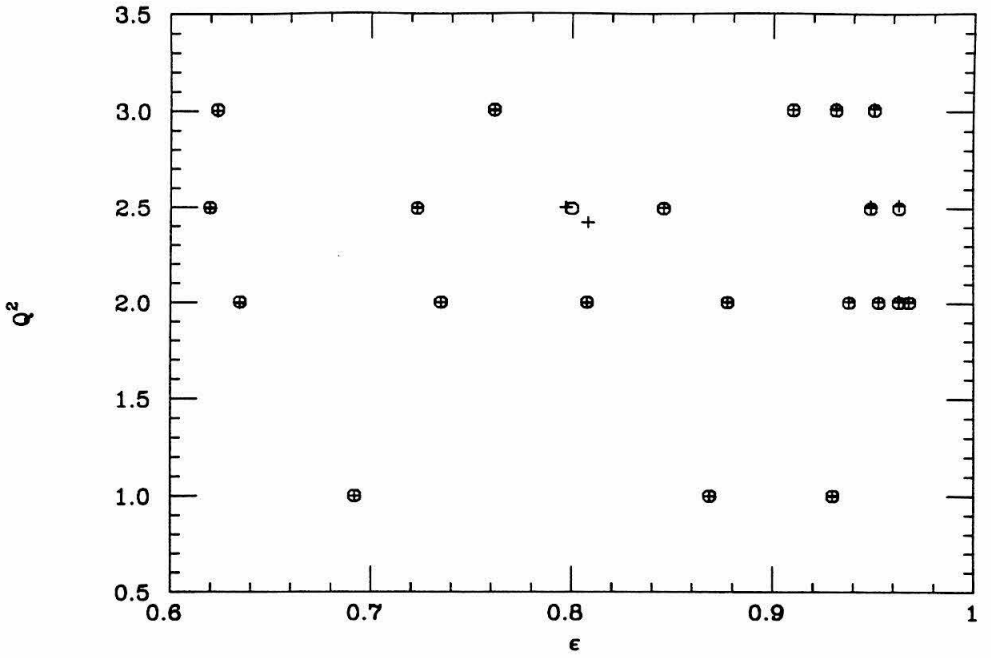

Figure 4.1 – The values of Q^2 and ϵ for each of the data runs are represented by the crosses. The circles represent the nominal values that were used in the form factor extraction.

4.6 Dependence of Cross Sections on Kinematic Cuts

If all the corrections have been properly applied, the measured cross sections should be independent of the $\Delta P/P_0$, $\Delta\theta$ and $\Delta\phi$ cuts used in defining the acceptance region. Any dependence of the cross sections on the kinematic cuts is therefore a good indicator of any errors in the acceptance function and target length corrections, the radiative corrections, or the aluminum background subtraction.

The cross section as a function of $\Delta\phi$, averaged over all runs and normalized to the central region (-10 $\leq \Delta\phi \leq$ 10 mr), is shown in Figure 4.2. The dashed line is the Monte-Carlo prediction of the $\Delta\phi$ dependence due to target length effects. Variations in the cross sections are well accounted for by the Monte-Carlo in the

region of the acceptance that was used in the cross section analysis (-24 $\leq \Delta\phi \leq$ 24 mr). A similar analysis separated in small, medium, and large θ runs indicated that the Monte-Carlo simulation described the $\Delta\phi$ cross section variation in the region of interest at all spectrometer angle settings.

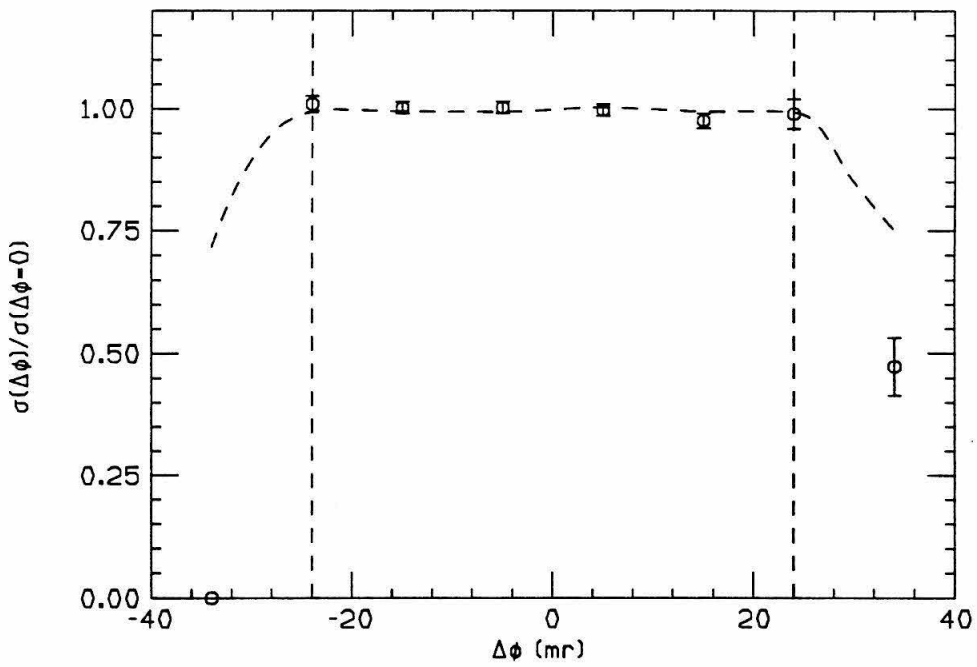

Figure 4.2 – The measured cross section as a function of $\Delta\phi$, averaged over all runs and normalized for small $\Delta\phi$ values. The dashed line is the prediction for the $\Delta\phi$ dependence of the cross section from a Monte-Carlo calculation of the acceptance including target length effects.

The cross section, as a function of $\Delta\theta$, is shown in Figure 4.3. Figure 4.3(a) is averaged over all runs with small scattering angles (11.5° $\leq \theta \leq$ 20°), while Figure 4.3(b) is large scattering angle data (40° $\leq \theta \leq$ 50°). Both were normalized in the region $-6 \leq \Delta\theta \leq 5$ mr. Dips can be seen in the large angle runs near $\Delta\theta = -8$

and $\Delta\theta$=6.5 mr. The Monte-Carlo simulation predicted such an effect in these regions, again due to the target length effects at large angles, although it significantly underestimated their magnitude. Data taken at medium scattering angles also displayed such structures, although smaller in magnitude. These dips occurred in the far edges of the acceptance region where the acceptance efficiency was $\lesssim 50\%$, and the acceptance corrections were large and rapidly changing. In the region of the final acceptance cuts ($-6 \leq \Delta\theta \leq 5$ mr) the cross sections appear to have no systematic $\Delta\theta$ dependence, as predicted by the Monte-Carlo. This indicated a good reliability in both the acceptance function and the cross section model used to correct the kinematic $\Delta\theta$ dependence of the cross section.

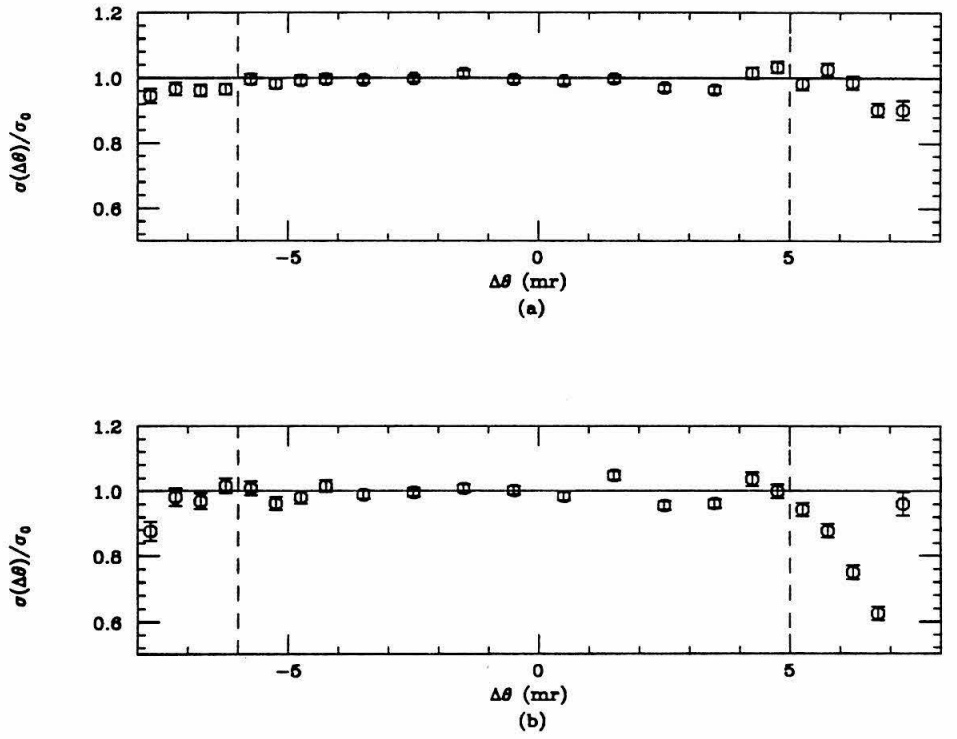

Figure 4.3 – The cross sections as a function of $\Delta\theta$. (a) At small scattering angles. (b) At large scattering angles. The cross sections are independent of $\Delta\theta$ within the final acceptance cuts.

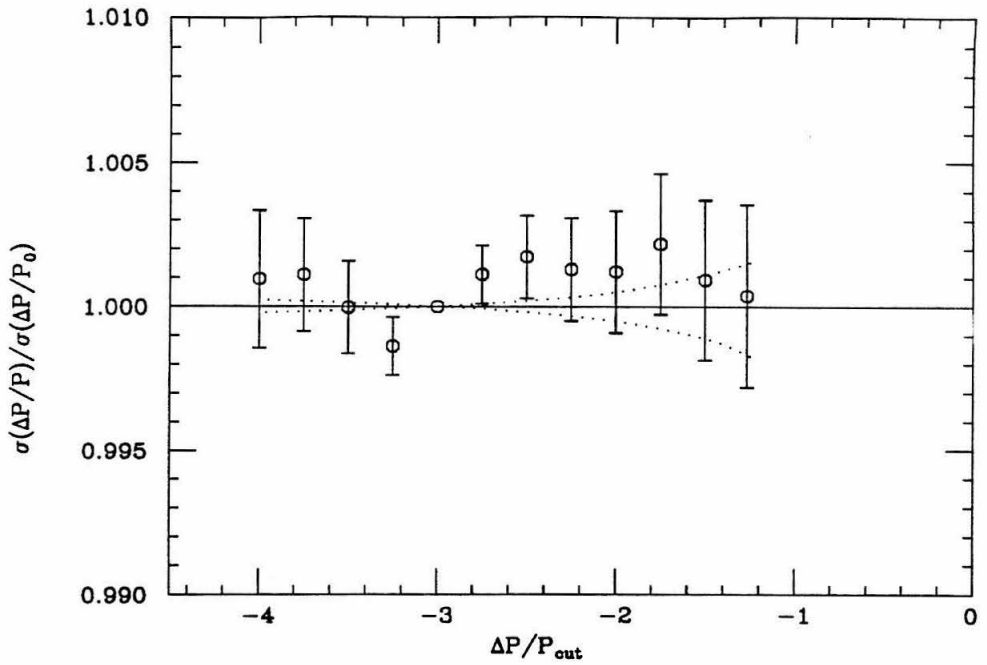

Figure 4.4 – The $\Delta P/P_0$-cut dependence for the measurement of a typical cross section, as discussed in the text. The data is normalized to the cross section value corresponding to a $\Delta P/P_0$-cut of -3.0%. The error bars include only the statistical error relative to this normalization point. The dotted lines are an estimate of systematic uncertainties from other sources.

A typical cross section as a function of the $\Delta P/P_0$-cut, p_{lo}, is shown in Figure 4.4, normalized to the cross section value measured with $p_{lo} = -3.0\%$. Only statistical error bars are shown relative to the normalization point; correlations exist between the values of the other points. The cross section is independent of the elastic tail cutoff within statistical fluctuations. Changes in the raw cross section (before radiative corrections) were $\sim 20\%$ between the lowest and highest cuts shown. The average χ^2/dof between the cross sections evaluated with the lowest $\Delta P/P_0$-cut relative to those with the highest $\Delta P/P_0$-cut was 26.4/22 for all the data runs. If systematic uncertainties due to the kinematic calibration of the elastic peak are included (dotted

line) the average χ^2/dof was reduced to 18.3/22. This indicated a high reliability to the $\Delta P/P_0$-dependence of the radiative corrections and the acceptance function, as well as proper subtraction of the aluminum background.

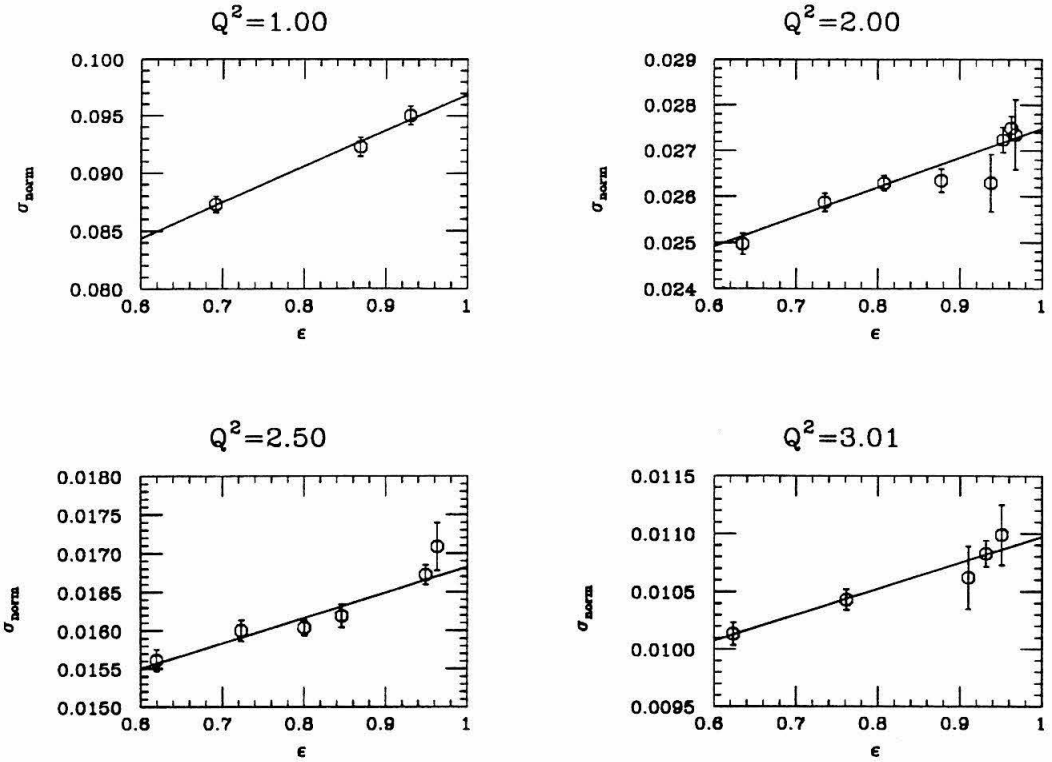

Figure 4.5 – The linear Rosenbluth fits used for extracting the form factors.

4.7 Elastic Form Factor Extraction

The relationship between the cross sections and form factors is:

$$\frac{d\sigma}{d\Omega} = \sigma_{mott}\frac{E'}{E_0}\left(\frac{G_E^2 + \tau G_M^2}{1+\tau} + 2\tau G_M^2 \tan^2(\theta/2)\right) \tag{4.9}$$

This can be rewritten as:

$$\sigma_{norm} \equiv \varepsilon(1+\tau)\frac{E_0}{E'}\frac{1}{\sigma_{mott}}\frac{d\sigma}{d\Omega} \tag{4.10}$$

$$= \tau G_M^2 + \varepsilon G_E^2 \tag{4.11}$$

where ε was defined previously as $\varepsilon = (1+2(1+\tau)\tan^2(\theta/2))^{-1}$ and is the longitudinal polarization of the virtual photon, and σ_{norm} is a function of Q^2 and ε only. A linear fit of σ_{norm} to ε at fixed Q^2 has τG_M^2 as the intercept and G_E^2 as the slope. Graphs of these fits to the data are shown in Figure 4.5. The average χ^2/dof was 0.62.

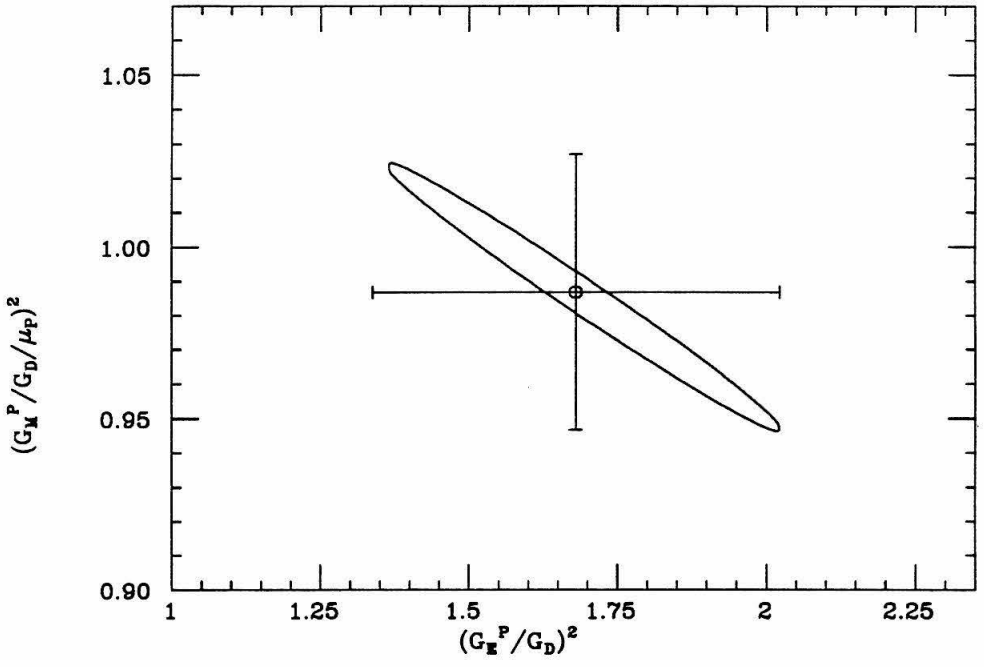

Figure 4.6 – The χ^2 contour plot of G_M^2 vs. G_E^2 for $Q^2 = 3.0$. The point is located where χ^2 is a minimum, the ellipse is the contour for $\chi^2 = \chi^2_{min} + 1$, and the assigned uncertainties in G_M^2 and G_E^2 are shown by the error bars.

In the determination of the uncertainties ΔG_M^2 and ΔG_E^2, the correlations between G_M^2 and G_E^2 involved in the fit have been included. This is shown in the χ^2 contour plot in Figure 4.6, for the $Q^2 = 3$ fit. The error bars are also shown and clearly include the effect of correlations. In table 4.1, the values of τG_M^2 and G_E^2 and their statistical uncertainties are given along with the χ^2/dof.

Q^2 (GeV/c)^2	G_E^2	τG_M^2	χ^2/dof
1.000	3.094E-02 ± 4.292E-03	6.655E-02 ± 3.522E-03	0.50
2.003	6.677E-03 ± 8.427E-04	2.105E-02 ± 6.905E-04	0.67
2.497	3.002E-03 ± 5.398E-04	1.389E-02 ± 4.357E-04	1.01
3.007	2.094E-03 ± 4.598E-04	8.942E-03 ± 3.596E-04	0.19

Table 4.1 – The extracted values of the form factors with statistical errors.

4.8 Systematic Uncertainties

Systematic uncertainties in the scattering kinematics and the operation and understanding of various components of the experimental equipment must be included with the statistical uncertainties of the form factors. The systematic uncertainties can be separated into point-to-point uncertainties, which can change independently from run-to-run or at different kinematics (such as fluctuations in E_0), and absolute uncertainties, which are the same for each data run (such as the absolute value of the acceptance). A presentation of the estimates of the systematic uncertainties and their effects on the form factors is given here.

4.8.1 Point-to-Point Uncertainties

Effects caused by the various point-to-point uncertainties on the values of the form factors were calculated using a Monte-Carlo program. In this program, the parameter in question was adjusted randomly on a run-by-run basis according to a gaussian distribution with a mean of zero and a standard deviation given by the uncertainty in that particular parameter. Changes in the cross section values were then calculated and new values of the form factors were extracted. This process was repeated $\sim$ 1000 times, and the mean difference ($\Delta\mu$) and standard deviation (σ) of

the form factor distribution were determined (in all cases $\Delta\mu \ll \sigma$). The value of σ was used as the estimate of the systematic uncertainty of the form factors. Individual contributions to the total systematic uncertainty were summed in quadrature to estimate the total uncertainty.

Fluctuations in E_0 were typically $\pm 0.05\%$, and were measured with the elastic peak analysis to an accuracy of $\pm 0.03\%$. The scattering angle was determined to an accuracy of $0.003°$, based on the accuracy of the wire array and beam cavity monitors in the beam steering system, and the survey of the spectrometer and wire chambers. The effect of the uncertainties in the incident energy and scattering angle were estimated using the dipole approximation to the form factors. Comparison between the two identical toroid monitors indicated an uncertainty in the incident charge measurement of 0.2%. Uncertainty of the target density was dominated at large beam currents by local beam heating effects, and was estimated at 0.5% at the maximum current of 40 mA. An average uncertainty of 0.2% was assigned to each cross section to account for target density effects. A systematic uncertainty was applied to each cross section equal to half the size of the angle dependent correction for target length effects ($\pm 0.35 \sin^2(\theta)$ %) as a conservative estimate. An additional uncertainty was included for the E' dependence of the acceptance that was measured by the wire orbit of 0.1%. No ε dependent uncertainty of the radiative corrections was included due to difficulty in obtaining a proper estimate of its size. The dominant uncertainties in the radiative corrections were due to ignoring the two-photon exchange terms [29], which have been limited in absolute magnitude [30,31] to be less than $< 1\%$, and the approximations of higher order effects by exponentiating δ_{int} [32], which is again estimated to be $< 1\%$ in absolute magnitude. The table of radiative corrections are provided in Appendix D to allow for improved analysis as the theory of radiative corrections is improved.

Quantity	Uncertainty	$\Delta\sigma/\sigma$ (typical)	$\Delta G_E^p/G_D$ Q^2=1	$\Delta G_E^p/G_D$ Q^2=3
Incident Energy (rel)	±0.03%	±0.34%	±2.2%	±4.4%
Scattering Angle	0.003°	0.10%	0.7%	1.3%
Incident Charge	0.20%	0.20%	1.8%	2.6%
Target Density	0.20%	0.20%	1.8%	2.6%
Endcap Subtraction	0.20%	0.20%	1.8%	2.6%
Acceptance (θ)	<0.20%	0.10%	0.9%	1.3%
Acceptance (E')	0.10%	0.10%	0.9%	1.3%
Pnt-to-Pnt Systematic		0.50%	4.1%	6.7%
Statistical		0.80%	7.1%	13.8%
Incident Energy	0.07%	0.67%	0.3%	0.8%
Scattering Angle	0.003°	0.10%	0.5%	1.2%
Rad. Cor.	1.00%	1.00%	0.5%	0.6%
Acceptance	1.00%	1.00%	0.5%	0.6%
Absolute Systematic		1.57%	0.9%	1.7%

Table 4.2 – The individual systematic uncertainties and their average effect on cross sections (σ) and G_E^p at $Q^2 = 1$ and $Q^2 = 3$.

4.8.2 Absolute Uncertainties

Absolute systematic uncertainties have a small impact on the uncertainties of G_E^p, F_2^p, and any of the ratios of form factors since they have very little ε dependence and thus have relatively small effects compared to statistical or point-to-point systematic fluctuations. However, the absolute values of cross sections and the determination of G_M^p and F_1^p are sensitive to the absolute calibrations since these have relatively small uncertainties from other effects. These absolute uncertainties are discussed here, and are summarized in Table 4.2.

A systematic uncertainty equal to the size of the average incident energy correction based on the elastic peak analysis, 0.07%, was included for the absolute value of E_0. Absolute determination of the scattering angle was limited to ±0.005° based

on the survey of the spectrometer and beamline, the precision of the beam steering system, and the measurement of the spectrometer central ray by the wire orbit. An absolute uncertainty of 0.5% was assigned to the measurement of the integrated incident beam current based on the uncertainty of the charge on the calibration capacitor and previous cross calibrations [33] between the toroids and a Faraday cup that indicated an agreement of better than 0.5%. The acceptance was measured [16,17] to $\pm 1.0\%$ by the wire orbit and the deep inelastic data [11]. Absolute radiative correction uncertainties were estimated [32] at 1%.

Errors caused by using an elastic scattering cross section model based on the dipole approximation in various steps of the analysis were estimated by redoing the entire analysis, but using a form factor model based on the Höhler fit [28]. The form factor values changed by $\lesssim 0.16\%$ in G_E^p and $\sim 0.03\%$ in G_M^p when this was done, indicating that the extracted values were *very* insensitive to the form of this model.

4.9 Final Values of the Form Factors

The values of G_E^p/G_D and $G_M^p/G_D/\mu_p$ are plotted in Figure 4.7 and 4.8, respectively, with $\mu_p = 2.79$ and $G_D = 1/(1 + Q^2/0.71)^2$. Statistical uncertainties are represented by the inner error bar; the outer error bar is statistical and systematic added in quadrature. Values of the form factors are presented, including both statistical and systematic errors, in Table 4.3. Other combinations of the form factors that are commonly used, such as F_1^p, F_2^p, $(\mu_p G_E^p/G_M^p)^2$, $R_{el} \equiv \frac{1}{Q^2}(G_E^p/G_M^p)^2$, and $Q^2(F_2^p/F_1^p)$ are also given.

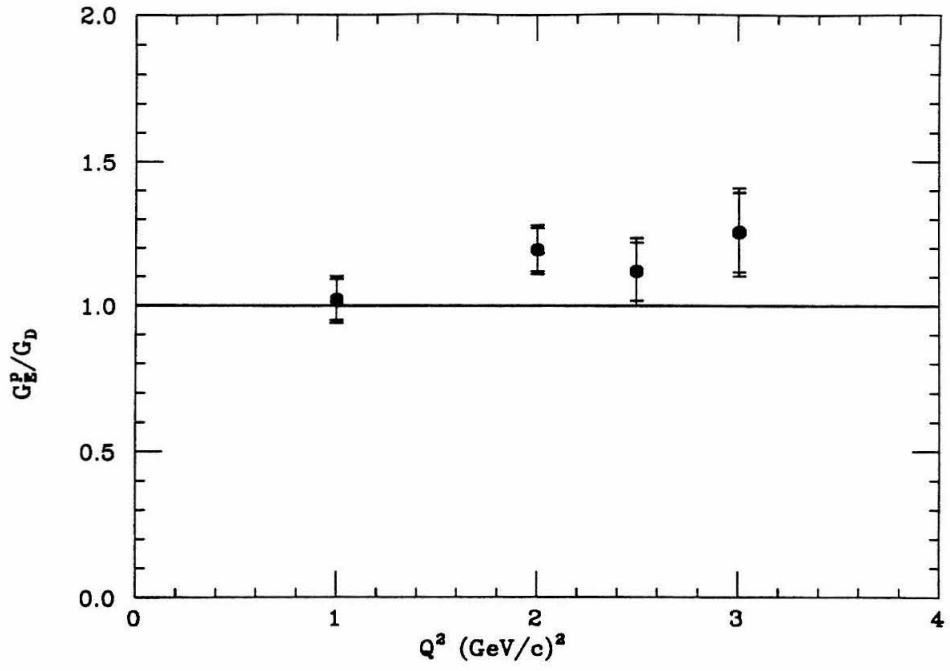

Figure 4.7 – The extracted values of G_E^p/G_D vs. Q^2.

Q^2 (GeV/c)^2	1.000	2.003	2.497	3.007
G_E^p/G_D	1.020E+0 ± 7.1E-2 ± 4.0E-2 ± 9.1E-3	1.193E+0 ± 7.5E-2 ± 4.0E-2 ± 1.5E-2	1.118E+0 ± 1.0E-1 ± 5.8E-2 ± 1.7E-2	1.254E+0 ± 1.4E-1 ± 6.7E-2 ± 1.7E-2
$G_M^p/G_D/\mu_p$	1.006E+0 ± 2.7E-2 ± 1.5E-2 ± 7.3E-3	1.007E+0 ± 1.7E-2 ± 8.8E-3 ± 7.4E-3	1.024E+0 ± 1.6E-2 ± 9.3E-3 ± 7.5E-3	1.005E+0 ± 2.0E-2 ± 9.8E-3 ± 7.4E-3
F_1^p	2.441E-1 ± 6.7E-3 ± 3.8E-3 ± 1.9E-3	1.218E-1 ± 2.2E-3 ± 1.2E-3 ± 1.0E-3	9.013E-2 ± 2.0E-3 ± 1.2E-3 ± 8.0E-4	7.182E-2 ± 1.8E-3 ± 9.0E-4 ± 6.0E-4
F_2^p	1.341E-1 ± 1.1E-2 ± 6.0E-3 ± 1.2E-3	3.942E-2 ± 3.0E-3 ± 1.6E-3 ± 4.6E-4	2.785E-2 ± 2.3E-3 ± 1.4E-3 ± 3.3E-4	1.705E-2 ± 2.1E-3 ± 1.1E-3 ± 2.1E-4
$Q^2(F_2^p/F_1^p)$ (GeV/c)^2	5.494E-1 ± 5.9E-2 ± 3.3E-2 ± 3.5E-3	6.479E-1 ± 6.0E-2 ± 3.2E-2 ± 8.4E-3	7.715E-1 ± 8.1E-2 ± 4.7E-2 ± 1.0E-2	7.138E-1 ± 1.1E-1 ± 5.2E-2 ± 9.8E-3
R_{el}	4.650E-1 ± 8.9E-2 ± 5.0E-2 ± 5.3E-3	3.172E-1 ± 5.0E-2 ± 2.7E-2 ± 7.1E-3	2.160E-1 ± 4.6E-2 ± 2.6E-2 ± 5.8E-3	2.342E-1 ± 6.1E-2 ± 3.0E-2 ± 5.7E-3
$(\mu_p G_E^p/G_M^p)^2$	1.028E+0 ± 2.0E-1 ± 1.1E-1 ± 1.2E-2	1.404E+0 ± 2.2E-1 ± 1.2E-1 ± 3.2E-2	1.192E+0 ± 2.5E-1 ± 1.5E-1 ± 3.2E-2	1.556E+0 ± 4.0E-1 ± 2.0E-1 ± 3.8E-2

Table 4.3 – Values of the form factors, including statistical, point-to-point systematic, and absolute systematic uncertainties.

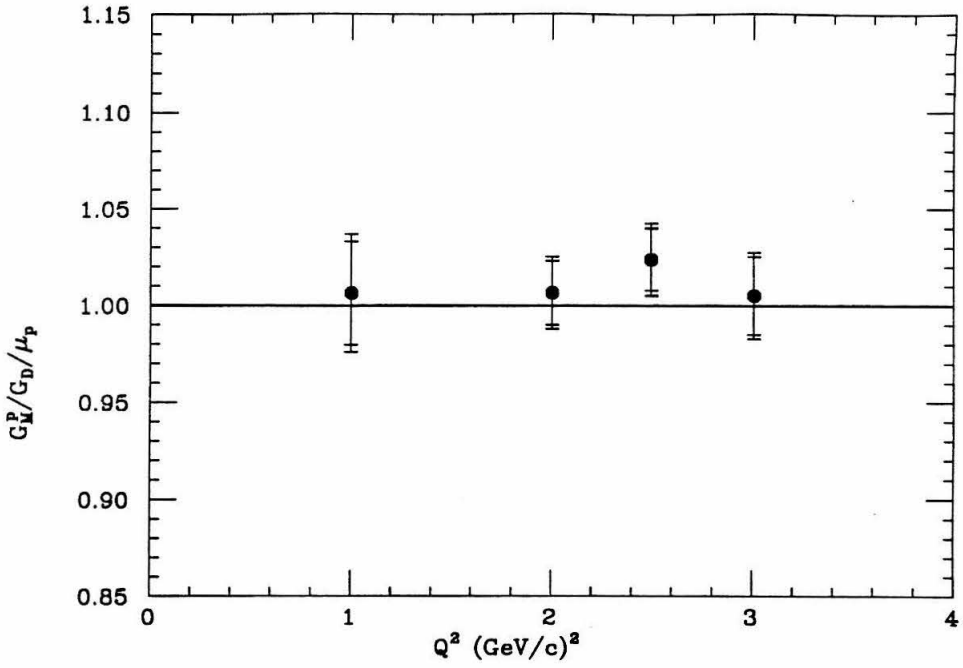

Figure 4.8 – The extracted values of $G_M^p/G_D/\mu_p$ vs. Q^2.

Chapter 5
Comparisons to Previous Data and Theories

5.1 Previous Measurements

In this section the data from selected previous measurements of *e-p* elastic scattering will be presented. The experiments are limited to those that provide a suitable range of ε values to allow for the form factor extraction at $Q^2 > 1$ (GeV/c)^2, although a significant body of lower Q^2 data will also be included. First a brief overview of each of the experiments will be presented, including a few of the important experimental details, the prescription used for calculating radiative corrections, the kinematic range covered, and the relative uncertainty in cross sections. See Appendix A for the details

of the radiative corrections procedure used for this experiment. Comparisons will be made between the form factors extracted from this work and some of the previous experiments. All the previous data will then be combined with the data from this experiment and a global fit to the form factors will be performed. The extracted form factors will be presented for a wide range of Q^2 values, along with the relative normalizations for the different experiments. The cross sections used from these previous experiments are presented in Appendix D.

5.1.1 Overview of Previous Experiments

Eleven different experiments were chosen as representing the essential elastic *e-p* data taken in the last 25 years for $Q^2 > 1$ (GeV/c)^2. These experiments are presented here in chronological order under the name of the principal author. Kinematics and cross sections for each of the experiments are listed in Appendix D.

Janssens, et al.,*1966* [34]

Data was taken at the Stanford Mark III linear accelerator with a 0.953 cm liquid hydrogen target. Scattered electrons were detected in a 72 inch double-focusing magnetic spectrometer with a momentum acceptance of 3.5%. Cross sections were measured at 25 different Q^2, of which 20 were suitable for performing an ε separation, covering a range of Q^2 of $0.15 \leq Q^2 \leq 0.86$ (GeV/c)^2. The incident energy ranged from $0.25 \leq E_0 \leq 1.0$ GeV. Typically 3-5 ε points were taken at each Q^2, covering an angular range of $45° \leq \theta \leq 145°$. Single ε points were taken at $\theta \approx 145°$ and Q^2 values of 1.01, 1.09, and 1.17 (GeV/c)^2. Radiative corrections were calculated using the method of Tsai [29] for the internal contributions and of Schwinger [35,36] for the external contributions. Uncertainties in cross section values were typically 5.0%, although they were slightly larger at the higher Q^2 points. An overall normalization uncertainty of 1.6% was also reported.

Bartel, et al., *1966* [37]

This experiment was the first of two performed by Bartel and collaborators at DESY that will be presented here. An electron beam provided by the 6-GeV synchrotron was focused onto a 5 cm liquid hydrogen target. Scattered electrons were detected by a magnetic spectrometer that could be rotated around the target pivot. The spectrometer had an angular acceptance of ± 12 mr in the horizontal plane, ± 9 mr in the vertical plane, and a momentum acceptance of $\pm 2\%$. A total of 8 different Q^2 measurements were done in the range $0.39 \leq Q^2 \leq 4.1$ (GeV/c)^2. The incident energy ranged from $3.6 \leq E_0 \leq 5.9$ GeV. The measurements were all done at relatively small scattering angles, $10° \leq \theta \leq 25°$. Usually only one ε point was taken at each Q^2, and the maximum spread in angle at a fixed Q^2 was only 4°, so an independent extraction of the form factors from this data alone was not possible. Radiative corrections were made using the method of Meister and Yennie [38]. Typical uncertainties in cross sections were 3.0%, with an additional absolute normalization uncertainty of 3.5%.

Albrecht, et. al., *1967* [4]

This data was also taken at DESY, with an electron beam incident on a cylindrical liquid hydrogen target [39]. A doubly focusing spectrometer was used to detect the final electrons. Only three measurements of the elastic cross sections were done; at $Q^2 = 1.95$, 2.92, and 9.56 (GeV/c)^2, all performed at $\theta \approx 76°$. The incident energy ranged from $1.7 < E_0 < 6.2$ GeV. Again, no independent extraction of the form factors from this experiment was possible. However, the first two data points could be combined with the data of Bartel 1966 to perform an ε separation. This extraction was dominated by the normalization uncertainties. The highest Q^2 data point was used to extract G_M^p under the assumption $G_E^p = G_M^p/\mu_p$. Radiative corrections were

carried out using the prescription of Meister and Yennie [38]. The two lower Q^2 cross sections had uncertainties of 4.3%; the highest Q^2 point uncertainty was 14.1%. An overall normalization uncertainty of 4% was also included.

Litt, et al. *1970* [40]

This experiment was performed at SLAC with electrons of incident energies $3.0 \leq E_0 \leq 10$ GeV scattered from a 23 cm liquid hydrogen target. The same 8-GeV spectrometer in End Station A that was used in the present experiment was used by Litt, *et al.* Cross sections were measured at $Q^2 = 1.00, 1.50, 2.00, 2.50$, and 3.75 with scattering angles of $12° \leq \theta \leq 42°$. Corrections were made for straggling in the target using the prescription of Eyges [41] and internal radiative processes using the prescription of Tsai [29], which was found to be consistent with Meister and Yennie [38], within the experimental error bars. Typically 3-5 ε points were measured at each Q^2. Cross section uncertainties were $\sim$ 1.5-2.0%, with a normalization uncertainty of 4.0%.

Goitein, et al., *1970* [42]

This experiment, performed by Harvard University at the Cambridge Electron Accelerator, used a liquid hydrogen target. Both the scattered electron and the struck proton were detected. The electron spectrometer had a momentum acceptance of 14% with a solid angle of 0.83 msr. Scattering angles ranged from $19° \leq \theta \leq 34°$, with the proton recoil angle ranging from $24° \leq \theta_p \leq 65°$. Good agreement was found between the cross sections measured with the electron arm only and those measured with the additional requirement of a coincident proton. The incident beam energy ranged from $1.6 \leq E_0 \leq 6.0$ GeV. A total of six Q^2-values were measured, from $0.27 \leq Q^2 \leq 5.9$ (GeV/c)^2. Once again, a sufficient ε range was not available to extract the form factors from this experiment alone. Internal corrections were done

with the method of Meister and Yennie [38], and bremsstrahlung corrections with the method of Bjorken [43]. Cross section uncertainties were $\sim 4\%$, with an overall normalization uncertainty of 2.2%.

Berger, et al., *1971* [44]

This experiment was performed at the Physikalisches Institut of the University of Bonn. A liquid hydrogen target 5 cm in diameter [45] scattered electrons into a magnetic spectrometer with solid angle 0.507 msr that could be rotated around the target pivot. The incident energy ranged from $0.66 \leq E_0 \leq 1.91$ GeV. Data were taken at approximately 14 different Q^2, from $0.1 \leq Q^2 \leq 1.95$ $(\mathrm{GeV/c})^2$. Some of the very low Q^2 data was taken exclusively at small angles, $\theta \approx 30°$, to provide a normalization to other experiments. Anywhere from 3 to 14 different ε points were taken at the medium and high Q^2 values, covering a maximum angular separation of $25° \leq \theta \leq 111°$. At the highest Q^2 points, only relatively large θ measurements were performed, with the intention of combining this data with other experiments performed at smaller scattering angles and extracting the form factors. Radiative corrections were done with the prescription of Meister and Yennie [38] for the internal, including the energy dependence of the elastic cross section in the internal bremsstrahlung terms [46], and Heitler [47] for the bremsstrahlung contributions. The cross section uncertainties ranged from 2-6%, with a normalization uncertainty of 4%.

Price, et al., *1971* [48]

This experiment was also performed at the Cambridge Electron Accelerator with an experimental group similar to the one of Goitein, *et al.* Data was usually taken at $\theta \approx 90°$ at 6 different Q^2 values ranging from 0.25 to 1.75 $(\mathrm{GeV/c})^2$. The incident energy ranged from $0.45 \leq E_0 \leq 1.6$ GeV. The radiative corrections were calculated

using the equivalent radiator method of Mo and Tsai [32], with additional corrections applied from Meister and Yennie [38] and Yennie, Frautschi, and Suura [49]. Typical cross section uncertainties were $\sim 4\%$ with a normalization uncertainty of 1.9%.

Kirk, et al., *1973* [13]

This experiment was performed at SLAC in the End Station A using the 8 GeV spectrometer. The principal purpose of this experiment was to extract G_M^p at large momentum transfers ($1 \leq Q^2 \leq 25$ (GeV/c)^2), under the assumption that $G_E^p = G_M^p/\mu_p$, where the contribution of G_E^p to the cross section was expected to be small. Incident energies ranged from $4 \leq E_0 \leq 17.3$ GeV with scattering angles $12° \leq \theta \leq 35°$. Five liquid hydrogen targets were used, and were vertical cylinders 8-32 cm in diameter. Radiative corrections were carried out with the prescription of Tsai [29] for the internal part and Eyges [41] for the external part. Additional correction terms (such as the contribution to the internal corrections due to the energy dependence of the elastic cross section) are described by Kirk, *et al.* [13]. Typical cross section uncertainties were 2% at low Q^2, and the absolute normalization uncertainty was estimated at 4%. Although most of this data was far beyond the range of Q^2 where a reliable determination of G_E^p is possible for the purposes of this paper, data at low values of Q^2 are used to provide a cross calibration of this experiment with other experiments. In addition, some of the higher Q^2 data ($Q^2 = 5.1$ and 10 (GeV/c)^2), combined with large angle measurements from some of the other experiments at similar Q^2 values, is used to determine an upper limit on the value of G_E^p. This is the first data on G_E^p for Q^2 values above 4 (GeV/c)^2.

Bartel, et al., *1973* [3]

This second set of data measured by Bartel, *et al.*, was also done at DESY. Three spectrometers were used to measure the *e-p* elastic cross sections. A small

angle electron spectrometer was set at $\theta \approx 12°$. The solid angle was 0.44 msr, and the momentum acceptance was $\pm 2.5\%$. A large angle electron spectrometer was set at $\theta = 86°$, with a solid angle of 21.0 msr and a momentum acceptance of $\pm 5.5\%$. An additional recoil nucleon detector was rotated to an angle corresponding to an electron scattering angle of $\theta = 86°$. This was used as an independent measurement of the scattering cross section. Data was taken at $Q^2 = 0.67$, 1.00, 1.17, 1.50, 1.75, 2.00, 2.33, and 3.00 $(\mathrm{GeV/c})^2$, corresponding to incident electron energies of $0.8 \leq E_0 \leq 6.5$ GeV. Radiative corrections were calculated from Meister and Yennie [38] for the internal and Mo and Tsai [32] for the external. Contributions from the energy dependence of the elastic cross section in the internal corrections [32] were also included. The major source of uncertainty in this experiment was the cross section normalization between the small and large angle spectrometers, which was estimated at 1.5%. Typical cross section uncertainties were 2-4%, with an absolute normalization uncertainty of 2.1%.

Sill, et al., *1986* [50,51]

This experiment was performed at SLAC in the End Station A using the 8 GeV spectrometer. The principal purpose of this experiment was to extract G_M^p at large momentum transfers $(2.8 \leq Q^2 \leq 31.3\ (\mathrm{GeV/c})^2)$, similar to the experiment of Kirk, *et al.*. Electron beams with energies of $5.5 \leq E_0 \leq 21$ GeV were incident on one of two liquid hydrogen targets with lengths of 25 and 65 cm. Scattering angles ranged from $21° \leq \theta \leq 33°$. Radiative corrections were carried out using the prescription of Mo and Tsai [32] for the internal and Tsai [52] for the external. Typical cross section uncertainties were 3-4%, with a normalization uncertainty of 3.6%. Again, most of this data was far beyond the range of Q^2 where a reliable determination of G_E^p is possible for the purposes of this paper, but data at $Q^2 = 2.9$ and $Q^2 = 3.7$ $(\mathrm{GeV/c})^2$ is used to provide a cross calibration of this experiment with other experiments; and

some of the higher Q^2 data (Q^2 = 5.0 and 9.7 (GeV/c)^2) is used to determine an upper limit on the value of G_E^p at large Q^2.

Katramatou, et al., *1987* [53,54]

This data was taken at SLAC in the End Station A as subset of *e-d* elastic data. A 180° back angle electron spectrometer and a 0° nucleon recoil spectrometer were built on the floor of the experimental area, with solid angles 22.5 and 5.9 msr, respectively, and momentum acceptances of ±4% and ±1.5%, respectively. At these kinematics the cross section is completely dominated by G_M^p; there is no contribution from G_E^p. Thus the cross section measurement is an unambiguous measurement of the magnetic form factor and no Rosenbluth separation is necessary. The incident beam ranged in energy from $0.5 \leq E_0 \leq 1.3$ GeV, which allowed measurements over a range of $0.5 \leq Q^2 \leq 1.8$ (GeV/c)^2. Various liquid hydrogen targets were used with lengths from 10 to 40 cm. Radiative corrections were carried out using the equivalent radiator approximation of Tsai [52] for the internal contributions combined with the effect [52] of bremsstrahlung and Landau straggling in the external radiators of the target. The effect of bremsstrahlung energy loss before the scattering vertex and the energy dependence of the elastic cross section was included. The cross sections uncertainties ranged from 2-3%, with an absolute normalization uncertainty of 1.8%.

5.1.2 Comparison to Previous Form Factor Measurements

In this section a comparison will be made between the form factors that were measured in this experiment and the form factors that were extracted from the previous data. Only those experiments that measured a sufficient ε range to extract the form factors will be included; no cross normalizations between small and large θ

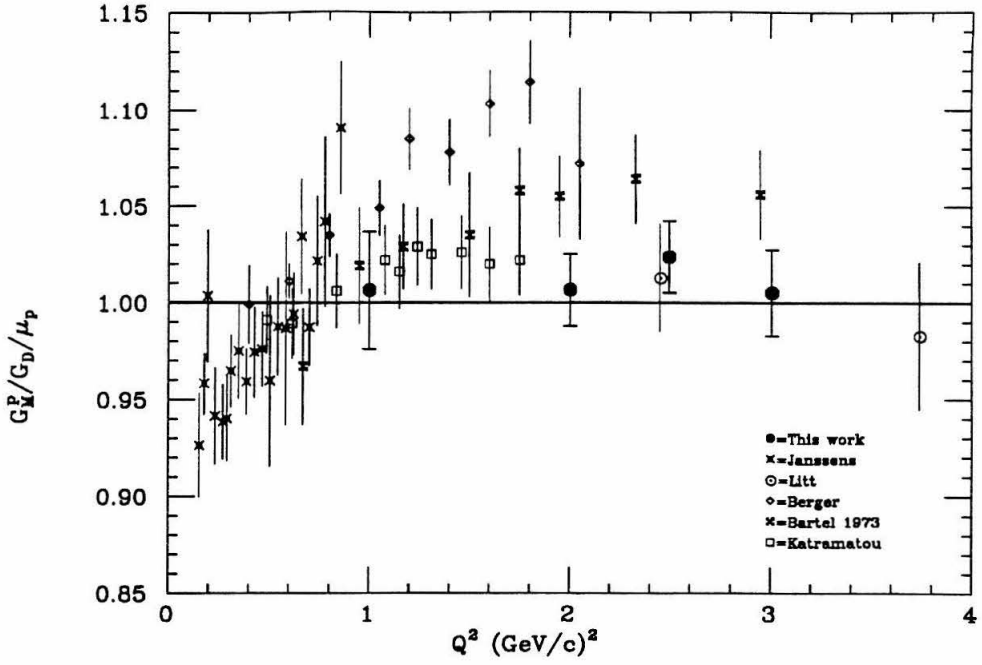

Figure 5.1 – The measurement of $G_M^p/G_D/\mu_p$ vs. Q^2 from this work, along with the data of Janssens, Litt, Berger, Bartel 1973, and Katramatou.

measurements of different experiments will be done. That will be performed in the following section.

In Figure 5.1, the results for $G_M^p/G_D/\mu_p$ are shown for this work along with the results of the ε-separations of Janssens, Litt, Berger, and Bartel-1973. The data of Katramatou is also included since at $\theta = 180°$ the cross section is only dependent on G_M^p. No ε-separation was required for this data, which eliminates many of the systematic uncertainties involved in a Rosenbluth extraction of the form factors. Our data tends to fall somewhat below the results of Bartel-1973 and Berger, but is in good agreement with Katramatou and Litt. Janssens' data lies at too low a value of Q^2 to make a meaningful comparison, except to point out that the data point

at Q^2=0.86 (GeV/c)^2 seems anomalously large. Results for G_M^p are sensitive to the absolute normalization of cross sections, which have not been included in the error bars.

Results for G_E^p/G_D are shown in Figure 5.2 for the same experiments as the G_M^p plot, with the exception of Katramatou. Our data tends to lie above the data of Bartel 1973 with a discrepancy of about two sigma. This is strongly correlated with the discrepancy in the G_M^p results. Our data is in moderately good agreement with the results of Berger and Litt.

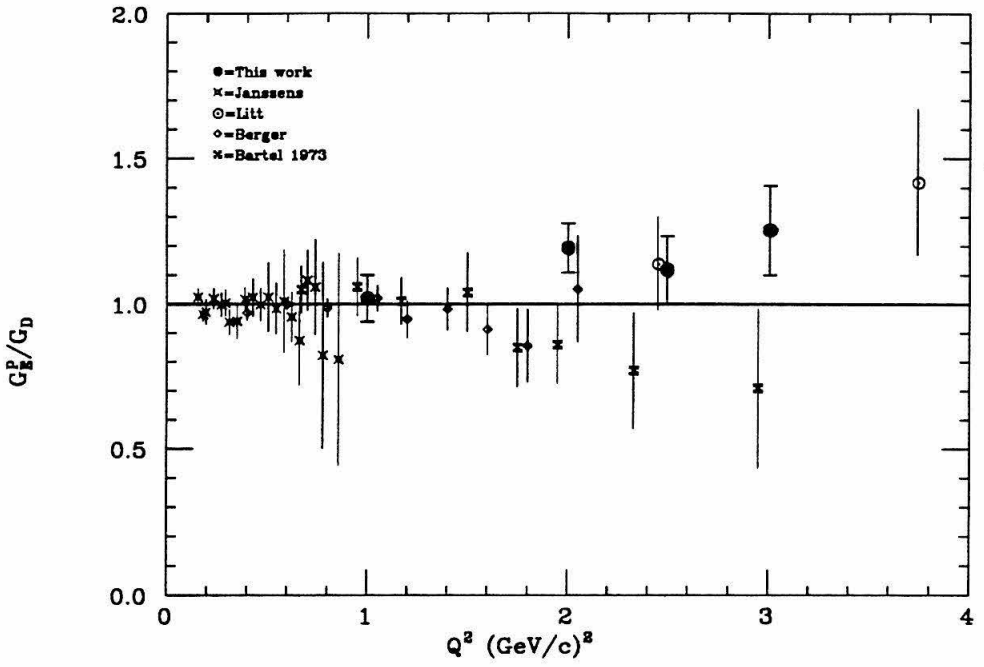

Figure 5.2 – The measurement of G_E^p/G_D vs. Q^2 from this work, along with the work of Janssens, Litt, Berger, and Bartel 1973.

Experiment	η	$\Delta\eta$
Janssens	0.983 ± 0.009	0.016
Bartel, 1966	0.994 ± 0.011	0.035
Albrecht	0.976 ± 0.025	0.040
Litt	1.005 ± 0.004	0.040
Goitein	0.973 ± 0.010	0.022
Berger	0.994 ± 0.007	0.040
Price	0.966 ± 0.012	0.019
Kirk	1.002 ± 0.009	0.040
Bartel, 1973	0.993 ± 0.006	0.021
Sill	1.006 ± 0.018	0.036
Katramatou	1.017 ± 0.011	0.018

Table 5.1 – Relative normalizations between each of the previous experiments and this work. Absolute systematic uncertainties for each of the experiments are also given.

5.1.3 World Fit to Elastic Form Factors

All of the data from the previous experiments (compiled in Appendix D) was combined with the data of this experiment to perform a global fit. From this fit, G_E^p and G_M^p were extracted at 28 different values of Q^2, along with the ten normalization constants between each of the experiments and this work. Cross sections were corrected for differences between the measured and nominal Q^2 values using the dipole approximation (typically $\sim 10\%$). After the form factors were extracted, the fit was re-iterated using these new values of the form factors. Values of the extracted form factors did not change significantly. The fit was done by minimizing χ^2, where χ^2 was defined by:

$$\chi^2 \equiv \sum_{i=1}^{N_{exp}} \sum_{j=1}^{N_{Q2}} \sum_{\varepsilon_{ijk}} \left\{ \frac{\eta_i \sigma_{norm}^{ijk} - \left[\tau_j G_M^2(Q_j^2) + \varepsilon_{ijk} G_E^2(Q_j^2) \right]}{\Delta\sigma_{norm}^{ijk}} \right\}^2$$

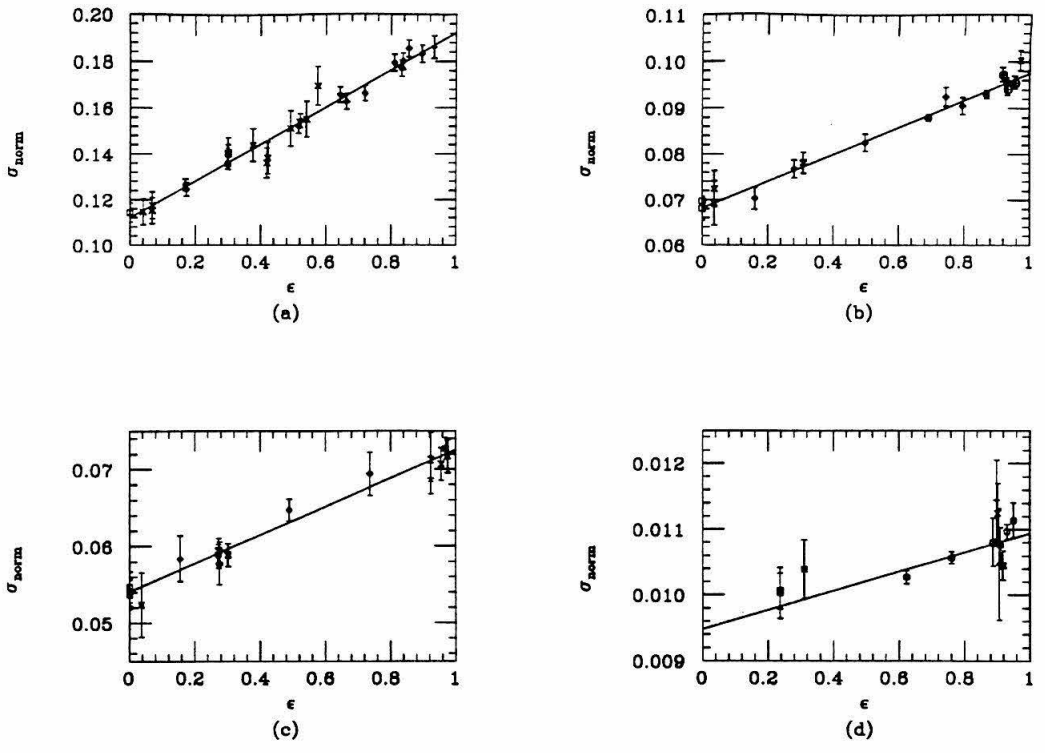

Figure 5.3 – Four typical ϵ separation plots for the form factor extraction at: (a) $Q^2 = 0.60$; (b) $Q^2 = 1.00$; (c) $Q^2 = 1.20$; and (d) $Q^2 = 3.00$ (GeV/c)^2.

$$+ \sum_{i=1}^{N_{exp}-1} \left(\frac{\eta_i - 1}{\Delta\eta_i} \right)^2 \tag{5.1}$$

where the definitions are similar to those of equation 4.10. The values of η_i are the normalization constants, and $\Delta\eta_i$ is the absolute cross section uncertainty given for each experiment. The cross section error bars ($\Delta\sigma^{ijk}_{norm}$) included both statistical and point-to-point systematic uncertainties. All the variables in the above equation (η_i, $G^p_E(Q^2_j)$, and $G^p_M(Q^2_j)$) were simultaneously fit to minimize χ^2.

The total χ^2 for the fit was 172 for 211 degrees of freedom, indicating a conservative estimate of the systematic uncertainties. A few typical ε separation plots are shown in Figure 5.3. Relative normalization constants for the experiments are given

in Table 5.1. Values of G_E^p/G_D and $G_M^p/G_D/\mu_p$ are given in Table 5.2 at each Q^2 value, along with the χ^2/dof that was contributed from each of the Q^2 points. This data is also plotted in Figures 5.4 and 5.5.

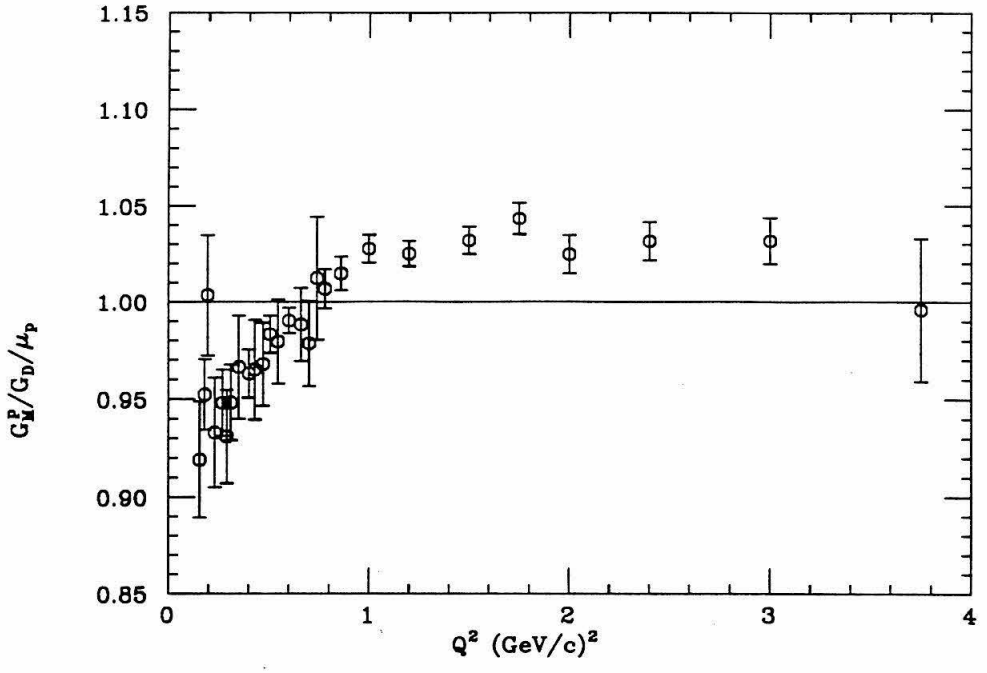

Figure 5.4 – The values of $G_M^p/G_D/\mu_p$ vs. Q^2 from the world fit. The data for $Q^2 > 4$ (GeV/c)^2 are not shown.

The normalization constants are well within the systematic uncertainty assigned by each experiment; only Price shows more than a one sigma deviation from a value of $\eta_i = 1.0$. In addition, excellent agreement is found between the normalizations of experiments done at the same facilities: the SLAC 8 GeV spectrometer data (Litt, Kirk, Sill, and this work), DESY experiments (Bartel 1966, Albrecht, and Bartel 1973), and the CEA work (Goitein and Price). This result, coupled with the small values of χ^2/dof for the fit, tends to indicate that a single normalization constant for

Q^2 (GeV/c)^2	G_E^p/G_D	$G_M^p/G_D/\mu_p$	χ^2/dof
0.155	1.017 ± 0.028	0.919 ± 0.030	0.17/1
0.180	0.957 ± 0.026	0.952 ± 0.018	0.96/5
0.195	0.935 ± 0.026	1.003 ± 0.031	1.83/3
0.230	1.012 ± 0.034	0.933 ± 0.028	0.88/2
0.270	0.953 ± 0.023	0.948 ± 0.017	7.91/6
0.290	0.997 ± 0.045	0.931 ± 0.024	0.44/3
0.310	0.964 ± 0.026	0.948 ± 0.019	2.22/4
0.350	0.931 ± 0.067	0.966 ± 0.026	0.07/1
0.400	0.976 ± 0.017	0.963 ± 0.012	9.91/15
0.430	1.016 ± 0.064	0.965 ± 0.026	0.54/1
0.470	0.973 ± 0.056	0.968 ± 0.021	1.68/4
0.505	0.969 ± 0.026	0.983 ± 0.010	3.84/3
0.545	0.980 ± 0.071	0.979 ± 0.022	4.60/3
0.600	0.961 ± 0.016	0.990 ± 0.007	11.9/25
0.660	0.969 ± 0.044	0.988 ± 0.019	2.78/3
0.700	1.074 ± 0.086	0.979 ± 0.022	1.43/4
0.740	1.051 ± 0.155	1.012 ± 0.032	0.80/1
0.780	0.956 ± 0.030	1.007 ± 0.010	20.2/16
0.860	1.212 ± 0.094	1.015 ± 0.009	12.8/3
1.000	0.967 ± 0.023	1.028 ± 0.007	14.0/16
1.200	1.012 ± 0.032	1.025 ± 0.007	5.44/14
1.500	1.048 ± 0.031	1.032 ± 0.007	7.49/14
1.750	0.017 ± 0.071	1.043 ± 0.008	8.00/9
2.000	1.105 ± 0.047	1.025 ± 0.010	14.6/17
2.400	1.063 ± 0.062	1.032 ± 0.010	14.7/17
3.000	1.050 ± 0.099	1.032 ± 0.012	11.1/11
3.750	1.358 ± 0.186	0.996 ± 0.037	3.54/6
5.100	< 2.17 (95% CL)	1.047 ± 0.083	0.38/3
9.600	< 3.24 (95% CL)	0.875 ± 0.097	0.60/1

Table 5.2 – The extracted values of the form factors from the world fit at each Q^2, relative to the dipole fit. The χ^2/dof for each of the Q^2 values is also shown. The error bars include statistical and point-to-point systematic uncertainties. An overall normalization uncertainty of 1-2% has not been included.

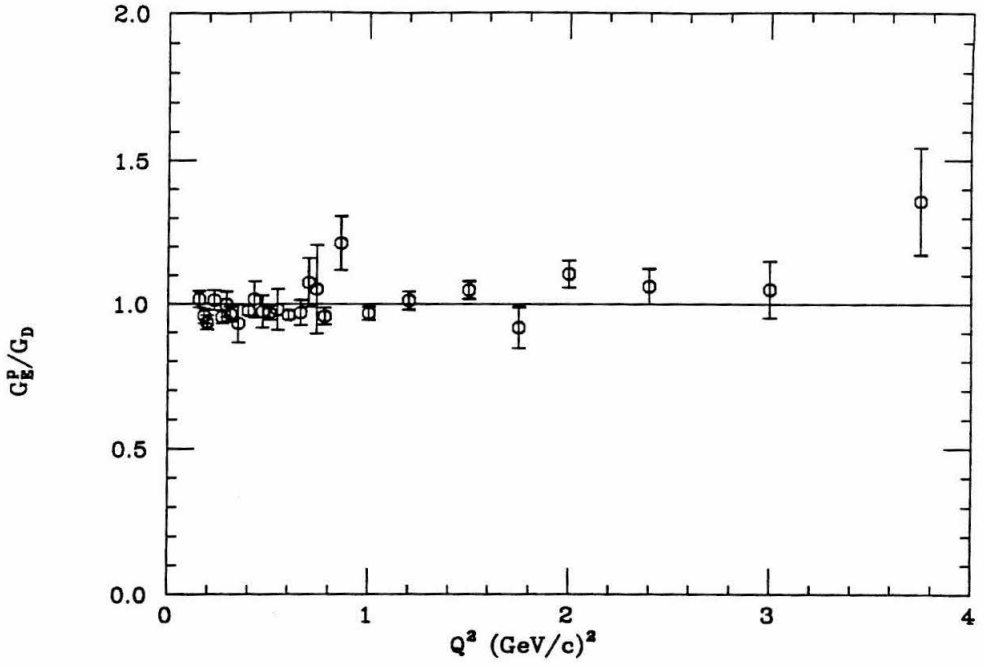

Figure 5.5 – The values of G_E^p/G_D vs. Q^2 from the world fit. The upper limits at $Q^2 > 4$ (GeV/c)^2 are not shown.

each experiment was a good correction for the systematic differences between each of the data sets.

Values of G_M^p are very similar to previously published results. For $Q^2 < 1$ (GeV/c)^2 it lies below the dipole, rising quickly to a point that is a few percent above the dipole. At larger values of Q^2, it again falls below the dipole, although much of that data has not been included here. The data on G_E^p, which have substantially reduced error bars compared to previous results, is nearly constant relative to the dipole; in fact, it tends to rise slightly above the dipole approximation. This is in sharp contrast to the interpretation generally given to previous experimental results, which have been used as an indication that G_E^p/G_D tends to decrease with increasing Q^2 above $Q^2 = 1$ (GeV/c)^2. However, these results were usually $\sim$ 1-σ away from a

value of 1.0, and were dominated by systematic uncertainties involved in cross normalizations between different spectrometers or different experiments. These systematic uncertainties affected the data at the different Q^2 values in a highly correlated way. Data from this experiment alone, which is dominated by statistical uncertainties, combined with this world fit, would seem to indicate that G_E^p/G_D does not fall below 1.0 for $Q^2 < 4$ (GeV/c)^2. At $Q^2 = 0.86$ (GeV/c)^2, the value of G_E^p seems somewhat anomalous. This is related to the anomalous G_M^p value extracted from Janssens, and is reflected in the value of χ^2/dof for this point.

5.2 Theories and Parameterizations

A number of different approaches have been developed to try to understand the nucleon elastic form factors. Low Q^2 data have been interpreted in terms of the spatial distributions of the charge and magnetic moment distributions, such as the rms radius of the proton. Moderate Q^2 data have been viewed in the light of vector meson dominance which models the virtual photon as a sum of massive vector mesons. The Q^2 dependence of the form factors is thus, in part at least, caused by the Q^2 dependence of the meson propagator terms. Models involving higher twist effects, such as diquarks, also make specific predictions for the elastic form factors at moderate Q^2. Large Q^2 data have been compared to perturbative QCD predictions and dimensional scaling laws, and has been interpreted as confirmation of the quark/parton model of the nucleon and the success of quark counting rules. These various approaches will be discussed here, and comparisons to measurements will be made at the end of this section.

5.2.1 Dipole Approximation and Form Factor Scaling

The elastic form factors of point particles, such as muons, have no Q^2 dependence. But for particles with non-zero size, such as protons, the form factors decrease with increasing Q^2 as the virtual photon begins to probe distance scales comparable to or smaller than the size of the particle. The dipole approximation is a lowest order attempt to incorporate the non-zero size of the proton into the form factors.

It is assumed, in this model, that the proton has a simple exponential spatial charge distribution:

$$\rho(r) = \rho_0 e^{-r/r_0} \tag{5.2}$$

where r_0 is the scale of the proton radius ($\langle r^2 \rangle = 12 r_0^2$) and $\rho_0 = \frac{1}{8\pi r_0^3}$ is the normalization constant. The form factors are related, in the non-relativistic limit, to the Fourier transform of the charge and magnetic moment distribution. The dipole form factor, G_D, can thus be defined by:

$$\begin{aligned} G_D(\mathbf{q}^2) &= \int e^{i\mathbf{q}\cdot\mathbf{r}} \rho(\mathbf{r}) d^3\mathbf{r} \\ &= \frac{1}{(1+\mathbf{q}^2 r_0^2)^2} \end{aligned} \tag{5.3}$$

where $\mathbf{q}^2$ is the three-momentum of the virtual photon squared. In the non-relativistic limit ($\nu \ll M_p$), the approximation $\mathbf{q}^2 = Q^2 + \nu^2 = Q^2(1 + \frac{\nu}{2M_p}) \approx Q^2$ can also be made. If it is also assumed that the magnetic moment distribution has the same spatial dependence as the charge distribution (*i.e.* form factor scaling), we achieve the dipole approximation to the form factors:

$$\begin{aligned} G_D(Q^2) &= \frac{1}{(1+Q^2 r_0^2)^2} \\ &= G_E^p(Q^2) \\ &= G_M^p(Q^2)/\mu_p \end{aligned} \tag{5.4}$$

Previous measurements of e-p elastic scattering have indicated a best fit value of $r_0^2 = (0.24\text{ fm})^2 = 1/0.71\ (\text{GeV/c})^{-2}$, indicating an rms radius of $\sqrt{\langle r^2 \rangle} \approx 0.81$ fm. Measurements of G_E^p and G_M^p agree with the dipole approximation, as well as form factor scaling, to 10% for $Q^2 < 1.5\ (\text{GeV/c})^2$.

5.2.2 Vector Meson Dominance Models

Vector meson dominance models [55,56] approximate the e-p scattering vertex by assuming the primary mode of coupling between the virtual photon and the proton is through a vector meson. The form factor for the γ-p coupling through a vector meson can be written as the meson propagator term times a VNN coupling term:

$$(Q^2) \sim \frac{1}{Q^2 + M_V^2} F_{VNN}(Q^2) \tag{5.5}$$

where M_V is the vector meson mass, and F_{VNN} is the meson-nucleon form factor. This coupling is shown in Figure 5.6.

The VMD model contains both iso-vector and iso-scalar meson components to the photon, thus there are iso-vector and iso-scalar components to the form factors. These can be written in terms of the Pauli and Dirac form factors, F_1 and F_2, and are related to the nucleon form factors by:

$$\begin{aligned} F_1^p &= F_1^{IS} + F_1^{IV} \\ F_2^p &= F_2^{IS} + F_2^{IV} \\ F_1^n &= F_1^{IS} - F_1^{IV} \\ F_2^n &= F_2^{IS} - F_2^{IV} \end{aligned} \tag{5.6}$$

Different models incorporate different numbers of vector mesons in the calculations, and some include a bare photon coupling in addition. Two typical models will be discussed here.

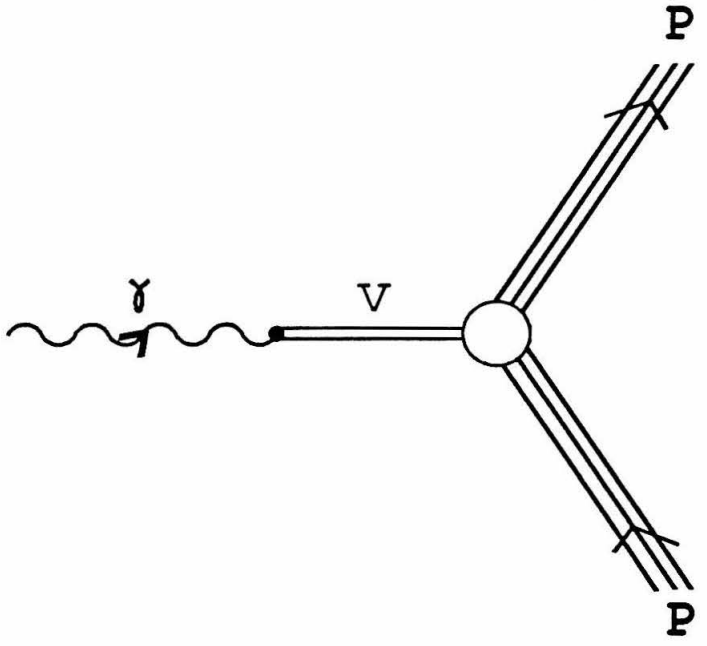

Figure 5.6 – Vector meson dominance picture of the coupling of a photon to a proton.

G. Höhler, et. al. [28]

The VMD model developed by G. Höhler, *et al.*, incorporates terms involving the exchange of ρ and ω mesons, plus higher terms that are associated with the ϕ, ω' and ρ' mesons. Contributions from the ρ were determined from π-N scattering data and 2-π final state data, as well as $F_\pi(Q^2)$. Masses and coupling strengths of the higher mesons were free parameters that were fit to the previous proton form factor data. Expressions for the form factors were thus:

$$F_1^p(Q^2) = F_{1\rho}^p + \frac{a_1(\omega)}{M_\omega^2 + Q^2} + \sum_V \frac{a_1(V)}{M_1^2(V) + Q^2}$$
$$\kappa_P F_2^p(Q^2) = F_{2\rho}^p + \frac{a_2(\omega)}{M_\omega^2 + Q^2} + \sum_V \frac{a_2(V)}{M_2^2(V) + Q^2} \qquad (5.7)$$

$$F_{1\rho}^{p} = \left(\frac{1}{2}\right)\frac{0.955 + 0.090(1 + Q^2/0.355)^{-2}}{1 + Q^2/0.536}$$
$$F_{2\rho}^{p} = \left(\frac{1}{2}\right)\frac{5.335 + 0.962(1 + Q^2/0.268)^{-1}}{1 + Q^2/0.603} \qquad (5.8)$$

where V refers to the heavier meson states. The value used for the mass of the ω was fixed at 0.7826 GeV. Many different fits were done to various form factor data sets, and the parameters presented here (from fit 5.3) were the best fit to the proton data set alone:

$$a_1(\omega) = 0.67 \qquad a_2(\omega) = 0.04$$
$$a_1(V_1) = -0.39 \qquad a_2(V_1) = -1.88$$
$$a_1(V_2) = -0.54 \qquad a_2(V_2) = 0.24$$
$$M_1(V_1) = 0.96 \text{ GeV} \qquad M_2(V_1) = 1.14 \text{ GeV}$$
$$M_1(V_2) = 1.66 \text{ GeV} \qquad M_2(V_2) = 3.19 \text{ GeV}$$

Iachello, Jackson, and Lande [57]

Another VMD model, developed by Iachello, Jackson, and Lande (IJL), incorporated terms from ρ, ω, and ϕ exchange, in addition to a contribution from a bare photon coupling. An intrinsic proton form factor, $g(Q^2)$, was also included. The equations used for F_1 and F_2 were:

$$F_1^{IS} = \frac{1}{2}g(Q^2)\left[(1 - \beta_\omega - \beta_\phi) + \beta_\omega\frac{M_\omega^2}{M_\omega^2 + Q^2} + \beta_\phi\frac{M_\phi^2}{M_\phi^2 + Q^2}\right]$$
$$F_1^{IV} = \frac{1}{2}g(Q^2)\left[(1 - \beta_\rho) + \beta_\rho\frac{M_\rho^2 + 8\Gamma_\rho M_\pi/\pi}{M_\rho^2 + Q^2 + (4M_\pi^2 + Q^2)\Gamma_\rho\alpha(Q^2)/M_\pi}\right]$$
$$\kappa_s F_2^{IS} = \frac{1}{2}g(Q^2)\left[(-0.12 - \alpha_\phi)\frac{M_\omega^2}{M_\omega^2 + Q^2} + \alpha_\phi\frac{M_\phi^2}{M_\phi^2 + Q^2}\right]$$
$$\kappa_v F_2^{IV} = \frac{1}{2}g(Q^2)\left[3.706\frac{M_\rho^2 + 8\Gamma_\rho M_\pi/\pi}{M_\rho^2 + Q^2 + (4M_\pi^2 + Q^2)\Gamma_\rho\alpha(Q^2)/M_\pi}\right] \qquad (5.9)$$

where an attempt has been made to include the finite width of the ρ meson, Γ_ρ, into the formalism using the techniques of Frazer and Fulco [58]. The widths of the other mesons are small and were ignored. The function $\alpha(Q^2)$ was defined:

$$\alpha(Q^2) = \frac{2}{\pi}\left[\frac{Q^2 + 4M_\pi^2}{Q^2}\right]^{1/2} \ln\left[\frac{(Q^2 + 4M_\pi^2)^{1/2} + (Q^2)^{1/2}}{2M_\pi}\right] \tag{5.10}$$

Different forms of $g(Q^2)$ were attempted in the fit, but only the one which gave the best fit to the form factor data (and the proper asymptotic behavior within the QCD formalism) will be considered here. This form was a dipole:

$$g(Q^2) = \frac{1}{(1 + \gamma Q^2)^2} \tag{5.11}$$

The parameters were fit to elastic proton and neutron form factor data. The fit had fixed values of $M_\rho = 0.765$ GeV, $M_\omega = 0.784$ GeV, and $M_\phi = 1.019$ GeV. When the effect of the ρ-meson width was ignored (Γ_ρ=0), the χ^2/dof was large ($\sim$ 2-3). However, with $\Gamma_\rho = 112$ MeV, the χ^2 was much smaller ($\sim$ 1). The following parameters were extracted:

$$\gamma = 0.25 \text{ (GeV/c)}^{-2}$$

$$\beta_\rho = 0.672$$

$$\beta_\omega = 1.102$$

$$\beta_\phi = 0.112$$

$$\alpha_\phi = -0.052$$

with χ^2/dof=0.924. Note that the value of γ for the intrinsic nucleon form factor was much smaller than the value of r_0^2 extracted for the dipole form factor ($r_0^2 = 1.41$ (GeV/c)$^{-2}$).

5.2.3 Dimensional Scaling

Dimensional scaling predicts [59] that in the absence of an internal mass scale the exclusive cross section of a process $AB \rightarrow CD$ can be expressed by:

$$\lim_{t\to\infty} \frac{d\sigma}{dt}(AB \rightarrow CD) \sim s^{-n+2} f(t/s) \tag{5.12}$$

where n is the total number of lepton, photon, or elementary quark fields carrying a finite fraction of the momentum in the particles A, B, C, and D; s is the center of mass energy squared, $t = -Q^2$, and f is a function of the ratio t/s. For $ep \rightarrow ep$ scattering, $n = 8$ (initial state $(1e,\ 3q)$ + final state $(1e,\ 3q) = 8$ fields). Thus the prediction of dimensional scaling for ep elastic scattering is, in the limit of large t and fixed t/s:

$$\begin{aligned} \frac{d\sigma}{dt}(ep \rightarrow ep) &\sim s^{-6} \\ &\sim t^{-6} \\ &\sim \frac{1}{Q^{12}} \end{aligned} \tag{5.13}$$

Fixed t/s corresponds to a fixed center-of-mass scattering angle. This can alternatively be expressed in the limit of high Q^2 in the fixed target frame by $E_0 \sim Q^2$, $E' \sim Q^2$, and $\sin^2(\theta/2) \sim 1/Q^2$.

The cross section $d\sigma/dt$ is related to $d\sigma/d\Omega$, and thus to F_1^p which dominates at large Q^2, by:

$$\begin{aligned} \frac{d\sigma}{dt} &= \frac{\pi}{E_0 E'} \frac{d\sigma}{d\Omega} \\ &\sim \frac{1}{Q^4} \frac{E'^2 \cos^2(\theta/2)}{Q^4} Q^2 F_1^2 \tan^2(\theta/2) \frac{E'}{E_0} \\ &\sim \frac{1}{Q^4} F_1^2 \end{aligned} \tag{5.14}$$

therefore:

$$F_1^2 \sim \frac{1}{Q^8} \tag{5.15}$$

Thus dimensional scaling predicts that $F_1^p \sim 1/Q^4$ in the limit of high Q^2. Since F_2^p is related to the helicity non-conserving part of the scattering amplitude, it is suppressed in the limit of high Q^2 by a factor of $\sim m_q^2/Q^2$ relative to F_1^p where m_q is the quark mass scale. Dimensional scaling thus predicts that $F_2^p \sim 1/Q^6$ in the limit of high Q^2. This can be stated alternatively as $Q^4 F_1^p \sim$ constant and $Q^2(F_2^p/F_1^p) \sim$ constant. These predictions are similar to those of Perturbative QCD (PQCD) [60], neglecting factors of $\alpha_s(Q^2)$.

The question as to what Q^2 is a "high" Q^2 is a controversial one within the literature. More discussion of this question will appear in the following two subsections. Data from *e-p* elastic scattering [51] seem to indicate the onset of scaling in the range of 5-10 $(\mathrm{GeV/c})^2$. Data [61] on pion cross sections exhibit scaling behavior for $Q^2 > 1$ $(\mathrm{GeV/c})^2$, while neutron data [62] exhibits the behavior above 3 $(\mathrm{GeV/c})^2$. Recent data [63] on the photodisintegration of the deuteron also indicate scaling above 1 $(\mathrm{GeV/c})^2$.

5.2.4 Perturbative QCD

M. Gari and W. Krümpelmann [60] have attempted to combine the low Q^2 phenomenology of VMD with the high Q^2 predictions of PQCD. In this model the intrinsic proton vertex form factors, F_1^p and F_2^p, follow a monopole type Q^2 dependence at low Q^2, where meson physics dominates. But at high Q^2 they have a dependence of $F_1^p \sim 1/Q^4$ and $F_2^p \sim 1/Q^6$ $\Big(\text{modified by } \log(Q^2/\Lambda^2)\Big)$, as predicted by PQCD. These form factors are also modified by contributions from vector meson propagator terms. For this model only the ρ and ω mesons were included, and no attempt was made to

include the ρ resonance width. This leads to a parameterization of the iso-scaler and iso-vector form factors of:

$$\begin{aligned}
F_1^{IV} &= \left(\frac{M_\rho^2}{M_\rho^2+Q^2}\frac{g_\rho}{f_\rho}+1-\frac{g_\rho}{f_\rho}\right)F_1^{QCD} \\
F_1^{IS} &= \left(\frac{M_\omega^2}{M_\omega^2+Q^2}\frac{g_\omega}{f_\omega}+1-\frac{g_\omega}{f_\omega}\right)F_1^{QCD} \\
\kappa_v F_2^{IV} &= \left(\frac{M_\rho^2}{M_\rho^2+Q^2}\frac{g_\rho}{f_\rho}\kappa_\rho+\kappa_v-\frac{g_\rho}{f_\rho}\kappa_\rho\right)F_2^{QCD} \\
\kappa_s F_2^{IS} &= \left(\frac{M_\omega^2}{M_\omega^2+Q^2}\frac{g_\omega}{f_\omega}\kappa_\omega+\kappa_s-\frac{g_\omega}{f_\omega}\kappa_\omega\right)F_2^{QCD}
\end{aligned} \tag{5.16}$$

$$\begin{aligned}
F_1^{QCD} &= \frac{\Lambda_1^2}{\Lambda_1^2+\hat{Q}^2}\frac{\Lambda_2^2}{\Lambda_2^2+\hat{Q}^2} \\
F_2^{QCD} &= \frac{\Lambda_2^2}{\Lambda_2^2+\hat{Q}^2}F_1^{QCD}
\end{aligned} \tag{5.17}$$

$$\hat{Q}^2 = Q^2\frac{\ln\left(\frac{\Lambda_2^2+Q^2}{\Lambda_{QCD}^2}\right)}{\ln\left(\frac{\Lambda_2^2}{\Lambda_{QCD}^2}\right)} \tag{5.18}$$

where $\kappa_v = \kappa_p - \kappa_n$ and $\kappa_s = \kappa_p + \kappa_n$, and κ_p and κ_n are the anomalous contributions to the proton and neutron magnetic moments, respectively. Λ_1 is the scale of the proton wave function (~ 0.8 GeV) and Λ_2 is the scale below which the meson dynamics dominate and above which the quark dynamics dominate. The parameter $\hat{Q}^2$ contains the logarithmic dependence of the strong coupling constant.

This model was fit to proton and neutron form factors extracted from the measured electron scattering cross sections using the experimental values $M_\rho = 0.776$ GeV and $M_\omega = 0.784$ GeV. The following values of the parameters were extracted:

$$\Lambda_1 = 0.795 \text{ GeV} \quad \Lambda_2 = 2.27 \text{ GeV} \quad \Lambda_{QCD} = 0.29 \text{ GeV}$$

$$\frac{g_\rho}{f_\rho} = 0.377 \qquad \kappa_\rho = 6.62$$

$$\frac{g_\omega}{f_\omega} = 0.411 \qquad \kappa_\omega = 0.163$$

with a χ^2/dof of 0.43. These parameters are in good agreement with other experiments ($\kappa_\rho = 6.1 \pm 0.6$ [64,65] and $\kappa_\omega = 0.14 \pm 0.2$ [66] from pion-nucleus scattering) and $SU(3)_F$ predictions ($g_\rho/g_\omega = \sin\Theta/\sqrt{3}$, $g_\Phi = 0$ for Θ near ideal mixing angle [60] and $\Lambda_1 \sim 0.8$ GeV from a strong interaction coupling scheme [67,68]). Perturbative QCD effects begin to dominate the form factors at a value of $Q^2 = \Lambda_2^2 = 5.15$ (GeV/c)^2.

5.2.5 QCD Sum Rules

A model proposed by Radyushkin [69] attempts to reproduce the form factor scaling behavior that has been measured in various experiments by using only the soft components of the proton wave function and without invoking the large Q^2 assumptions of scale invariance and lowest order PQCD. In this model *e-p* scattering is decomposed into the components shown in Figure 5.7. The higher order diagrams are suppressed by a factor of $\alpha_s(Q^2)/\pi$ for each gluon exchange that occurs. Thus diagram (a) is naively expected to be the dominant contribution to the form factors. At large Q^2, however, diagrams (a) and (b) are suppressed due to the momentum imbalance of the quarks and the corresponding small overlap between the intermediate quark wave function and the final proton wave function. Diagram (c), which allows the quarks to achieve similar momenta will then dominate, and is expected to fall like $1/Q^4$ due to the dimensional scaling laws [59] discussed before. There should exist an energy scale, Q_0^2, where diagram (a) is dominant for $Q^2 < Q_0^2$, while (c) is dominant for $Q^2 > Q_0^2$. Radyushkin calculates the contribution from diagram (a) (to be discussed below), and finds that it behaves like $1/Q^6$ in the asymptotic limit. He therefore concludes that the scale of Q_0^2 might be of the order $[1/(\alpha_s(M_p)/\pi)^2][O(1\ (\mathrm{GeV/c})^2)] \sim 100$ (GeV/c)^2. This is well above the range of presently available data, which have been used as an indication of the validity of the scaling model.

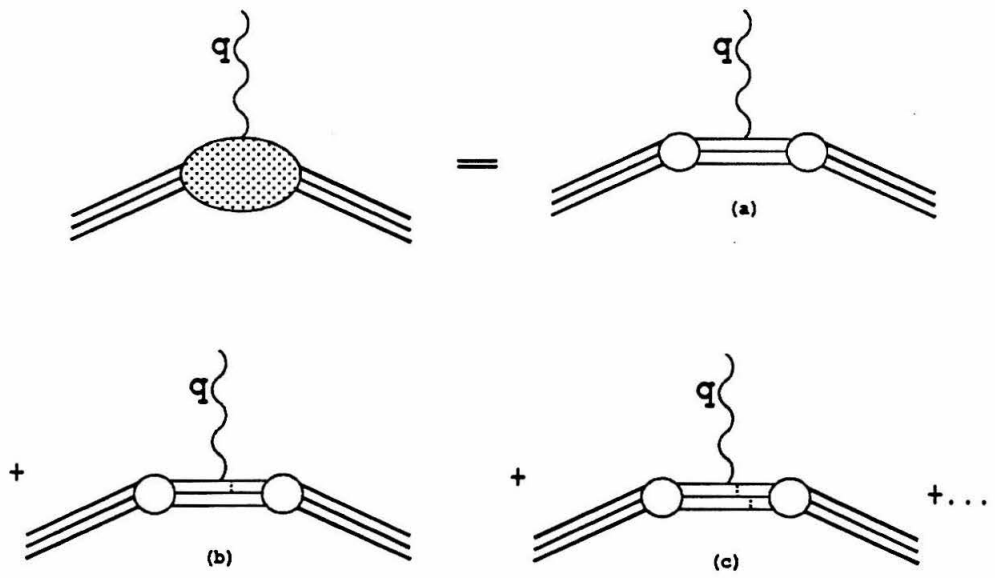

Figure 5.7 – The Feynman diagrams for factorization (in α_s) of *e-p* elastic scattering.

In this model the coupling of the electromagnetic current to a current with the same quantum numbers as the proton is calculated (Figure 5.7(a)). The hadronic spectral density, $\rho(s_1, s_2, Q^2)$, where s_1 and s_2 are the mass squared of the incoming and outgoing hadronic current, respectively, was determined. At large values of s_1 and s_2 where the hadronic resonances are broad the hadronic density should correspond to the perturbative free quark density. At small values of s_1 and s_2 non-perturbative effects will cause ρ to become a δ function located at the mass of the proton ($\rho(s_1, s_2, Q^2) \sim \delta(s_1 - M_p^2)\delta(s_2 - M_p^2)$). Quark-hadron duality suggests, however, that these non-perturbative effects only cause the strength to be concentrated within a local range in s_1 and s_2 and do not effect the overall magnitude. Thus the

contribution of the proton, the lowest mass hadron with the proper quantum numbers, can be related to an integral of the perturbative contribution, ρ^{pert}, over a range of $0 \leq s_1 \leq s_0$ and $0 \leq s_2 \leq s_0$, where s_0 is the duality constant. The value of s_0 was fixed [70,71] at $s_0 = 2.3$ (GeV/c)^2. The form factors were computed to be:

$$\begin{aligned} F_1^p &= \frac{1}{(2\pi)^4 \lambda_N^2} \int_0^{s_0} ds_1 \int_0^{s_0} ds_2 \; Q^2 (1 - \frac{\sigma}{z})^2 \\ &\times \{ \frac{2e_u - e_d}{16} \frac{Q^2}{z} (1 + \frac{\sigma}{z})^2 + \frac{e_u + e_d}{12} (2 + \frac{\sigma}{z}) \} \\ G_M^p &= \frac{e_u}{(2\pi)^4 \lambda_N^2} \int_0^{s_0} ds_1 \int_0^{s_0} ds_2 \; \frac{Q^2}{4} (1 - \frac{\sigma}{z})^2 (2 + \frac{\sigma}{z}) \end{aligned} \tag{5.19}$$

where $\sigma = s_1 + s_2 + Q^2$, $z = \sqrt{\sigma^2 - 4 s_1 s_2}$, $e_u = 2/3$, $e_d = -1/3$. λ_N is related to s_0 by $(2\pi)^4 \lambda_N^2 = s_0^3/12$. The results of these calculations agree with the data [51] on G_M^p fairly well up to $Q^2 \sim 20$ (GeV/c)^2 (see Figure 5.8). It is not until $Q^2 \sim 30$ (GeV/c)^2 that the full asymptotic $1/Q^6$ falloff begins to occur. In this limit the magnetic form factor behaves like $G_M^p \sim \frac{4 e_u s_0^3}{Q^6}$. It is important to note that, although the normalization $G_E^p(0)$=1 is fixed in this theory (through the quark charges e_u and e_d), the normalization of $G_M^p(0)$=μ_p is not required, since μ_p is not included in any of the equations.

5.2.6 Diquark Models

The diquark model of the nucleon was motivated, in part, by recent polarized elastic *p-p* experiments [72] performed at Brookhaven that indicated an unexpectedly large number of helicity non-conserving events in elastic proton-proton scattering. Non-perturbative effects are one way to describe such helicity flips. The diquark model of Anselmino, Kroll, and Pire (AKP) [73] is an attempt to include such higher twist effects.

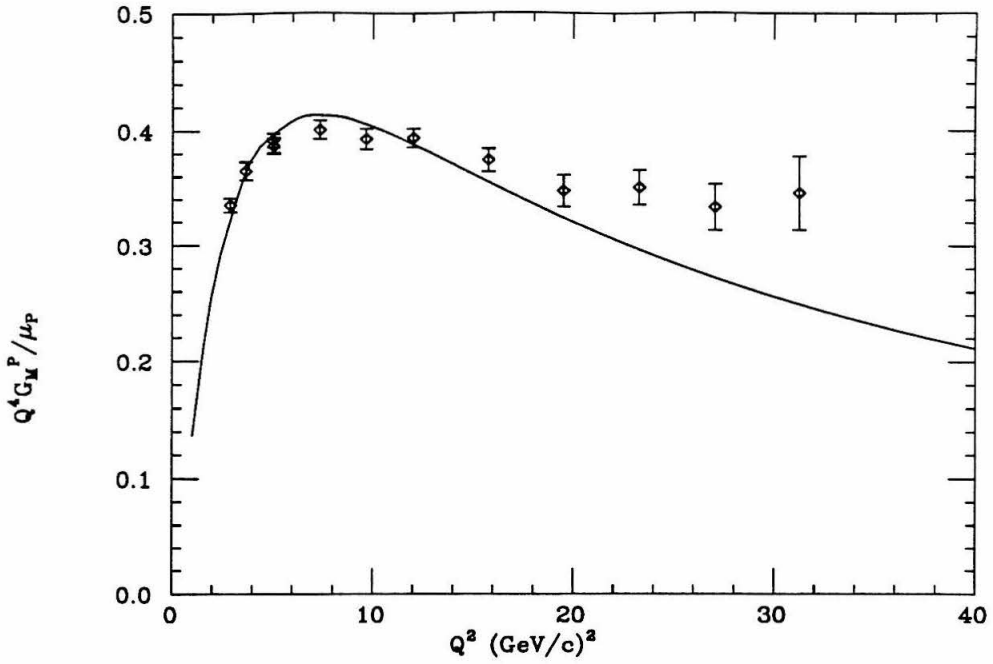

Figure 5.8 – A comparison between data [51] on G_M^p and the model of Radyushkin [69] using quark-hadron duality and QCD sum rules.

In this model it is presumed that of the three quarks within the nucleon, two of them form a tightly coupled diquark state ($r \sim$ 0.1-0.3 fm), while the third quark is more loosely bound (see Figure 5.9). These diquarks could exist in either a scaler or (axial-)vector state. The proton form factors can be derived in this model, treating the diquark as an elementary particle, and are given by:

$$G_M^p(Q^2) = \frac{8\pi C_F}{3Q^2}\Big\{\int dx\ dy\ \phi_S^*(y)\frac{\alpha_s(\hat{Q}^2)F_S(\hat{Q}^2)}{(1-x)(1-y)}\phi_S(x) - \frac{Q^2}{8m^2}F_V(Q^2)\int dx\ dy\ \phi_V^*(y) \cdot \frac{\alpha_S(\tilde{Q}^2)(1-x)(1-y)F_V(\tilde{Q}^2)}{xy}\phi_V(x)\Big\}$$

$$F_2^p(Q^2) = -\frac{2\pi C_F}{Q^2\kappa_p}F_V(Q^2)\int dx\ dy\ \phi_V^*(y)$$

$$\cdot \frac{\alpha_S(\tilde{Q}^2)F_V(\tilde{Q}^2)}{xy}\phi_V(x) \tag{5.20}$$

where $\hat{Q}^2 = (1-x)(1-y)Q^2$ and $\tilde{Q}^2 = xyQ^2$, m is the mass of the vector diquark (assumed to be 580 MeV), and $C_F = 4/3$ is the color factor. F_S and F_V are the diquark form factors and are given by:

$$F_S(Q^2) = \frac{\alpha_S(Q^2)Q_0^2}{Q_0^2+Q^2}$$
$$F_V(Q^2) = \frac{\alpha_S(Q^2)Q_1^2}{Q_1^2+Q^2} \tag{5.21}$$

where Q_0^2 and Q_1^2 are related to the size of the scaler and vector diquarks (similar to the dipole form factor for the proton). ϕ_V and ϕ_S are the longitudinal momentum wave functions of the diquarks. Under exact $SU(6)$ symmetry they would be related by $\phi_V = \phi_S$.

The asymptotic behavior of the form factors, $G_M^p \sim 1/Q^4$ and $F_2^p \sim 1/Q^6$, is also predicted by this model. AKP found good agreement with the data [51] on G_M^p for $10 \leq Q^2 \leq 30$ (GeV/c)^2 with $Q_0^2 = Q_1^2 \approx 3.2$ GeV^2 and $\phi_s = \phi_v = \delta(x-0.4)$ when the form factors were normalized to the data at $Q^2 = 15$ (GeV/c)^2. An identical calculation was performed for this paper, and a similar agreement with the data was found when a multiplicative normalization constant of ≈ 0.16 was applied. However, G_E^p was found to be approximately related to G_M^p by:

$$G_E^p(Q^2) \approx 2 \times G_M^p(Q^2) \tag{5.22}$$

for $1 \leq Q^2 \leq 100$ (GeV/c)^2. The large value of G_E^p relative to G_M^p occurs because of the negative value of F_2^p. At *very* large Q^2 ($\sim 10^7$ (GeV/c)^2), the asymptotic limit stated by AKP of $G_E^p \approx G_M^p$ is achieved. This is far beyond the valid range of this model, and it occurs because the contribution of F_2^p goes to zero due to the extra power of $\alpha_s(Q^2)$ in the vector diquark contributions relative to the scaler diquarks, but this falloff occurs only logarithmically.

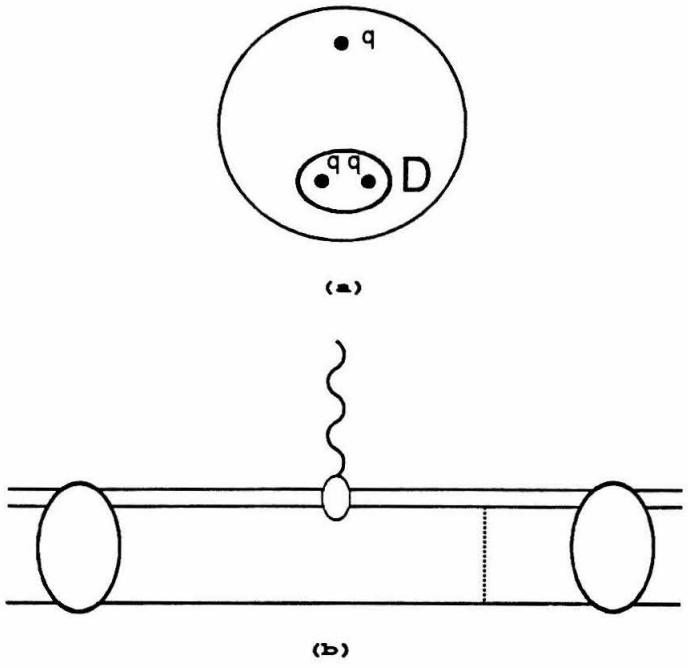

Figure 5.9 – (a) Schematic picture of a proton in the diquark model. (b) Feynman diagram for scattering from a diquark within the proton.

5.2.7 Presentation of the Predictions

The dipole form factor, $G_D(Q^2)$, is plotted in Figure 5.10 versus Q^2. This parameterization describes the dominant Q^2 behavior of the form factors. Other predictions for the form factors will be presented relative to the dipole form factor. The sharp falloff with Q^2 is clearly seen, leading to an even sharper falloff in the cross section at large Q^2 since the cross section depends on the square of the form factor.

Various parameterizations for G_E^p are shown in Figure 5.11. The data from various experiments are plotted for comparison. The models of Gari [60], Höhler [28], and IJL [57] clearly fall below our data. However, since these theories had free parameters that were fit to previous data, which was dominated by Bartel's 1973

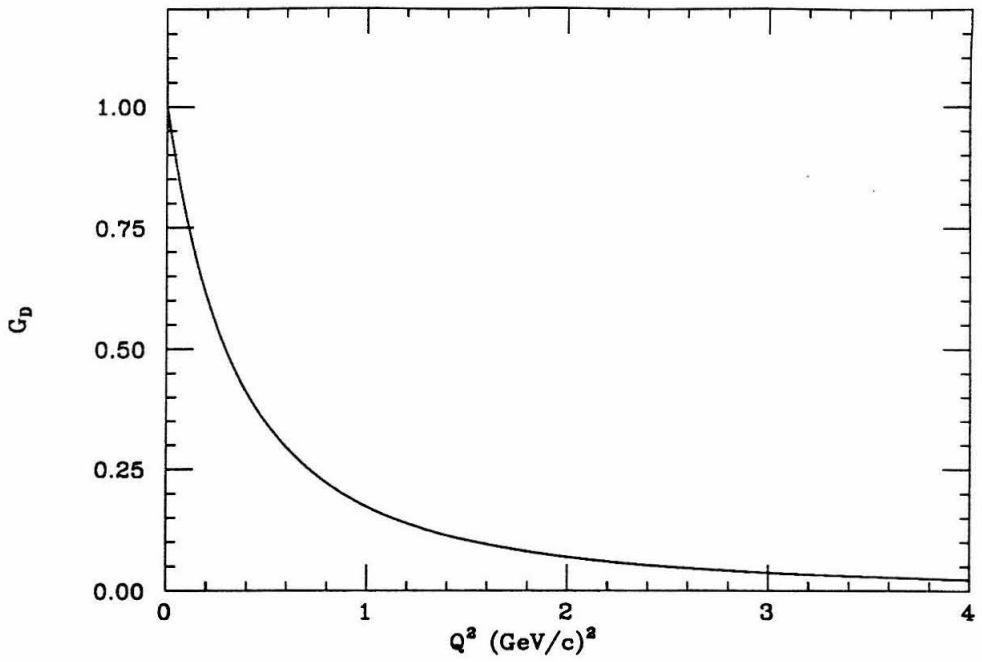

Figure 5.10 – The dipole form factor, $G_D(Q^2)$, versus Q^2.

data [3], slight adjustments could be made to these parameters to account for the new data. Radyushkin [69] shows good agreement with our data. The diquark theory of AKP [73] has not been plotted because it is off scale; in the range of $1 \leq Q^2 \leq 3$ (GeV/c)^2, this model predicts $G_E^p/G_D \sim$ 4-5, and the value stays above 4 for $Q^2 < 8$ (GeV/c)^2 (the world fit limits $G_E^p/G_D < 3.2$ for $Q^2 < 10$ (GeV/c)^2 at the 95% C.L.).

Predictions for $G_M^p/G_D/\mu_p$ are shown in Figure 5.12. The curves of Gari, Hohler, and IJL go above the data of this experiment for reasons that are strongly correlated with the discrepancies in the G_E^p values. Radyushkin's theory disagrees for $Q^2 \leq 2.5$, but is clearly getting results that are nonphysical in this region (*i.e.* the required normalization of $G_M^p(0) = \mu_p$ is violated). However, the value of $G_M^p/G_D/\mu_p$ reaches a minimum of ≈ 0.65 at $Q^2 \approx 0.16$, and rises back up to ≈ 0.94 at $Q^2 = 0$.

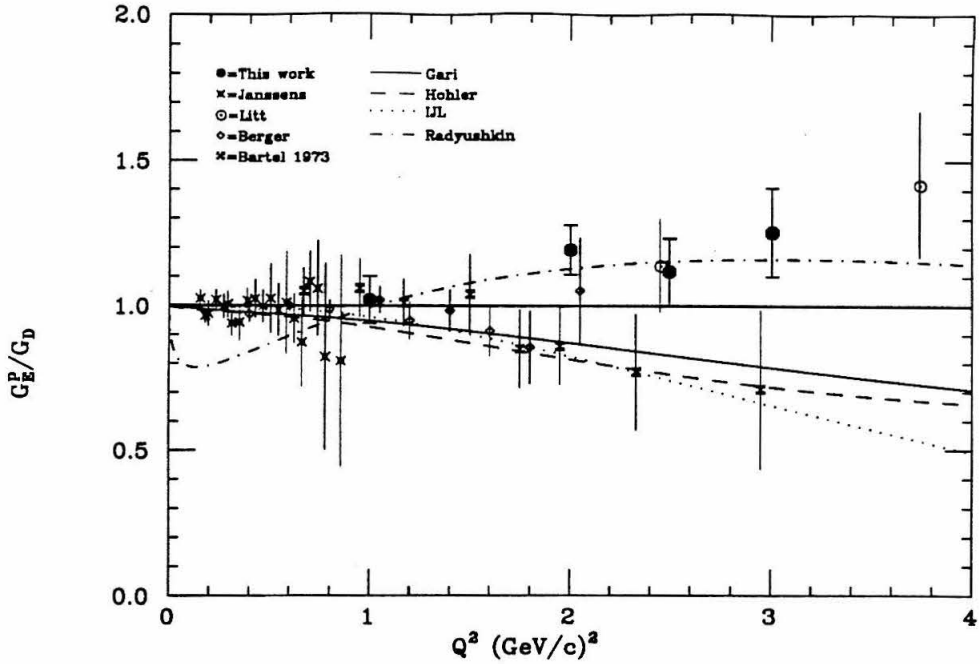

Figure 5.11 – The models for G_E^p. The lines correspond to: solid=Gari, dash=Hohler, dot=IJL, dotdash=Radyushkin.

Radyushkin attempted to eliminate some of these low-Q^2 problems by assuming the phenomenological form factor scaling relationship (G_E^p=G_M^p/μ_p) and extracting both form factors from the F_1^p calculation, which is expected to be more accurate at low Q^2. This does tend to reduce the disagreement in the range of $Q^2 \sim$ 2-3 (GeV/c)^2 ($G_M^p/G_D/\mu_P = 1.01$ at $Q^2 = 2$ (GeV/c)^2). The model of AKP is not plotted, but falls from a value of 1.15 at $Q^2 \approx 1$ to 0.85 at $Q^2 \approx 3$ (GeV/c)^2, and is clearly ruled out by the data in the range of $Q^2 \leq 3$ (GeV/c)^2.

In figure 5.13 the values of $Q^2(F_2^p/F_1^p)$ are plotted. Our data clearly flattens out much more quickly than most of the theories; only Radyushkin shows a similar behavior. The best fit value to the slope of the data of this experiment for $Q^2 \geq 2$ (GeV/c)^2 is 0.08 ± 0.11 (GeV/c)$^{-2}$, the value for Gari in this region is 0.19, while

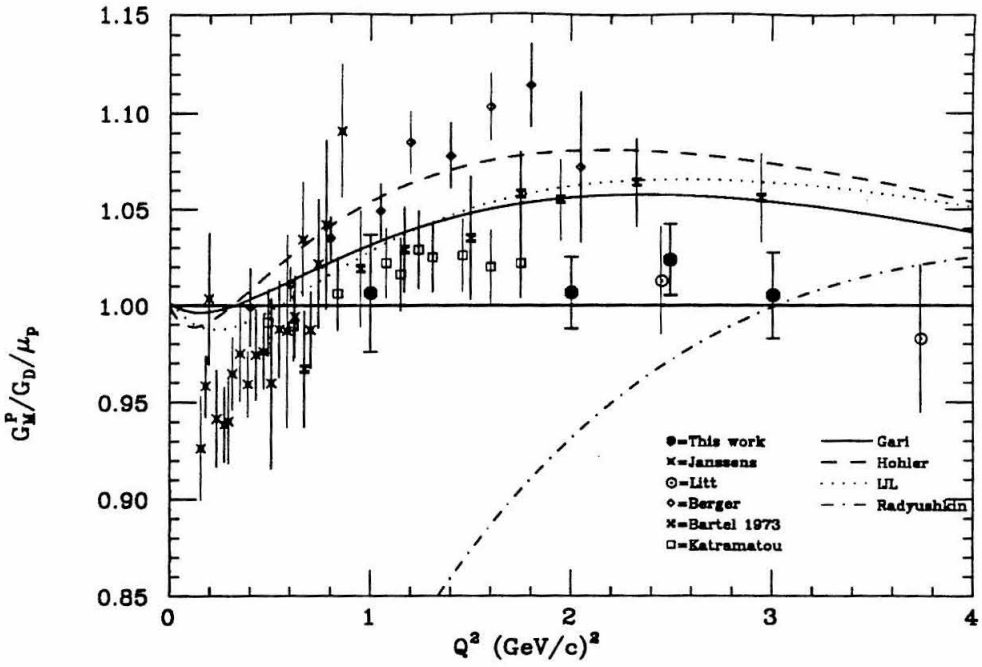

Figure 5.12 – The models for G_M^p. The legend is the same as Figure 5.11.

Radyushkin predicts 0.14. The AKP model is not plotted, but predicts $Q^2(F_2^p/F_1^p)\sim -0.4$ in this Q^2 regime due to the fact that F_2^p is negative in this model.

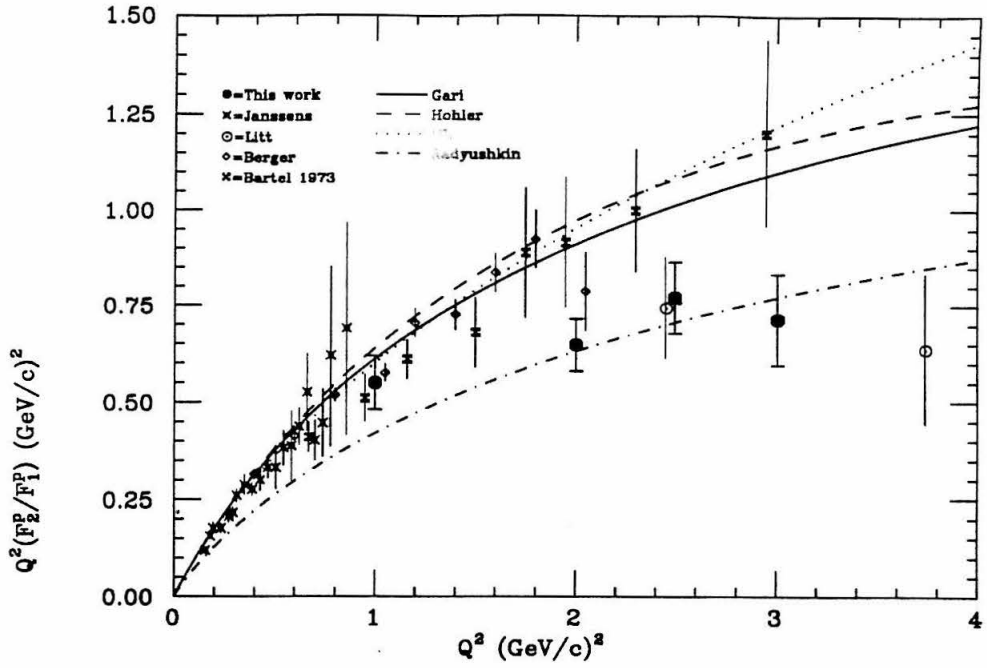

Figure 5.13 – The models for $Q^2(F_2^p/F_1^p)$. The legend is the same as the previous figures.

Chapter 6
Conclusions

We have extracted the proton form factors from *e-p* elastic scattering for $1 \leq Q^2 \leq 3$ (GeV/c)^2 using a Rosenbluth separation technique covering an angular range of cross section measurements of $11.5° \leq \theta \leq 48°$. Statistical uncertainties were $\leq 1\%$ in the cross sections, 7-11% in G_E^p and 1.5-2.5% in G_M^p. The systematic uncertainties were smaller than the statistical uncertainties; most previous form factor extractions

have been dominated by systematic uncertainties. The absolute normalization uncertainty for the cross sections was 1.6%. The total uncertainty in G_E^p was reduced by $\sim$ a factor of two over previous measurements in this Q^2 regime. Improvements could be made, however, with a better theoretical understanding of the radiative corrections used in the analysis; particularly the corrections arising from two-photon exchange and $O(\alpha^4)$ contributions.

A comparison between our data and previous measurements indicate marginal agreement with the previous DESY data and good agreement with previous SLAC data. However, our data for G_E^p rises above the dipole approximation, while the DESY data tended to fall 1-σ below the dipole. Most parameterizations of the data have also fallen below the dipole, but this has been ruled out, both by our data and the previous SLAC data. Our measurements are also in marginally good agreement with the *ansatz* of form factor scaling ($G_E^p \approx G_M^p/\mu_p$). The measurements of $Q^2(F_2^p/F_1^p)$ are lower in magnitude and demonstrate less Q^2 dependence then the previous DESY and Bonn measurements and most parameterizations, but are in good agreement with the predictions of dimensional scaling. They are also in good agreement with the predictions by Radyushkin based on QCD sum rules. The results clearly rule out the diquark model in this range.

A global fit to the data at $Q^2 > 1$ (GeV/c)^2 shows a good consistency between the different data sets within the normalization errors. The extracted values of G_E^p have error bars reduced by a factor of ~ 3 over previous measurements. This data once again rules out the possibility of any significant decrease of G_E^p/G_D below 1 for $Q^2 < 4$ (GeV/c)^2 and generally indicates an increase in G_E^p relative to the dipole with increasing Q^2. The results are in good agreement with the QCD sum rule prediction of Radyushkin for G_E^p. The global fit also limits $G_E^p/G_D < 3.2$ for $Q^2 < 10$ (GeV/c)^2

at the 95% C.L. This clearly rules out the diquark predictions for this Q^2 range and tends to support the *ansatz* of form factor scaling which has been frequently used by other experiments to extract G_M^p from single angle cross section measurements.

The extraction of the proton elastic form factors at relatively large Q^2 with substantially reduced systematic uncertainties has proven to be possible. Measurement of the form factors at larger Q^2 (> 5 (GeV/c)^2) would be an important test of the predictions of dimensional scaling and would enhance our knowledge of the proton substructure and the strong force. A dedicated experiment with greater amounts of beam time than was possible in this experiment should be able to perform such measurements. More precise data at larger values of θ would also be important in order to reduce the statistical and systematic uncertainties involved in the Rosenbluth separation. Such an experiment has been approved at the ESA at SLAC, and should be taking data shortly. Improved calculations of the radiative corrections are also necessary if better measurements of the form factors are to prove possible. Two photon exchange terms, which require an understanding of the contributions arising when the proton is off mass-shell in the intermediate state, need to be estimated. Explicit calculation of the $O(\alpha^4)$ terms, rather than the relatively simple estimate made by exponentiating the $O(\alpha^3)$ contribution, would prove useful. And a better understanding of the energy dependent effects arising from internal bremsstrahlung, beyond the equivalent radiator approximation used in this work, could also be important, due to the strong ε dependence of these corrections. Systematic uncertainties could be further reduced through better calibration of the incident energy.

Appendix A
Radiative Corrections

A.1 Overview

Elastic scattering does not consist of simply the one-photon exchange process outlined in the introduction. Higher order processes in α_{em} also affect the cross section. These processes can be split into two general categories. *Internal* effects are those that occur as a part of the primary *e-p* scattering vertex, such as vacuum polarization, vertex, or internal bremsstrahlung. *External* effects are those caused by secondary scattering from rest of the material in the target, such as bremsstrahlung or ionization losses. (Figure A.1).

These processes cause the elastic cross section to be changed from the simple δ-function at $E' = E'_{el} = E_0/[1 + 2\frac{E_0}{M_p}\sin^2(\theta/2)]$ (modified by resolution effects and the energy spread of the beam) to an asymmetric peak with an extended elastic tail at lower energies (see Figure A.2). The radiative tail extends down to values of E' where other processes (π-production, Δ-resonance, etc.) also occur. Therefore, the integration of the cross section must be cut off at a value of $E' = E'_{el} - \Delta E$, with the value of ΔE chosen to be small enough to exclude these other background processes, but large enough so that the value of the integral is not sensitive to the exact shape of the energy resolution function of the detectors.

Radiative corrections depend on the details of the target materials and geometry. They also depend in a complicated way on the kinematics of the scattering. Therefore they are included as part of the experimental corrections, so that the measured cross

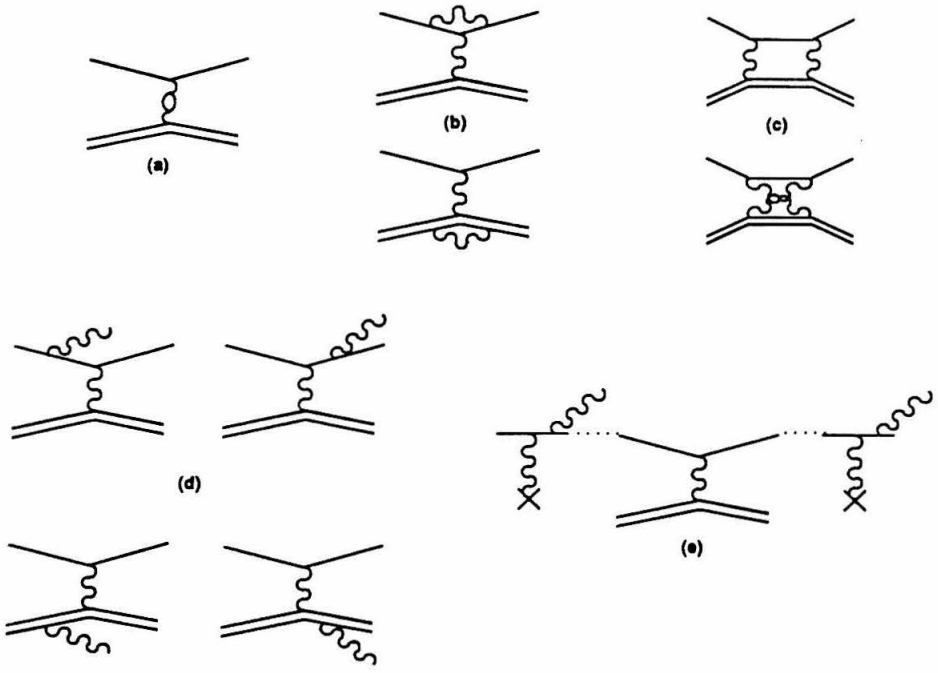

Figure A.1 – The higher Feynman diagrams used in the calculation of the radiative corrections. The internal corrections: (a) vacuum polarization, (b) vertex, (c) two-photon exchange, (d) internal bremsstrahlung. The external corrections: (e) electron bremsstrahlung.

sections correspond to the simple one-photon exchange in the Born approximation presented in the introduction. Exact details of the calculation of the corrections are given below.

A.2 Internal Corrections

The radiative corrections procedure of Mo and Tsai [32] were used to make the internal corrections for this experiment. For a detailed presentation of the calculations involved, see ref [29]. The results are stated here for completeness.

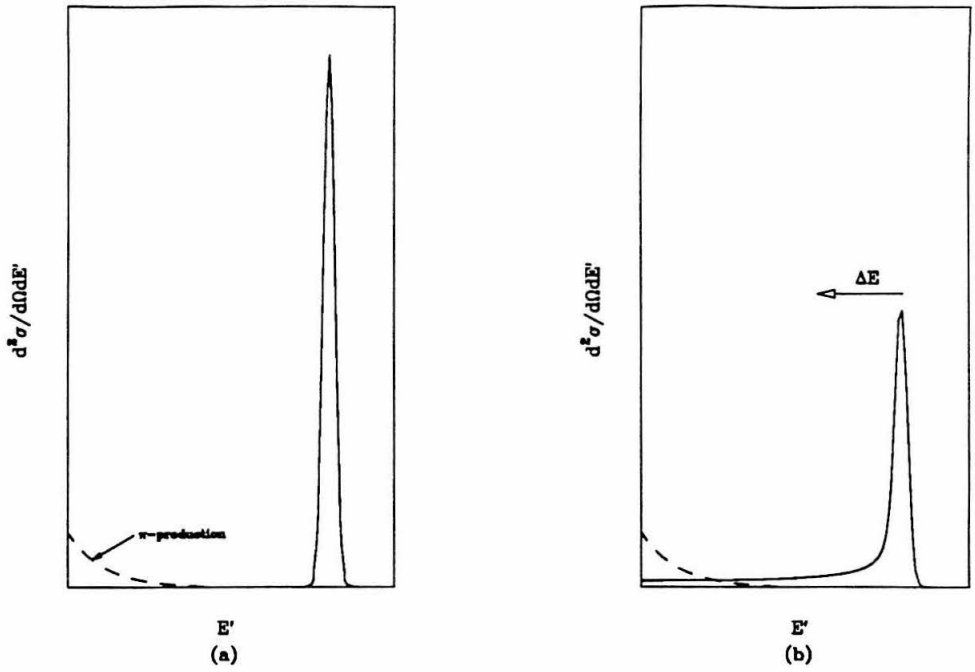

Figure A.2 – (a) Elastic peak in the simple, one-photon exchange approximation (including resolution effects) as a function of E' at fixed E_0 and θ. Other processes (π production, etc.) occur at E' values well below the elastic peak. (b) The elastic peak including higher order radiative effects. The elastic spectrum is integrated from E'_{el} to $E'_{el} - \Delta E$.

The radiative corrections were parameterized by δ_{int}, which related the cross section of $O(\alpha^3_{em})$ to the one-photon exchange cross section by:

$$\frac{d\sigma}{d\Omega}(\alpha^3) = (1 + \delta_{int})\frac{d\sigma}{d\Omega}\Big|_{1\text{-}\gamma} \qquad (A.1)$$

Higher order corrections were approximated by exponentiating δ_{int}:

$$\frac{d\sigma}{d\Omega}_{meas} = e^{\delta_{int}}\frac{d\sigma}{d\Omega}\Big|_{1\text{-}\gamma} \qquad (A.2)$$

Although this approximation for the higher order terms was strictly valid only for the infrared divergent terms, the error caused in the nondivergent terms was estimated [32] to be small ($\leq 0.7\%$ at $Q^2 = 20$ (GeV/c)^2, and smaller at our kinematics).

Contributions from vacuum polarization (Figure A.1(a)) and electron vertex diagrams (Figure A.1(b)) were calculated explicitly. Only the infrared divergent contributions from proton vertex (Figure A.1(b)) and two-photon exchange (Figure A.1(c)) diagrams were calculated; the nondivergent components of these were estimated to be small $< 1\%$ [32,30]. Contributions from these diagrams (neglecting the infrared divergent terms that were not completely cancelled) were:

$$\delta_{int} = \frac{-\alpha}{\pi}\left[\frac{28}{9} - \frac{13}{6}\ln\left(\frac{Q^2}{m_e^2}\right)\right] \tag{A.3}$$

Contributions from the internal bremsstrahlung diagrams (Figure A.1(d)) were somewhat more difficult to calculate. It was assumed that $\Delta E(1 + 2E_0/M_p) \ll E'$ to simplify the calculation. Corrections for this approximation will be discussed later in the section on improvements to the internal corrections. The value of δ_{int}, including the bremsstrahlung diagrams, was:

$$\begin{aligned}
\delta_{int} =& \frac{-\alpha}{\pi}\Big(\frac{28}{9} - \frac{13}{6}\ln(\frac{Q^2}{m_e^2}) + (\ln(\frac{Q^2}{m_e^2}) - 1 + 2Z\ln\eta)(2\ln(\frac{E_0}{\Delta E}) - 3\ln\eta)) \\
&- \Phi(\frac{E' - E_0}{E'}) - Z^2\ln(\frac{E_p}{M_p}) + Z^2\ln(\frac{M_p}{\eta\Delta E})(\frac{1}{\beta_4}\ln(\frac{1+\beta_4}{1-\beta_4}) - 2) \\
&+ \frac{Z^2}{\beta_4}\{\frac{1}{2}\ln(\frac{1+\beta_4}{1-\beta_4})\ln(\frac{E_4 + M_p}{2M_p}) - \Phi[-(\frac{E_4 - M_p}{E_4 + M_p})^{\frac{1}{2}}(\frac{1+\beta_4}{1-\beta_4})^{\frac{1}{2}}]\} \\
&+ Z[\Phi(-\frac{M_p - E'}{E_0}) - \Phi(\frac{M_p(M_p - E')}{2E'E_4 - M_pE_0}) + \Phi(\frac{2E'(M_p - E')}{2E'E_4 - M_pE_0}) \\
&\qquad + \ln|\frac{2E'E_4 - M_pE_0}{E_0(M_p - 2E')}|\ln(\frac{M_p}{2E'})] \\
&- Z[\Phi(-\frac{E_4 - E'}{E'}) - \Phi(\frac{M_p(E_4 - E')}{2E_0E_4 - M_pE'}) + \Phi(\frac{2E_0(E_4 - E')}{2E_0E_4 - M_pE'})
\end{aligned}$$

$$+\ln|\frac{2E_0E_4 - M_pE'}{E'(M_p - 2E_0)}|\ln(\frac{M_p}{2E_0})]$$
$$- Z[\Phi(-\frac{M_p - E_0}{E_0}) - \Phi(\frac{M_p - E_0}{E_0}) + \Phi(\frac{2(M_p - E_0)}{M_p})$$
$$+\ln|\frac{M_p}{2E_0 - M_p}|\ln(\frac{M_p}{2E_0})]$$
$$+ Z[\Phi(-\frac{M_p - E'}{E'}) - \Phi(\frac{M_p - E'}{E'}) + \Phi(\frac{2(M_p - E')}{M_p})$$
$$+\ln|\frac{M_p}{2E' - M_p}|\ln(\frac{M_p}{2E'})] - \Phi(\frac{E_0 - E'}{E_0})$$
$$+ \frac{Z^2}{\beta_4}\{\Phi[(\frac{E_4 - M_p}{E_4 + M_p})^{\frac{1}{2}}(\frac{1 - \beta_4}{1 + \beta_4})^{\frac{1}{2}}] - \Phi[(\frac{E_4 - M_p}{E_4 + M_p})^{\frac{1}{2}}] + \Phi[-(\frac{E_4 - M_p}{E_4 + M_p})^{\frac{1}{2}}]\}\Big) \tag{A.4}$$

with the definitions of E_0 = incident electron energy, E' = final electron energy, m_e = mass of the electron, $\eta = E_0/E'$, M_p = mass of the proton, E_4 = final energy of the proton, β_4 = final velocity of the proton, Z = charge of the target particle (= 1), and ΔE = the E' cutoff of the elastic tail. The infrared divergent terms completely cancelled in this calculation. The Spence functions, Φ, is defined:

$$\Phi(x) \equiv \int_0^x \frac{-\ln|1 - y|}{y} dy \tag{A.5}$$

and was integrated numerically in order to calculate δ_{int}. The typical value of δ_{int} was ~ -0.17.

A.3 External Corrections

Radiative effects that occur external to the principle scattering are caused by bremsstrahlung in the target material and the effects of the Landau tail of the ionization energy loss spectrum. Corrections were made based on the work of Tsai [52].

Bremsstrahlung Spectrum

An electron of energy E will emit bremsstrahlung photons in the field of a nearby nucleus. The probability of losing energy ω ($\omega \lesssim 0.8E, E \gtrsim 0.1$ GeV) after passing through a thickness of t radiation lengths is:

$$P_B(\omega,t)d\omega = \frac{1}{\Gamma(1+bt)}\left[\left(\frac{\omega}{E}\right)^{bt}\right]\frac{bt}{\omega}\left[\phi\left(\frac{\omega}{E}\right)\right]d\omega \qquad (A.6)$$

$$\phi\left(\frac{\omega}{E}\right) = 1 - \left(\frac{\omega}{E}\right) + \frac{3}{4}\left(\frac{\omega}{E}\right)^2 \qquad (A.7)$$

where ϕ is the shape of the bremsstrahlung spectrum and normalized to $\phi(0) = 1$. The parameter $b \approx 4/3$ is given [74] more precisely by:

$$b = \frac{4}{3}\left\{1 + \frac{1}{9}\left[\frac{Z+1}{Z+\eta}\right]\left[\ln(184.15Z^{\frac{-1}{3}})\right]^{-1}\right\} \qquad (A.8)$$

$$\eta = \ln(1194Z^{\frac{-2}{3}})/\ln(184.15Z^{\frac{-1}{3}}) \qquad (A.9)$$

where Z is the charge of the nucleus.

The cross section for an electron of initial energy E_0 to elastically scatter from a proton and have final energy $E' = E'_{el} - \Delta E'$, when the electron is emitting bremsstrahlung photons with t_i and t_f radiation lengths of material before and after scattering, respectively, is:

$$\frac{d^2\sigma(E_0,E')}{d\Omega dE'} = \int_0^{\Delta E_0} d\omega_0 \int_0^{\Delta E'} d\omega' P_B(\omega_0,t_i)P_B(\omega',t_f)\frac{d\sigma(E_0-\omega_0)}{d\Omega}\delta(\omega' + \frac{\omega_0}{R} - \Delta E') \qquad (A.10)$$

where the δ-function fixes the final energy at $E' = E'_{el} - \Delta E'$, and the effect of the proton recoil is included through the parameter R which relates $\Delta E_0 = R\Delta E'$ ($R \approx (\frac{E_0}{E'})^2$). Since $P_B(\omega,t)$ is strongly peaked at $\omega \approx 0$, the double integral can be

approximated by separating it into two single integrals; one near $\omega_0 \approx 0$ and one near $\omega' \approx 0$ (energy peaking approximation). These integrals can be explicitly calculated, leading to the equation:

$$\frac{d^2\sigma(E_0,E')}{d\Omega dE'} = \Big(\frac{R\Delta E'}{E_0}\Big)^{b_i t_i}\Big(\frac{\Delta E'}{E'_{el}}\Big)^{b_f t_f}\frac{1}{\Gamma(1+b_i t_i)}\frac{1}{\Gamma(1+b_f t_f)} \times \Big[\frac{d\sigma(E_0)}{d\Omega}\frac{b_f t_f}{\Delta E'}\phi\Big(\frac{\Delta E'}{E'_{el}}\Big) + \frac{d\sigma(E_0 - R\Delta E')}{d\Omega}\frac{b_i t_i}{\Delta E'}\phi\Big(\frac{R\Delta E'}{E_0}\Big)\Big] \tag{A.11}$$

Straggling and Ionization Loss Spectrum

The energy loss spectrum due to ionization for an electron of energy E passing through material in the ultra-relativistic limit is shown in Figure A.3. This spectrum is described by a Landau distribution [75] which is defined:

$$\Phi_L(\lambda) \equiv \frac{1}{2\pi i}\int_{\sigma-i\infty}^{\sigma+i\infty} e^{\lambda u + u\ln u}du \tag{A.12}$$

where $\sigma > 0$ is a real number. The parameter λ [75,52] is defined:

$$\lambda = \frac{\Delta E - \Delta E_{mp}}{\xi} \tag{A.13}$$

$$\xi = 0.154(Z/A)tx_0 \text{ MeV} \tag{A.14}$$

where Z is the number of protons/nucleus in the material, A is the mass number, and tx_0 is the thickness in g/cm^2. The most probable energy loss is ΔE_{mp} and is defined in Appendix B. At large λ the tail of $\Phi_L(\lambda)$ falls like $\sim 1/\lambda^2$.

The correction for the Landau tail was small for this experiment. Under these conditions a correction to the cross section, CLN, can be calculated to a good approximation by:

$$CLN \equiv 1 - \int_{R\Delta E'}^{\infty} d\omega\ \Phi_L\Big(\frac{\omega}{\xi_i}\Big) - \int_{\Delta E'}^{\infty} d\omega\ \Phi_L\Big(\frac{\omega}{\xi_f}\Big) \tag{A.15}$$

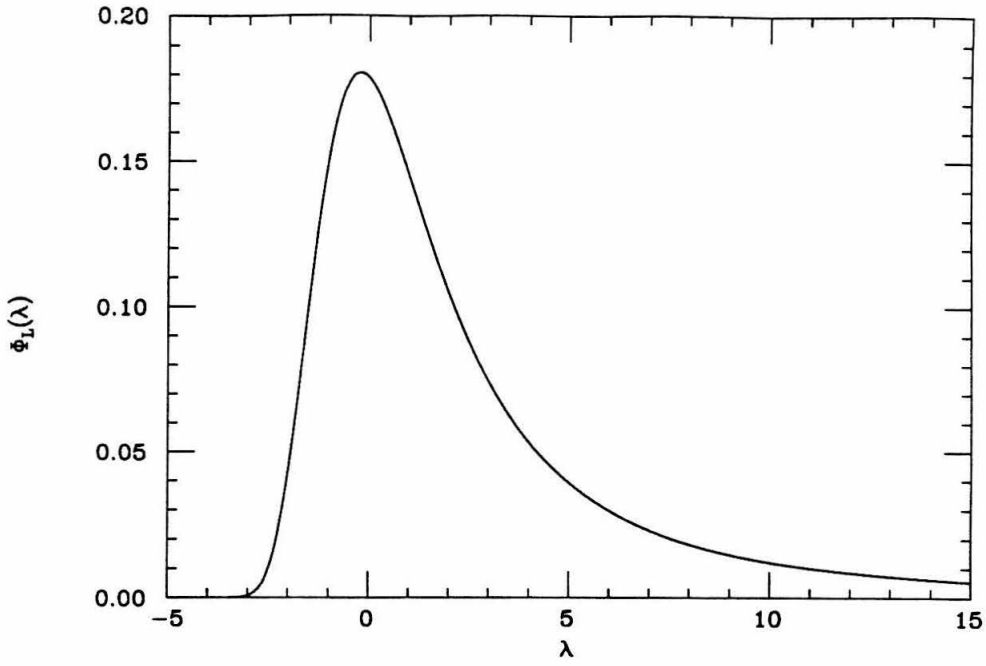

Figure A.3 – The Landau ionization energy loss spectrum. The parameter λ is defined in the text.

where CLN is the percentage of the ionization spectrum that scatters with final energy $E' > E'_{el} - \Delta E'$ (again using the energy peaking approximation), and the subscripts i and f on ξ refer to initial and final material thickness. Recall that E_0 and E' have already been corrected for the most probable energy loss (Appendix B). The value of CLN was typically 99.8% ($\Delta E'/\xi \sim 1000$).

Calculation of External Corrections

The external radiative corrections can be parameterized by a number δ_{ext}, analogous to the internal correction parameter, which is defined by relating the integral of A.11, along with the correction for the Landau tail, to the lowest order cross section:

$$e^{\delta_{ext}} \frac{d\sigma(E_0)}{d\Omega} \equiv CLN \times \int_{E'_{el}-\Delta E}^{E'_{el}} dE' \frac{d^2\sigma(E_0, E')}{d\Omega dE'} \qquad (A.16)$$

The integrand on the right hand side diverges like $1/(\Delta E')^{1-bt}$ as $\Delta E' \rightarrow 0$ due to the bremsstrahlung spectrum. Therefore when δ_{ext} was calculated the bremsstrahlung contribution was integrated analytically in the region where $\Delta E'$ is small ($E'_{el} - E' \leq 3$ MeV). In this region the cross section could be treated as a constant. The contribution at larger $\Delta E'$ was numerically integrated. The energy dependence of $d\sigma/d\Omega$ was approximated using the dipole approximation.

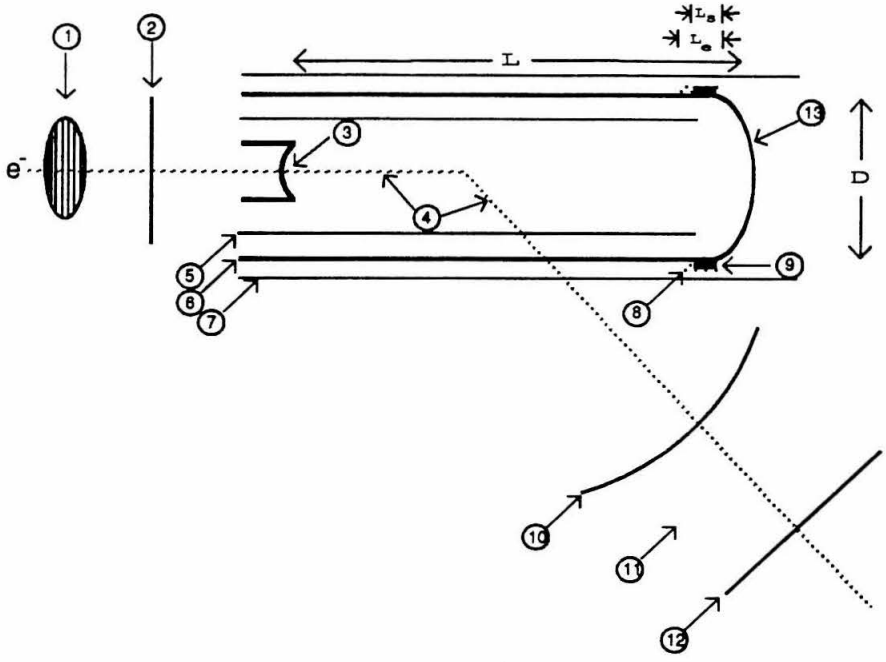

Figure A.4 – The schematic of the LH2 target used for calculating the radiation lengths before and after the scattering, t_i and t_f, for scattering along the target length.

The value of δ_{ext} depended on where in the target the electron was assumed to scatter (through the variables t_i, t_f, ξ_i, and ξ_f). It was presumed that the electrons scattered from the center of the target in the transverse direction ($X_{\rm tgt}$=$Y_{\rm tgt}$=0), and had an equal probability of scattering anywhere in the longitudinal direction along

the target ($0 \leq Z_{tgt} \leq 20$ cm). Steps of 0.5 cm were made along the target length, and the amount of material before and after the scattering, including all entrance and exit windows, etc., was calculated. The model used for the target is shown in Figure A.4, and the material properties and thicknesses are given in Table A.1. The effect of the flow guides that were accidentally bent into the beam path is discussed in Appendix C. The value of $e^{\delta_{ext}}$ averaged over the length of the target was used in the corrections. Typical values of δ_{ext} were $\sim -0.18\%$.

Item	Name	Material	τ (cm)	ρ (g/cm^3)	X_0 (g/cm^2)
1	Wire Arrays	Aluminum	0.00664	2.70	24.01
2	Hyman	Al 6061	0.00254	2.70	23.39
3	Endcap	Al 5052	0.00762	2.68	23.63
*	Flow Guide	Al 5052	—	—	23.63
4	Liquid H2	Hydrogen	—	—	63.05
5	Flow Guide	Al 5052	0.00254	2.68	23.63
6	Cell Wall	Al 5052	0.00762	2.68	23.63
7	Insulation	Mylar	0.00635	1.39	39.95
8	Epoxy	Epoxy	0.01270	1.39	39.95
9	Solder	Sn,Pb,Ag	0.00457	8.81	7.744
10	Window	Al 6061	0.03175	2.70	23.39
11	Air	N_2,O_2	82.55	0.0012	36.98
12	8GeV Window	Al 6061	0.02718	2.70	23.39
13	Endcap	Al 5052	0.00762	2.68	23.63

$L = 19.972$ cm, $L_e \approx 1.90$ cm, $L_s \approx 1.27$ cm, $D = 5.08$ cm

* see Appendix C

Table A.1 – The thicknesses and radiation lengths of the target materials.

A.4 Improvements to Internal Corrections

Because of the reduced systematic and statistical uncertainties of the present experiment, uncertainties in the radiative corrections at the level of $\approx 1\%$ caused by some of the approximations used in the previous sections were unacceptably large. In calculating the value δ_{int}, Tsai assumed that [29] $\Delta E(1 + 2E_0/M_P) \ll E'$ when the internal bremsstrahlung contributions were included. This approximation is not valid to the $\approx 1\%$ level necessary for this experiment, and an error is introduced in calculating the contribution to the elastic tail from the first diagram shown in Figure A.1(d). In this case, the electron emits a bremsstrahlung photon before scattering from the proton, giving it a lower energy and thus an enhanced scattering cross section; by as much as 50% for the kinematics considered here. Therefore the size of the elastic tail has been underestimated, and this error increases with larger values of the radiative cutoff ΔE.

The effect of this approximation can be estimated, however. Internal bremsstrahlung corrections can be approximated [76] by treating the single proton as an *external* radiator, with equivalent radiator thickness:

$$b_i t_i = b_f t_f = \frac{\alpha}{\pi}[\ln(Q^2/m_e^2) - 1] \qquad (A.17)$$

External radiative corrections due to bremsstrahlung (equation A.11) can be calculated with these equivalent radiator thicknesses, and the effect of the energy dependence of the cross section can be estimated by calculating the elastic tail with $\frac{d\sigma}{d\Omega}$ approximated with the dipole form factors relative to the same calculation assuming a constant cross section (no energy dependence). This contribution to the internal correction, δ'_{int}, is defined by:

$$e^{\delta'_{int}} \equiv \int dE' \, \frac{d^2\sigma(E_0, E')}{d\Omega dE'}^{dipole} \Big/ \int dE' \, \frac{d^2\sigma(E_0, E')}{d\Omega dE'}^{const} \qquad (A.18)$$

This correction ranged from 0.2-3.0%, and had a strong $\Delta E'$-cut and ε dependence. Without this correction term, the cross sections showed [77]a strong ($\sim$ 1-2%) dependence on the $\Delta P/P_0$ cut.

Vacuum polarization contributions from $\mu^+\mu^-$ and $q\bar{q}$ loops were also neglected. The muon loop was calculated from:

$$\delta^{\mu}_{vac} = \frac{2\alpha}{\pi}\Big[-\frac{5}{9} + \frac{4}{3}\frac{M_\mu^2}{Q^2} + \Big(\frac{1}{3} - \frac{2}{3}\frac{M_\mu^2}{Q^2}\Big)\ln\Big(\frac{Q^2}{M_\mu^2}(1+\sqrt{1+\frac{4M_\mu^2}{Q^2}})\Big)\Big] \qquad (A.19)$$

where $M_\mu = 0.10566$ GeV is the muon mass. This contribution is the same as the electron loop contribution in the limit of $Q^2 \gg M_\mu^2$. Quark loop corrections [78] were performed using a simple fit to the previous equation for all flavors of quarks (including the color factor) which was valid for $1 \leq Q^2 \leq 64$ (GeV/c)^2:

$$\delta^{q}_{vac} = -2\Big(-1.513\times10^{-3} - 2.822\times10^{-3}\ln(1+1.218Q^2)\Big) \qquad (A.20)$$

An additional correction by Schwinger [79] was included by Tsai [52] to correct for the noninfrared divergent part of the soft photon emission cross section. A sign error in Tsai's paper [52] has since been corrected [80], giving the term:

$$\delta_{Sch} = \frac{-\alpha}{\pi}\Big[\frac{\pi^2}{6} - \Phi(\cos^2(\theta/2))\Big] \qquad (A.21)$$

All these effects were then included in the definition of δ'_{int}:

$$\delta'_{int} \rightarrow \delta'_{int} + \delta^{\mu}_{vac} + \delta^{q}_{vac} + \delta_{Sch} \qquad (A.22)$$

Combining all of the above effects, the radiative correction, $RCOR$, is defined:

$$RCOR \equiv e^{(\delta_{int}+\delta'_{int}+\delta_{ext})} \qquad (A.23)$$

This value of $RCOR$ was used to correct the measured cross sections for the higher order radiative effects. Different values of the radiative corrections used for this experiment are tabulated in Appendix D.

Appendix B
Kinematic Calibration

It was important to have systematic uncertainties in E_0, E', and θ well controlled since these are correlated with ε. The A-bend and spectrometer energies were calibrated, and the incident beam position and angle and spectrometer angle were measured. The ionization energy loss of the electrons in the target was calculated, and the centroid of the incident beam energy distribution was determined. These considerations are discussed below.

B.1 Spectrometer Survey

The spectrometer angle was measured with respect to the nominal beam axis before the experimental data run. The spectrometer was set at an angle of approximately 70°, and the angle was measured relative to a 70° scribe mark on the ESA wall. Due to a problem with the spectrometer angle encoder just before the experiment was about to begin, the survey needed to be done quickly and without access to the pivot. The encoder was set to only the approximate value of the angle. A more extensive survey of the spectrometer was performed after the experiment at eight different angles from 12° to 46°. These measurements indicated an offset of 0.049° in the encoder setting. The measurement of the spectrometer angle was accurate to ±0.003°.

A pointer was attaced to the spectrometer that pointed to a scribe line on the ESA floor when the spectrometer was set at 30.000°. A video camera mounted on the spectrometer allowed this pointer to be periodically observed, guaranteeing that

the angle encoder value did not change during the experiment. Previous extensive surveys of the spectrometer indicated that the angle encoder functioned properly over the entire range of spectrometer angle settings. In addition, these measurements indicated that the pivot position was stable to 0.27 ± 0.07 mm when the spectrometer was moved, and that the vertex position (where the spectrometer central ray intersects the beam path) was stable to 6.9 ± 0.1 mm.

The position of the wire chambers in the detector hut was also measured relative to the nominal central ray. These measurements were accurate to ± 1 mm in the wire chamber position and ± 0.5 mr in the relative wire chamber rotations.

B.2 Wire Orbit

The wire orbit [16,17], in addition to studying the transport characteristics of the spectrometer, was able to calibrate the $\Delta P/P_0$ and $\Delta\theta$ values of the nominal central ray of the spectrometer. The data indicated that the nominal ray in the detector hut had an offset in the horizontal angle at the target of $-0.010°$. This offset was possibly caused by a rotation in one or more of the quadrupole magnets relative to their nominal positions.

The difference between the central value of the spectrometer momentum and the nominal momentum setting is shown in Figure B.1. The initial calibration of the central momentum was determined with dark current studies [14], conducted in 1967, with the spectrometer set at zero degrees (relative to the beamline). These studies were carried out at 3, 6, 8 and 9 GeV. From this data a fifth order polynomial for the current in the spectrometer magnets, as a function of momentum, was determined. This polynomial was used to include the effects of residual fields at zero current as well as saturation effects at high momentum settings. Data from the wire orbit indicated that this current equation gave the proper momentum setting at the points that were

fit (3, 6, 8, and 9 GeV), but residual discrepancies on the order of ±0.1% still exist. Two sets of wire orbit data were taken with different tensions placed on the wire. These data were in good agreement in the area of the data overlap (0.5-4.0 GeV), indicating that systematic errors were well controlled. Measurements were taken at each of the momenta several times, indicating a repeatability of the spectrometer momentum setting to ±0.025%.

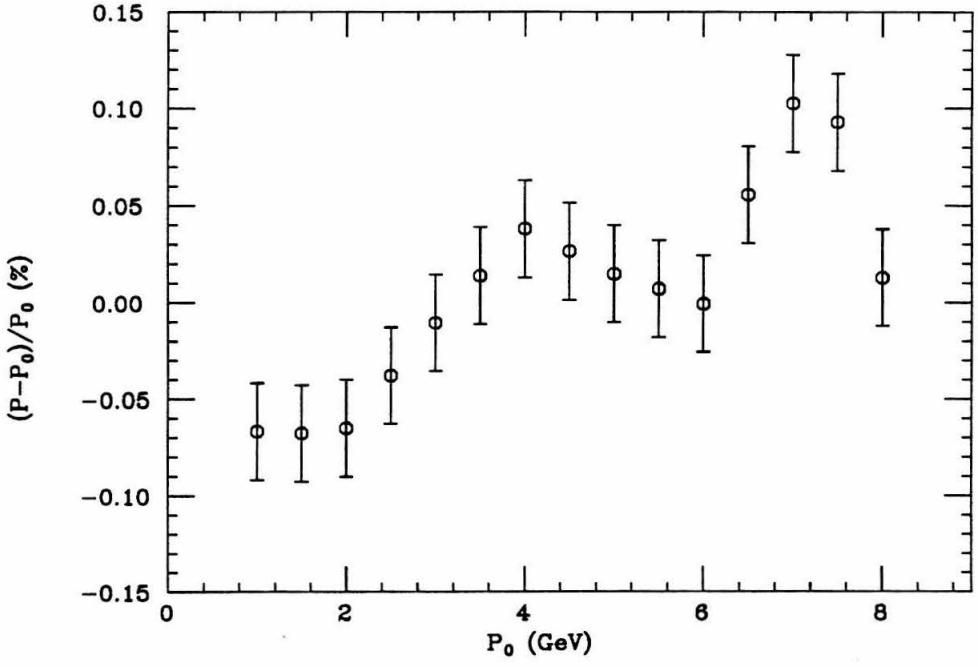

Figure B.1 – The absolute momentum calibration of the spectrometer central momentum (P) relative to the nominal setting (P_0) from the wire orbit.

B.3 Ionization Losses

Electrons in the beam lost energy as they passed through the target material due to the ionization of atomic electrons within the target. The nominal value of

the incident beam energy (and spectrometer momentum setting) was corrected for the most probable energy loss an electron would experience as it entered (exited) the target by subtracting (adding) the energy loss calculated from the equation [81-83] valid in the ultra-relativistic limit:

$$\begin{aligned}\Delta E_{mp} =& \frac{2\pi\alpha^2(\hbar c)^2 N_A}{mc^2}\left(\frac{Z}{M_A}\right)t\left[\ln\left(\frac{\alpha mc^2}{\hbar c}(\frac{t}{\rho}\right) + 0.198\right] \\ =& 0.15354\left(\frac{Z}{M_A}\right)t\left[\ln\left(1.8897\times 10^8(\frac{t}{\rho})\right) + 0.198\right] \qquad (B.1)\end{aligned}$$

where N_A is Avogadro's constant, t = the length of material in (g/cm^2), Z = the atomic number of the nucleus, M_A is the atomic mass of the nucleus, ρ is the density of the material in (g/cm^3), and ΔE_{mp} is given in MeV. The most probable energy loss was averaged over the target length assuming a uniform probability of scattering along the target. The typical size of this correction was 2.5 MeV.

B.4 Beam Steering

Offsets of the beam position and angle at the pivot can cause offsets in the measured momentum and angle of the scattered electron in the detector hut. The SLAC computer program TRANSPORT was used to estimate the effects of beam position and angle on the various kinematic quantities measured. The beam's horizontal and vertical angle were related to the measured values of $\Delta\theta$ and $\Delta\phi$, respectively, by a simple 1:1 relationship. Offsets in the beam's vertical position, $Y_{\rm tgt}$, caused offsets in the detected momentum fraction; this offset was related by $d(\Delta P/P_0)$=0.3183$\times Y_{\rm tgt}$, where $\Delta P/P_0$ is in % and $Y_{\rm tgt}$is in cm. The target reconstruction algorithm assumed that the scattering takes place at $X_{\rm tgt}$=0, so offsets in the beam's horizontal position caused offsets only in the measured target position along the beam, $Z_{\rm tgt}$. These were related by the simple geometric relationship $Z_{\rm tgt}$= tan(θ)$X_{\rm tgt}$. It was not important

for the kinematics of the scattering to know the precise target position so this correction was ignored. For certain data runs the beam was deliberately displaced by 3 mm in either the vertical or horizontal direction. The offsets in the observed elastic peak positions for these runs were consistent with the TRANSPORT predictions.

Only data which was taken with the beam steering operating properly are included in this analysis, so the above corrections were typically extremely small. The beam position was known at both the wire array and microwave cavity monitor to better than ± 1 mm. This lead to a typical uncertainty in the beam position and angle at the pivot of ± 0.1 cm and ± 0.03 mr, respectively, causing an uncertainty in $\Delta P/P_0$ of 0.03% and in $\Delta\theta$ and $\Delta\phi$ of 0.03 mr.

B.5 Elastic Peak Calibrations

The kinematic constraint that elastic scattering occurs at $x = 1$ allows a useful method to calibrate the incident and final electron energy. Measurements of the elastic peak positions at a variety of kinematics yields a measurement of the incident energy relative to the spectrometer momentum setting. Combining this information with the absolute calibration of the spectrometer provided by the wire orbit, an absolute calibration of the beam energy was possible. These measurements also indicated differences between the average beam energy in a particular run and the nominal central value measured by the flip-coil caused by a nonsymmetric distribution of the beam within the energy defining slits. A run-by-run correction of the absolute beam energy can thus be determined.

B.5.1 Procedure for De-radiating Spectra

The ($\Delta P/P_0$, $\Delta\theta$, $\Delta\phi$) histograms that were generated in the Pass-1 analysis were converted into one-dimensional missing mass squared (W^2) histogram. The values of E_0, E', and θ that were used included all the corrections noted above. Corrections were made for acceptance effects and the $\Delta\theta$ dependence of the cross section across the acceptance. A typical W^2 histogram measured with the LH2 target is shown in Figure B.2. Similar measurements were done with the aluminum DUM target, and these were then subtracted from the LH2 histograms to exclude the contributions from endcaps and flow guides. These spectrum have all been checked to guarantee that the distribution of events in the super-elastic regions was statistically consistent with a flat, zero contribution.

Radiative effects, as described in the Appendix A, shift the cross section from lower to higher W^2. When this effect is folded in with the resolution of the spectrometer and the spread in the incident beam energy, the W^2 value where the maximum of the elastic peak occurs is shifted to $W^2 > M_p^2$. This effect must be included before the peak position can be determined.

The unfolding procedure was based on the de-radiating prescription of P.N. Kirk, *et al.* [13]. Radiative tails of the lower W^2 bins were subtracted from the higher W^2 bins on a bin-by-bin basis. First a low W^2 bin which was not contaminated by radiative tails from smaller W^2 bins was chosen, such as the first bin above the super-elastic cutoff (see Appendix C). This bin was corrected for the total radiative losses expected from the radiative corrections procedure of Mo and Tsai [29,32,52] (see Appendix A), and the contributions of this radiative tail were subtracted from each of the higher W^2 bins. If we let σ_1 = the measured cross section in the lowest (radiatively uncontaminated) bin, σ_i = the measured cross section in bin i, RCOR(W^2) = the

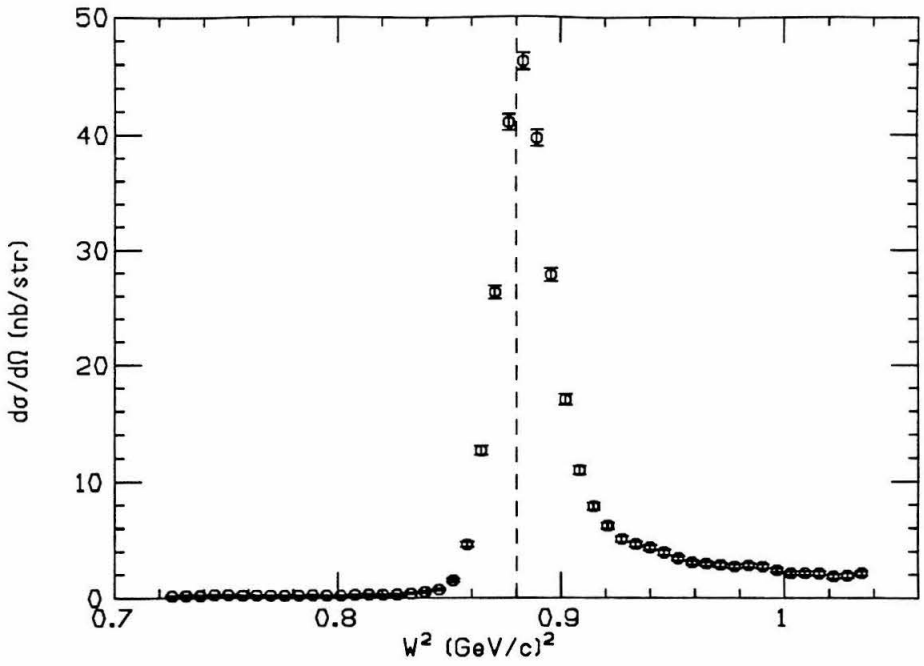

Figure B.2 – A typical missing mass squared histogram measured with the LH2 target. The elastic peak position, neglecting radiative effects, should occur at $W^2 = M_p^2 = 0.88035$ (GeV/c)² (dashed line).

radiative correction for a missing mass squared cut of W^2 (with the assumption $x = 1$ corresponds to $W^2{=}M_p^2$), and δW^2 be the histogram bin width, the radiative contributions from this first bin can be unfolded by:

$$\sigma_1' \equiv \sigma_1 / R_1 \tag{B.2}$$

$$\sigma_i' \equiv \sigma_i - \sigma_1' \times R_i \tag{B.3}$$

$$R_i \equiv \int_0^{\delta W^2} dw' \left[\mathrm{RCOR}\left(i\delta W^2 - w' + M_p^2 \right) - \mathrm{RCOR}\left((i-1)\delta W^2 - w' + M_p^2 \right) \right] \tag{B.4}$$

where σ' indicates the components of a new, partially radiatively corrected W^2 histogram.

The second bin above the super-elastic cutoff (σ_2') has thus been corrected for the contribution of the radiative tail from the lower W^2 bin (σ_1'), and can now be radiatively corrected with the same procedure. This was done to succesively higher W^2 bins, until the entire spectrum had been de-radiated. Error bars assigned to each bin must be handled carefully to include the effects of correlations between the W^2 bins after de-radiating. Confusion can be avoided by relating the components of the completely de-radiated spectrum (σ_i^0) directly to those of the measured spectrum (σ_i) with the matrix equation:

$$\begin{pmatrix} \sigma_1^0 \\ \sigma_2^0 \\ \sigma_3^0 \\ \vdots \\ \sigma_n^0 \end{pmatrix} = \begin{pmatrix} a_1 & 0 & 0 & \dots & 0 \\ a_2 & a_1 & 0 & \dots & 0 \\ a_3 & a_2 & a_1 & \dots & 0 \\ \vdots & \vdots & \vdots & \ddots & \vdots \\ a_n & a_{n-1} & a_{n-2} & \dots & a_1 \end{pmatrix} \begin{pmatrix} \sigma_1 \\ \sigma_2 \\ \sigma_3 \\ \vdots \\ \sigma_n \end{pmatrix} \tag{B.5}$$

where:

$$\begin{aligned} a_1 &\equiv \frac{1}{R_1} \\ a_n &\equiv -a_1 \sum_{i=2}^{n} R_i a_{n-i+1} \end{aligned} \tag{B.6}$$

The uncertainty squared of each bin of the de-radiated spectrum $(\Delta\sigma_i^0)^2$ can then be computed by simply taking the sum of the squares of the uncertainties of the measured bins $(\Delta\sigma_j)^2$ weighted by the proper component of the de-radiating matrix (a_{i-j+1}^2).

A typical de-radiated spectrum is shown in Figure B.3. Note that the error bars shown for each bin are the proper statistical error bar for that particular bin. Bin-to-bin correlations exist in the values of the de-radiated cross sections, however, and thus the uncertainties involved when comparing values between bins are somewhat smaller than a naive interpretation would indicate. These correlations are especially

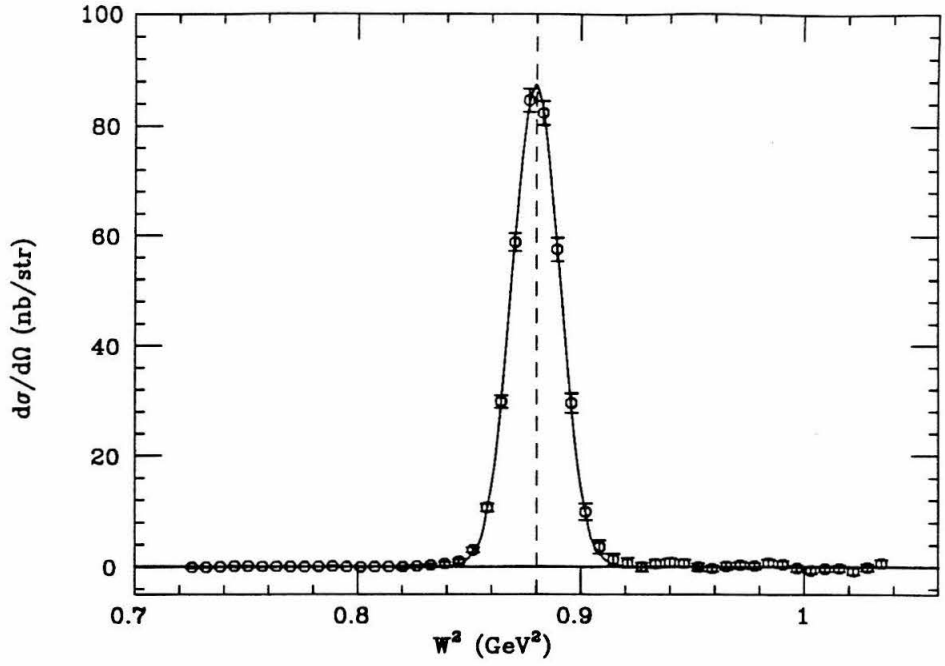

Figure B.3 – A typical W^2 histogram after the effects of the radiative tail have been unfolded. The solid line is a least-squares fit of a gaussian to the spectrum. The dashed line is the expected value of the peak position, $W^2 = M_p^2 = 0.88035$ (GeV/c)^2.

strong at the higher W^2 bins where large subtractions of the elastic radiative tails have been made.

B.5.2 Fits to De-radiated Spectra

Each de-radiated spectrum was fit to a gaussian shape. Only the central 7 bins near the peak maximum were fit. From these fits the gaussian height A_0, peak position W_0^2, and peak width δ_{W^2} were extracted for each run, along with their uncertainties. The typical χ^2/dof for these fits was 0.35. The χ^2/dof to the entire spectrum, as compared to only the central bins included in the fit, was typically 0.65. These small values of χ^2/dof were caused by the large correlations between the values in

different bins, and thus indicated a overly conservative estimate of the uncertainties of the extracted parameters. From these measured values of the peak positions, the calibration of the incident and final energies could be carried out.

B.5.3 Absolute Energy Calibration

An offset in the measured peak positions, W_0^2, relative to the kinematic constraint, $W^2 = M_P^2$, can be related to offsets in the kinematic variables. This offset, $dW^2 = W_0^2 - M_P^2$, is related to the offsets in the incident and final energies and scattering angle by:

$$\begin{aligned} dW^2 &= E_0 \frac{\partial W^2}{\partial E_0}\frac{dE_0}{E_0} + E' \frac{\partial W^2}{\partial E'}\frac{dE'}{E'} + \frac{\partial W^2}{\partial \theta} d\theta \\ \frac{\partial W^2}{\partial E_0} &= 2M_p - 4E' \sin^2(\theta/2) \\ \frac{\partial W^2}{\partial E'} &= -2M_p - 4E_0 \sin^2(\theta/2) \\ \frac{\partial W^2}{\partial \theta} &= -4E_0 E' \sin(\theta/2)\cos(\theta/2) \end{aligned} \qquad (B.7)$$

The contribution of the $d\theta$ term was very small due to the high precision of the scattering angle known from the spectrometer survey, wire orbit, beam steering, and event tracking and was neglected.

An estimate of the necessary energy offsets needed to explain the peak offsets can be performed by setting one of the energy offsets to zero, and assuming that the offset was due entirely to the other energy. The results of this analysis are shown in figure B.5. A fit to a constant, average offset in either the incident energy or the final energy was performed with the above data. If the offsets were assumed to be entirely due to dE_0/E_0, the average offset (dashed line (a)) was found to be -0.146%, with a χ^2/dof=2723/61. If the offsets were assumed to be entirely due to dE'/E', the average offset (dashed line (b)) was found to be 0.111%, with a χ^2/dof=1614/61.

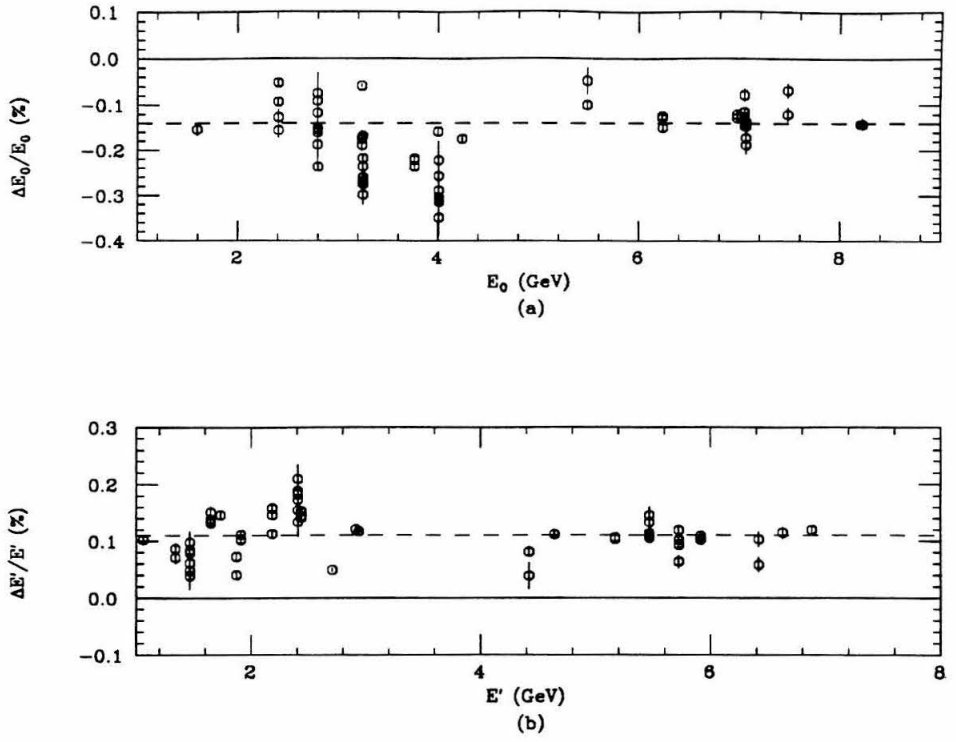

Figure B.4 – One-parameter analysis of the peak positions offsets. (a) The offset in the incident energy, dE_0/E_0 assuming no offset in the final energy. (b) The offset in the final energy, dE'/E', assuming no offset in the incident energy.

These large values of χ^2 were caused by fluctuations of the peak positions around these average offsets, and were consistent with a typical $\pm 0.05\%$ fluctuation in the incident beam energy. Since the full width spread in the incident beam energy was up to 0.3%, fluctuations of this order were not surprising.

The different kinematic dependence that the offsets dE_0/E_0 and dE'/E' have on the peak offset dW^2 can, in principle, allow for a two-dimensional separation of these absolute offsets. However, since the kinematic terms are highly correlated and the fluctuations in the average incident beam energy tend to be significant compared to the average offset, it was difficult to get separate constraints on both the incident and final energies. It was therefore decided to correct the final energy by 0.055%, and the

incident energy by −0.07%. The 0.055% shift in the spectrometer momentum was consistent with the uncertainty in the absolute calibration of the wire orbit ($\sim$ 0.05%) and the accuracy of the beam steering system ($\sim$ 1 mm). Since the cross section was only a function of the incident energy and scattering angle ($x \equiv 1$), shifts in the final energy had no direct effect on the measured cross sections. A systematic uncertainty of ±0.07% was included in the absolute incident energy calibration to account for the incident energy correction, but this uncertainty had only a small effect on the final extracted form factors.

B.5.4 Incident Energy Fluctuations

After the absolute energy calibration was accomplished, small fluctuations in the peak positions were still observed (see Figure B.5). These fluctuations were, as discussed above, consistent with $\sim$ 0.05% run-to-run fluctuations in the incident energy. The incident energy for each run was corrected assuming these peak fluctuations were caused entirely by differences between the average energy of the beam and the central value defined by the A-bend slits. Run-to-run fluctuations in the beam steering system ($\sim$ 1 mm) and in the spectrometer momentum calibration ($\sim$ 0.025%), could also contribute to these peak position fluctuations. A 0.03% systematic uncertainty was assigned to the point-to-point relative energy calibration to account for these uncertainties.

B.5.5 Resolution

The widths of the elastic peaks were also extracted from the de-radiated peak spectrum. Contributions to the width of the elastic peaks were from the incident energy spread ($\Delta E/E_0$=full width), multiple scattering of the electrons in the detector hut (principally from the Čerenkov mirror), and the resolution of the wire chambers

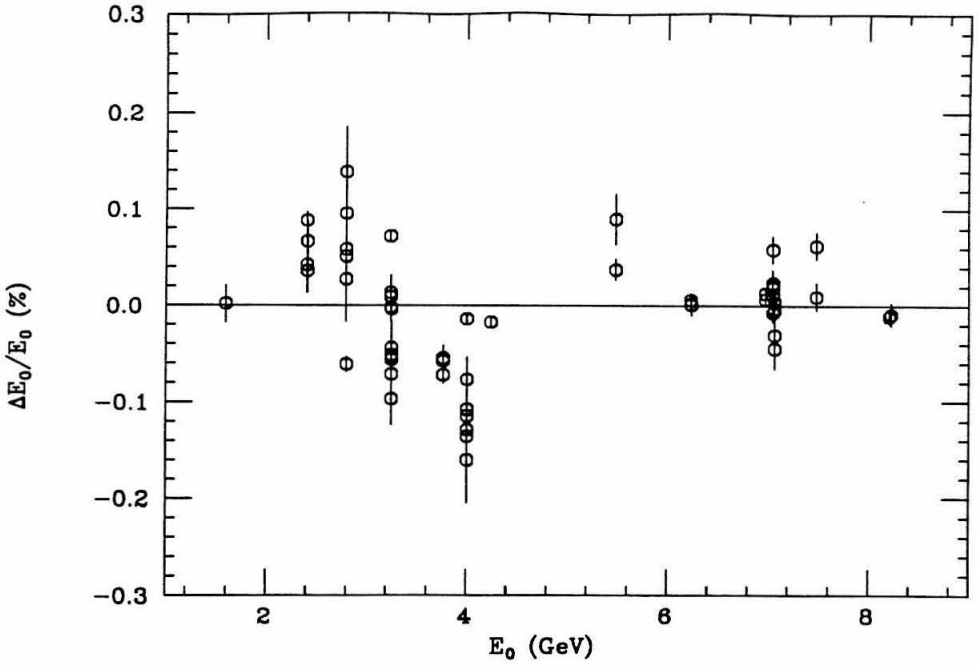

Figure B.5 – Run-to-run fluctuations in the relative incident beam energy extracted from elastic peak locations.

($\sim$ 2 mm) A rough model based on these effects gave an expected peak width (in $\Delta P/P_0$) of:

$$\begin{aligned}
\delta_{exp} &= \sqrt{\delta_{E_0}^2 + \delta_{ms}^2 + \delta_{wc}^2} \\
\delta_{E_0} &= \frac{1}{2\sqrt{3}} \frac{\Delta E_0}{E_0} \frac{E_0}{E'} \left(\frac{\partial E'}{\partial E_0}\right)\Big|_{x=1} \\
\delta_{ms} &= \frac{0.14\%}{E'} \\
\delta_{wc} &= 0.07\%
\end{aligned} \tag{B.8}$$

where δ_{exp} is an absolute number, and all energies are in GeV. A comparison between the measured peak widths and this model is shown in Figure B.6. In addition to these intrinsic effects, an additional contribution to the width of the peaks was caused by

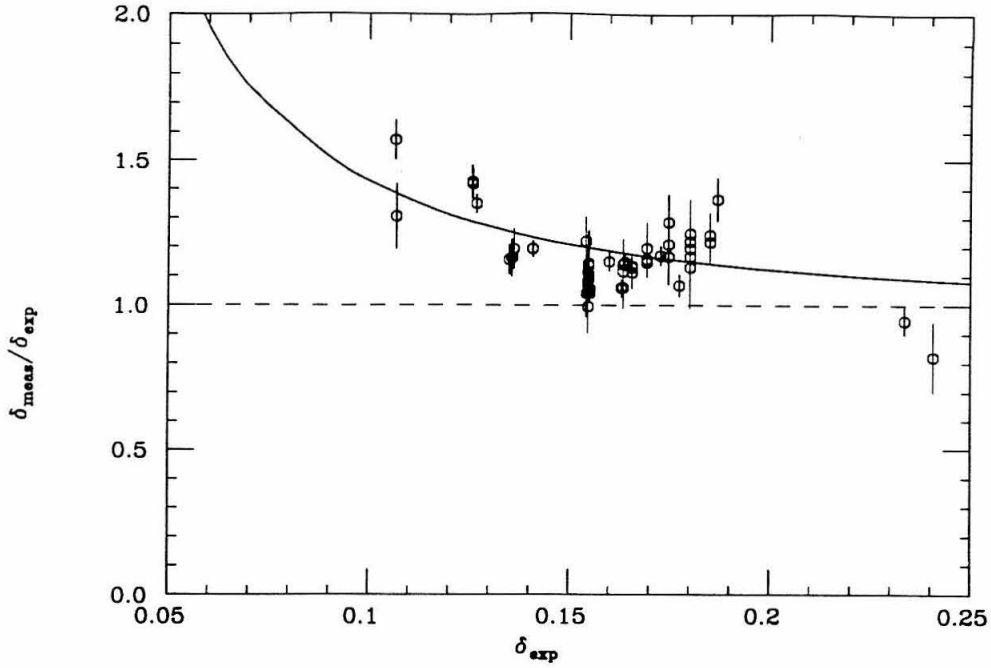

Figure B.6 – Comparison between the measured elastic peak widths in $\Delta P/P_0$ (δ_{meas}) and the expected peak widths (δ_{exp}) that was based on a rough model described in the text. The solid line is also described in the text.

the 0.25% $\Delta P/P_0$ bin width of the three-dimensional histogram generated in the Pass-1 analysis that was converted to the W^2 histogram. This effect must also be included:

$$\delta_{tot} = \sqrt{\delta_{exp}^2 + \delta_{hist}^2}$$
$$\delta_{hist} = \frac{0.25\%}{2\sqrt{3}} \qquad (B.9)$$

and is represented by the solid line in Figure B.6. The model agrees well with the data when this effect is included. Resolution effects caused by the intrinsic width of the peaks (δ_{exp}) were included in the corrections for the radiative tail. These corrections were usually very small ($\sim 0.01\%$).

Appendix C
Subtraction of Aluminum Background

Contributions to the detected electron rate from the LH2 target involved scattering from both the liquid hydrogen and the Al endcaps of the target. In addition, an accidental reversal of the flow of the liquid H_2 through the Al flow guides of the target caused the flow guides to be bent into the path of the beam during part of the experiment. It was important to know how much aluminum was present in the beam path and subtract this background from the measured cross section. This material also contributed to the external radiative corrections (see Appendix A). The effect this material had on the radiative processes of the electrons scattered from the hydrogen will also be discussed.

C.1 Reversed Liquid Hydrogen Flow

During the experimental run, it was noticed that additional electrons were detected above the elastic peak ($\nu < Q^2/2M_p$) that were not accounted for from the endcap contributions alone. An on-line analysis of this problem lead to the discovery that the hydrogen flow through the target was incorrect. In Figure C.1 a schematic of the hydrogen target with the correct flow path is shown: the hydrogen flows in through the center flow guide (0.00254 cm thick aluminum) and out between the flow guide and the target wall. The pressure inside the flow guide, $P0$, is larger than the pressure outside, $P1$. However, when the hydrogen flows in the opposite direction, the pressure $P1 > P0$, and the flow guide is pushed inwards. The combination of the flexibility of the flow guide, the flow rate of the hydrogen (> 1 m/s), and the

difference in the cross sectional areas of the inner and outer flow paths (inner area ~ 12.6 cm^2, outer area ~ 7.7 cm^2) could easily cause the flow guide to be bent into the beam path. Correction of the flow direction before the end of the experiment substantially reduced the rate of scattering above the elastic peak in subsequent data runs, giving support to the theory that the flow guides were, in fact, the cause of this additional background.

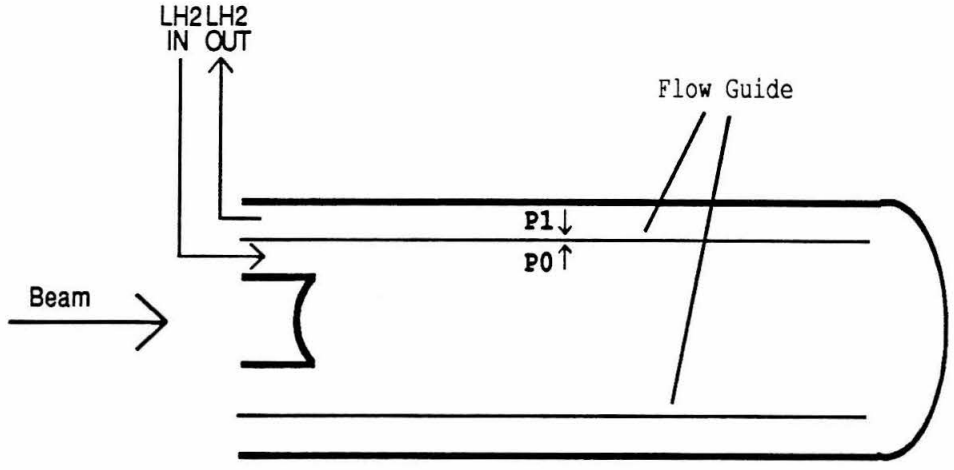

Figure C.1 – Schematic of the LH2 target under proper running conditions.

C.2 Determination of Aluminum Background

A "super-elastic" cross section was defined as the cross section in the region $\nu < Q^2/2M_p$. While electrons scattered from hydrogen were kinematically forbidden

in this region, scattering from the Al endcaps was allowed due to the Fermi momentum [84] of the nucleons within the aluminum nucleus. Thus the super-elastic cross section was proportional to the total amount of aluminum in the beam path.

The statistics in the super-elastic region were typically rather low; usually $\sim$ 100 counts. Thus the bin-by-bin statistics were very low and did not easily lend themselves to a statistical analysis. For this reason a model of the quasi-elastic plus deep inelastic scattering cross section from aluminum was developed to assist analysis of the distribution of events within the acceptance. The quasi-elastic model was based on a y-scaling formalism [85,25] fit to previous data. The inelastic contribution was taken from the fit [23] to deuterium data and was Fermi smeared. Higher order radiative processes were also included using the procedure of Mo and Tsai [32,52]

In order to make the kinematic corrections for variations in the beam energy from run-to-run, it was desirable to define the super-elastic cross section at the center of the acceptance region ($\Delta P/P_0$=0,$\Delta\theta$=0). The super elastic cross section was defined (including an overall constant, SE_0, which incorporates units, dead-time, etc.):

$$\begin{aligned} \frac{d^2\sigma^{SE}}{d\Omega dE'} &= \mathrm{SE}_0 \times \frac{\mathrm{N}_{SE}}{\mathrm{ACC}_{SE}} \times \mathrm{R}_{SE} \\ \Delta\left(\frac{d^2\sigma^{SE}}{d\Omega dE'}\right) &= \mathrm{SE}_0 \times \frac{\sqrt{\mathrm{N}_{SE}}}{\mathrm{ACC}_{SE}} \times \mathrm{R}_{SE} \end{aligned} \qquad (C.1)$$

with:

$$\mathrm{N}_{SE} \equiv \sum_{\Delta P/P_{0i},\Delta\theta_j}^{SE} \mathrm{HIST2}(\Delta P/P_{0_i},\Delta\theta_j) \qquad (C.2)$$

$$\mathrm{ACC}_{SE} \equiv \frac{\Sigma_{ASW}}{\Sigma_{SW}}\Sigma_W \qquad (C.3)$$

$$\mathrm{R}_{SE} \equiv \frac{\Sigma_W}{\Sigma_{SW}}\sigma^{\mathrm{Model}}(\Delta P/P_0{=}0,\Delta\theta{=}0) \qquad (C.4)$$

where N_{SE} is the total number of counts detected in the super-elastic region, ACC_{SE} is the acceptance (weighted by the cross section) in ($mr^2 \cdot$ GeV), and R_{SE} is the ratio of the model cross section at the center of the acceptance to the cross section averaged over the super-elastic region. The following definitions have been used:

$$\Sigma_{ASW} \equiv \sum_{\Delta P/P_{0i},\Delta\theta_j}^{SE} \mathrm{ACC2}(\Delta P/P_{0_i},\Delta\theta_j)\sigma^{\mathrm{Model}}(\Delta P/P_{0_i},\Delta\theta_j)\mathrm{WGT}_{ij} \quad (C.5)$$

$$\Sigma_{SW} \equiv \sum_{\Delta P/P_{0i},\Delta\theta_j}^{SE} \sigma^{\mathrm{Model}}(\Delta P/P_{0_i},\Delta\theta_j)\mathrm{WGT}_{ij} \quad (C.6)$$

$$\Sigma_{W} \equiv \sum_{\Delta P/P_{0i},\Delta\theta_j}^{SE} \mathrm{WGT}_{ij} \quad (C.7)$$

and:

$$\mathrm{WGT}_{ij} = (\Delta\phi_{hi} - \Delta\phi_{lo})(E' \times (\delta P/P_0)_i)(\delta\theta_j) \quad (C.8)$$

The notation is similar to that of Chapter 4. Kinematic cuts on the super-elastic region were defined as $-6 \leq \Delta\theta \leq 5$ mr and $p_{hi} \leq \Delta P/P_0 \leq 3\%$. The constant SE_0 was analogous to CR_0 in Chapter 4, and included corrections for dead-time, etc. It was defined by:

$$\mathrm{SE}_0 = \frac{1}{0.6022}\frac{DT}{(Beam \cdot Eff \cdot t_{Al} \cdot Acc_{cor})} \quad (C.9)$$

where t_{Al} is the thickness of *only* the aluminum endcaps in the target: 0.01524 g/cm^2 for the LH2 target and 0.2469 g/cm^2 for the DUM target. The model used for computing the acceptance and the centering correction was checked against previous measurements [85,25] of $e-$Al inclusive scattering in this Q^2 regime and was found to agree, in absolute cross sections, to 10%. The super-elastic cross section values changed by $< 1\%$ when a uniform cross section in E' and θ ($\sigma^{\mathrm{model}} \equiv 1$) was used instead of this more realistic model.

These cross sections were then used to extract the total amount of aluminum present in the LH2 target. If t_{Al}^{H2} is defined as the thickness of the endcaps alone and $t_{Al}^{H2'}$ as the total thickness of the aluminum in the beam path of the LH2 target (in g/cm^2), they can be related to the measured super-elastic cross sections of the DUM and LH2 targets by:

$$\left(\frac{d^2\sigma^{SE}}{d\Omega dE'}\right)_{DUM} = \left(\frac{d^2\sigma^{SE}}{d\Omega dE'}\right)_{LH2} \times \frac{t_{Al}^{H2}}{t_{Al}^{H2'}} \qquad (C.10)$$

Remember the super-elastic cross sections were defined assuming only the Al endcap contributions. A normalization factor, DF, can be defined as the ratio of measured to nominal aluminum thickness in the LH2 target:

$$\mathrm{DF} \equiv \frac{t_{Al}^{H2'}}{t_{Al}^{H2}} = \left(\frac{d^2\sigma^{SE}}{d\Omega dE'}\right)_{LH2} \Big/ \left(\frac{d^2\sigma^{SE}}{d\Omega dE'}\right)_{DUM} \qquad (C.11)$$

A factor of one would indicate that the aluminum in the target was entirely accounted for from the endcap contributions. A plot of DF versus time is shown in Figure C.2. It is clearly seen that when the LH2 flow was restored to the proper direction ($t \approx 39$ days), the dummy factor was reduced to a factor close to one. The average factor before the flow was corrected was 4.43 ± 0.12 (χ^2/dof=64/52); after the correction it was 1.28 ± 0.12 (χ^2/dof=10/7). Deviations of the normalization from 1.0 after correction of the flow direction were accounted for by the contamination of the liquid hydrogen by deuterium (D/H$\approx$ 0.16%, measured in atoms, leads to D/Al$\approx$ 13%, measured in g/cm^2 where Al represents only the endcap contributions of the LH2 target) and uncertainties in the measured endcap thickness of the LH2 target ($\sim$ 10%). The total LH2 target thickness under optimal conditions (DF= 1) was 2.41% r.l. (1.453 g/cm^2); with DF= 4.43, the thickness was increased to 3.01% r.l. (1.593 g/cm^2). For comparison, the DUM target thickness was 2.80% r.l. (0.662 g/cm^2).

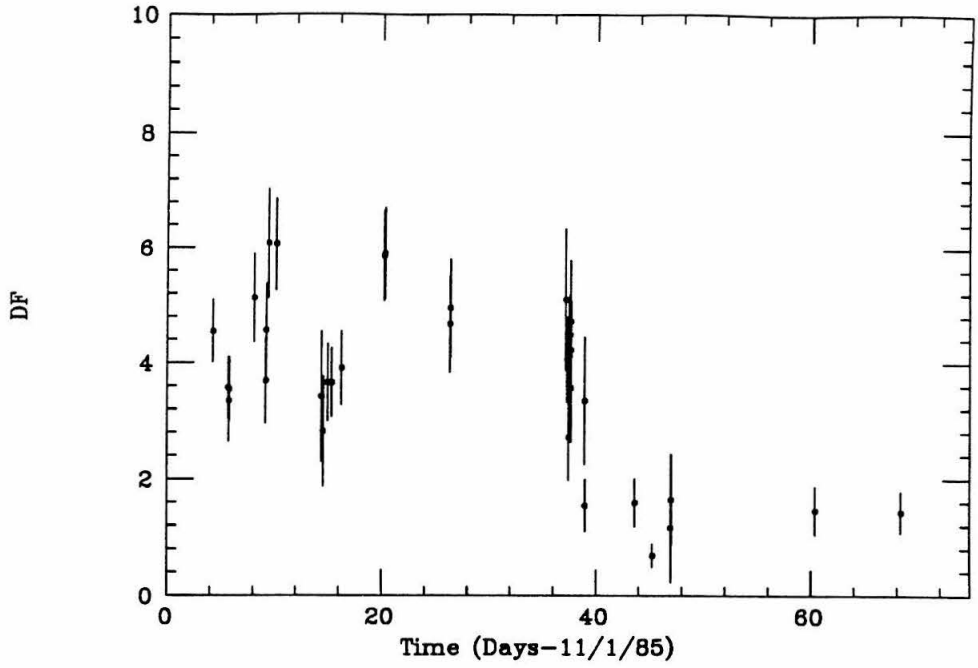

Figure C.2 – The normalization factor (DF, defined in the text) for the dummy target subtraction as a function of time.

C.3 Effect on Radiative Corrections

The additional aluminum in the beam path not only affects the scattering rate by directly scattering electrons itself; it also affects it indirectly by external radiative effects (see Appendix A) as the electrons pass through the material before scattering from the hydrogen. However, while material inserted in the beamline at the upstream end of the target (defined here as $Z = -10$ cm) can cause electrons to produce additional bremsstrahlung photons before scattering from the hydrogen, material at the downstream end ($Z = +10$ cm) will have no effect. It is therefore important to understand not only *how much* additional material was placed in the beam path (DF), but also the *distribution* of the aluminum within the target.

The flow guide extended almost the entire length along the target and was supported at the upstream end. The downstream end was completely free, and was only supported by the pressure of the hydrogen flowing through the target. Since the upstream end could not be bent into the beam path while the downstream end could, it was expected that the aluminum distribution might plausibly be shifted in the $+Z_{\rm tgt}$direction relative to the hydrogen distribution.

Although DF was a direct measure of the total quantity of aluminum along the beam path, there was no way to know the precise details of the distribution across the cross sectional area of the beam or along the beam path. This is not a problem, however, if the radiative corrections are linear with respect to the amount of material the beam passes through. If it is assumed that a fraction of the beam, α, passed through an additional amount of material from the flow guides, $\frac{\Delta t_{Al}}{\alpha}$, and the remaining $1-\alpha$ fraction of the beam passed through no additional material (average amount of material $\equiv \Delta t_{Al} = ({\rm DF}-1)t^{Al}_{LH2}$), the linearity of the radiative corrections can be tested by calculating ${\rm RC}(\alpha) \equiv \alpha {\rm RCOR}_{\frac{\Delta t_{Al}}{\alpha}} + (1-\alpha)\ {\rm RCOR}_0$. The subscript on RCOR indicates the additional amount of material placed in the path of the incident beam ("t_i" in the notation of Appendix A). It can be easily shown that if the radiative corrections are linear:

$$ {\rm RCOR}_{\frac{\Delta t_{Al}}{\alpha}} = {\rm RCOR}_0(1 + a\frac{\Delta t_{Al}}{\alpha}) \qquad (C.12) $$

where a is a constant, then:

$$ \begin{aligned} {\rm RC}(\alpha) &= \alpha {\rm RCOR}_0(1 + a\frac{\Delta t_{Al}}{\alpha}) + (1-\alpha){\rm RCOR}_0 \\ &= {\rm RCOR}_0(1 + a\Delta t_{Al}) \end{aligned} \qquad (C.13) $$

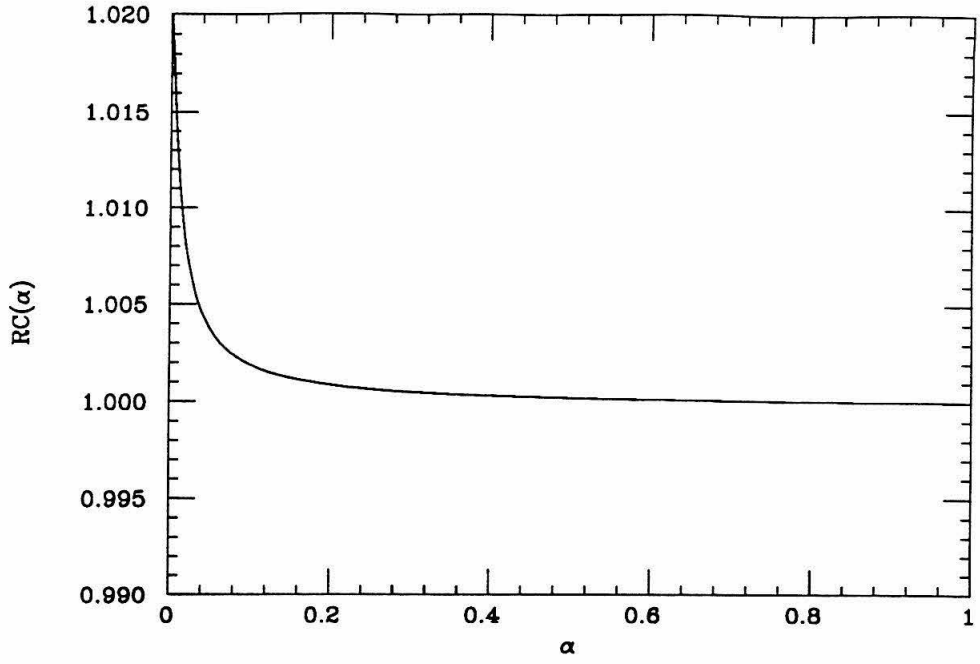

Figure C.3 – A plot of RC(α) vs. α, as defined in the text, normalized at $\alpha = 1$ for a typical set of kinematics and running conditions.

and RC(α) is independent of α. A plot of RC(α) for a typical kinematic setting is shown in Figure C.3.

The fact that RC(α) is nearly independent of α for $\alpha > 0.10$ indicates that the radiative corrections do not depend much on the distribution of the aluminum across the cross sectional area of the beam; in fact, it indicates that the radiative corrections do not depend much on the details of the distribution *along* the beam direction; only the *mean position* of the distribution along the beam affects the radiative corrections. This can be shown by calculating the average radiative correction of a target of length L, cross sectional area A (weighted by the beam distribution), and volume $V = A \times L$,

with a distribution of additional material $\rho(x,y,z)$:

$$\begin{aligned}\langle \mathrm{RCOR} \rangle &= \frac{1}{V}\int_V dx\ dy\ dz \mathrm{RCOR}(x,y,z) \\ &= \frac{1}{V}\int_V dx\ dy\ dz \mathrm{RCOR}_0\Big[1 + a\int_0^z dz'\rho(x,y,z')\Big] \\ &= \mathrm{RCOR}_0\Big[1 + a\frac{1}{V}\int_V dx\ dy\ dz\int_0^L dz'\theta(z-z')\rho(x,y,z')\Big] \\ &= \mathrm{RCOR}_0\Big[1 + a\frac{1}{V}\int_V dx\ dy\ dz'(L-z')\rho(x,y,z')\Big] \qquad (C.14)\end{aligned}$$

which is only a function of the total amount of additional material and its mean position along the (average) beam path.

The wire chamber tracking information not only measured the $\Delta P/P_0$, $\Delta\theta$ and $\Delta\phi$ values of a particular track, but also the horizontal (in plane) position of the particle at the spectrometer entrance, X_{SP8}. This quantity is related to the position along the beamline that the track originated from by Z_{tgt}=$X_{\mathrm{SP8}}/\sin(\theta)$. It was assumed that the track originated along the beamline, Y_{tgt}=0. The measurement of the mean Z value of the distribution, $\langle Z\rangle_{SE}$, of the super-elastic events was a measurement of the mean position of the aluminum in the target. A typical spectrum of Z_{tgt} is shown in Figure C.4. Systematic offsets in this quantity can be caused by an offset in the target position on the pivot, a rotation in the wire chambers ($X_{\mathrm{SP8}} \propto x_{wc} - dx_{wc}$), and errors in the transport coefficients. A similar measurement of the $\langle Z\rangle_{EL}$ of the events in the elastic region was dominated by the scattering from the hydrogen, and was sensitive to identical systematic effects. The difference between these two quantities, $\Delta Z = \langle Z\rangle_{SE} - \langle Z\rangle_{EL} \approx \langle Z\rangle_{Al} - \langle Z\rangle_{H2}$ measured the shift of the mean of the aluminum distribution relative to the hydrogen distribution. Systematic effects with

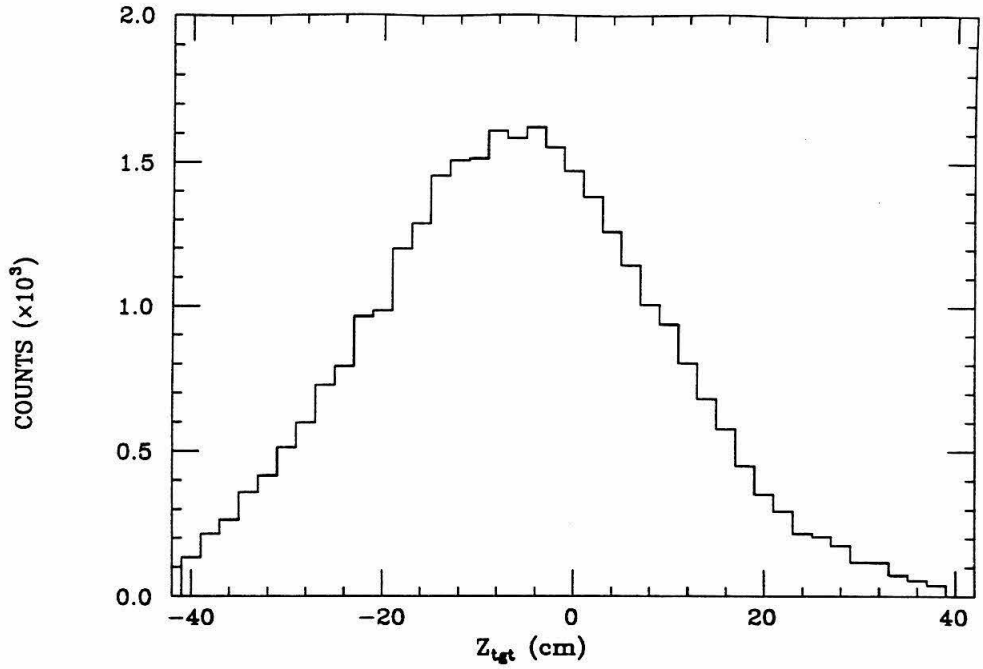

Figure C.4 – A typical spectrum in $Z_{\mathbf{tgt}}$.

regard to the exact placement of the target on the pivot, the orientation of the wire chambers, and the transport coefficients were cancelled.

The super-elastic and elastic kinematic regions occupied different areas of the acceptance. Since the $Z_{\mathbf{tgt}}$ measurement was related to the $x - dx$ track coordinates in the wire chambers, it was possible that acceptance effects correlated with the scattering kinematics (the x and y positions in the wire chambers) could affect the value of ΔZ. The Monte-Carlo program that was used to study the spectrometer acceptance (see Acceptance section) was also used to study this effect. This model has been shown to be a reasonably good approximation to the physical spectrometer acceptance function. The value of $\langle Z \rangle$ was computed as a function of $\Delta P/P_0$ and $\Delta\theta$. This calculation indicated a typical difference between the $\langle Z \rangle$ in the super-elastic

region and the elastic region of $\approx$ 1 cm due to acceptance effects. Corrections were made to the measured $\langle Z \rangle_{SE}$ and $\langle Z \rangle_{EL}$ based on this calculation. A check of this correction was done using the dummy target, and will be discussed below.

Figure C.5(a) shows the values of ΔZ measured with the LH2 target as a function of time (for $t \leq 39$ days, before the flow was corrected). The average offset was 1.8 ± 0.4 cm, (χ^2/dof=1.1). Since the scattering from the DUM target in both the elastic and super-elastic region was from the same material, no such offset should be observed with this target. An identical analysis of the DUM target gave an average offset of 0.8 ± 0.7 (χ^2/dof=0.6), which was consistent with zero, indicating that systematic effects were well controlled. Without the Monte-Carlo based corrections for the acceptance effects, the measured offset with the DUM target was 1.5 ± 0.7. This indicated a good reliability to the Monte-Carlo.

The super-elastic events were scattered from the endcaps, which were centered on the target, and the flow guides, which caused the ΔZ displacement. The average value of the dummy factor was 4.43 while the hydrogen flow was reversed, indicating that on average 23% of the super-elastic scattering was from the endcaps, and 77% of the scattering was from the flow guides. The offset of the Al flow guide distribution was thus taken to be $1.29 \times (1.8 \pm 0.4) = 2.3 \pm 0.5$ cm from the center of the target.

A model of the aluminum distribution of the flow guides was developed that had both the correct amount of material and the proper mean position along the beamline. The aluminum was presumed to be uniformly distributed across the beam cross section. The density was scaled for each run to achieve the proper normalization of material to account for the measured dummy factor. It was also assumed that the aluminum was uniformly distributed along the beamline from $Z = -5.4$ cm to $Z = +10$ cm, where $Z = 0$ cm was defined as the center of the target and therefore the

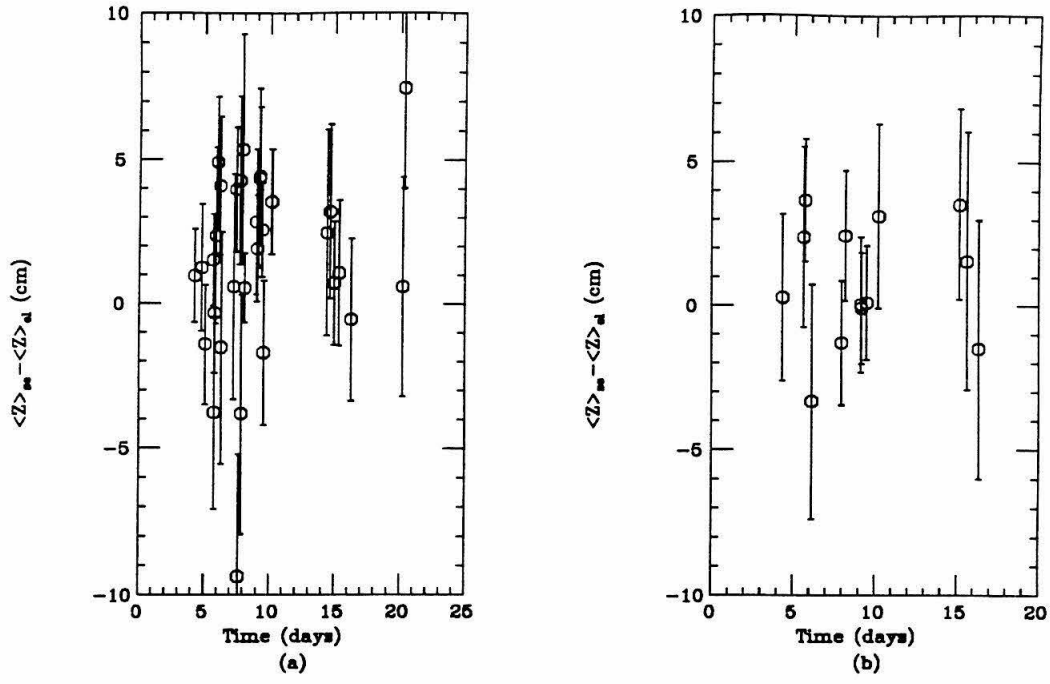

Figure C.5 – Measured values of ΔZ as a function of time. (a) With the LH2 target. (b) With the DUM target.

center of the hydrogen distribution. This model had the proper amount of aluminum with the proper $\langle Z \rangle_{Al}$ value and, due to the high linearity of the radiative corrections, properly incorporated the radiative effects of the flow guides to $\pm 0.2\%$.

C.4 Subtraction and Uncertainty Analysis

The final cross section was defined by:

$$\frac{d\sigma}{d\Omega} = \left[\frac{d\sigma}{d\Omega}^{LH2}_{raw} - \mathrm{DF}\left(\frac{t_{Al}^{H2}}{t_{Al}^{DUM}}\right)\left(\frac{d\sigma}{d\Omega}^{DUM}_{raw}\right)\right] \times \frac{1}{RCOR} \qquad (C.15)$$

Corrections for the aluminum background subtraction were typically $3.0 \pm 0.3\%$ under reversed flow conditions, and were $0.7 \pm 0.1\%$ after the hydrogen flow had been restored. The final cross sections had three sources of statistical uncertainty: the

elastic cross section of the LH2 target, the cross section in the elastic region measured with the dummy target, and the measured normalization factor. The first two contributions could be handled in a straightforward fashion. However, the third contribution (ΔDF) had to be treated more carefully because the additional aluminum in the beam path caused the cross section to both *increase*, due to direct scattering effects, and *decrease*, due to indirect radiative effects, causing a systematic correlation that reduced the sensitivity of the cross section to the value of DF. This effect can be included by expressing the uncertainty in the final cross section in the form:

$$\left[\Delta\frac{d\sigma}{d\Omega}\right]^2 = \left[\Delta\frac{d\sigma}{d\Omega}^{LH2}_{raw}\right]^2 + \left[\mathrm{DF}\frac{t^{H2}_{Al}}{t^{DUM}_{Al}}\Delta\frac{d\sigma}{d\Omega}^{DUM}_{raw}\right]^2 + \left[\beta\frac{t^{H2}_{Al}}{t^{DUM}_{Al}}\frac{d\sigma}{d\Omega}^{DUM}_{raw}\Delta\mathrm{DF}\right]^2 \times \left(\frac{1}{RCOR}\right)^2 \qquad (C.16)$$

where β is a parameter that includes the negative correlation effects.

From the measured aluminum background and the expressions for the radiative corrections given in Appendix A, the value of β can be derived. The direct statistical contribution of ΔDF to the elastic cross section can be expressed by:

$$\left(\Delta\frac{d\sigma}{d\Omega}\Big/\frac{d\sigma}{d\Omega}\right) =\approx (\Delta\mathrm{DF})\frac{t^{H2}_{Al}}{t^{DUM}_{Al}}\left(\frac{d\sigma}{d\Omega}^{DUM}_{raw}\Big/\frac{d\sigma}{d\Omega}\right) \equiv (\Delta\mathrm{DF})\alpha_1 \qquad (C.17)$$

The radiative contribution of ΔDF to the uncertainty was estimated to be:

$$\left(\Delta\frac{d\sigma}{d\Omega}\Big/\frac{d\sigma}{d\Omega}\right) = (\Delta\mathrm{DF})b\ln\left(\frac{R\Delta E}{E_0}\right) \equiv (\Delta\mathrm{DF})\alpha_2 \qquad (C.18)$$

where the notation and variables are defined in Appendix A, with $b \approx 4/3$ and $R \approx (E_0/E')^2$. The parameter β was then defined by:

$$\beta = \frac{\alpha_1 + \alpha_2}{\alpha_1} \qquad (C.19)$$

which related the effect of ΔDF on the cross section uncertainty relative to the statistical effect alone. The value of β ranged from $0 < |\beta| < 0.90$, depending on the kinematics, etc. It was artificially limited to $0.25 < |\beta|$ to provide a safely conservative estimate of the uncertainty caused by the measured dummy factor when the two effects nearly cancelled.

Other systematic errors were included in the aluminum background subtraction. These were caused by the uncertainty in the amount of material the electrons passed through as they exited the target through the flow guides, and the variation of $\langle Z \rangle_{AL}$ from run to run. The direction of the hydrogen flow and the geometry of the flow guides limited the uncertainty in the outgoing electron path to be the thickness of the flow guides, which was 0.00254 cm. This had a $\pm 0.1\%$ effect on the cross sections. An uncertainty analysis of the $\langle Z \rangle$ fits described previously limited the typical fluctuations of ΔZ to ± 0.5 cm, which had a $\pm 0.15\%$ effect on the cross sections.

Appendix D
Data Tables

D.1 Data From This Experiment

E_0 GeV	θ_0 deg	W^2_{cut} $(GeV/c)^2$	$\langle t_i \rangle$ %	$\langle t_f \rangle$ %	δ_{int}	δ'_{int}	$\langle \delta_{ext} \rangle$	RCOR
1.5938	45.5074	0.9730	1.54	1.54	-0.1637	0.0179	-0.1147	0.7710
2.4033	27.5635	1.0104	1.54	1.79	-0.1680	0.0175	-0.1307	0.7551
3.2375	19.7400	1.0498	1.54	2.06	-0.1699	0.0172	-0.1442	0.7435
2.4076	46.6752	1.0134	1.54	1.53	0.1769	0.0244	-0.1100	0.7694
2.8002	37.7562	1.0359	1.54	1.63	0.1763	0.0242	-0.1161	0.7650
3.2501	31.0965	1.0571	1.54	1.75	-0.1777	0.0237	-0.1233	0.7581
4.0030	24.1089	1.0980	1.54	1.90	-0.1773	0.0234	-0.1313	0.7522
5.4894	16.7996	1.1095	1.33	2.16	-0.1961	0.0212	-0.1500	0.7228
6.2371	14.6021	1.1061	1.33	2.27	-0.2062	0.0203	-0.1625	0.7061
6.9806	12.9317	1.1024	1.54	2.36	-0.2154	0.0197	-0.1831	0.6850
7.4876	12.0007	1.1021	1.54	2.40	-0.2204	0.0193	-0.1895	0.6771
2.7962	46.2336	1.0352	1.54	1.53	-0.1799	0.0271	-0.1079	0.7708
3.2413	37.3101	1.0741	1.54	1.63	-0.1738	0.0275	-0.1104	0.7739
3.7662	30.5311	1.0881	1.43	1.74	-0.1798	0.0261	-0.1173	0.7628
4.2416	26.2759	1.1107	1.54	1.85	-0.1808	0.0257	-0.1273	0.7542
7.0542	14.5725	1.1015	1.54	2.27	-0.2209	0.0213	-0.1786	0.6854
8.2093	12.3574	1.1026	1.33	2.38	-0.2314	0.0206	-0.1831	0.6749
3.2513	44.2630	1.0621	1.54	1.57	-0.1818	0.0295	-0.1073	0.7716
4.0082	32.7090	1.1063	1.54	1.70	-0.1810	0.0287	-0.1156	0.7652
6.2460	18.8138	1.1068	1.54	2.08	-0.2142	0.0238	-0.1596	0.7050
7.0743	16.3060	1.1038	1.54	2.17	-0.2243	0.0228	-0.1721	0.6886
8.2334	13.7628	1.1065	1.33	2.29	-0.2344	0.0221	-0.1768	0.6780

Table D.1 – Radiative correction values calculated for the kinematics of this experiment. The number of radiation lengths before and after the scattering (t_i and t_f) are approximated in this table because the aluminum normalization parameter (DF) fluctuated from run to run, and each kinematic setting frequently contained many runs (see Appendix C).

Q^2	ε	E_0	E'	θ	$\frac{d\sigma}{d\Omega}$	$\Delta\frac{d\sigma}{d\Omega}$
1.000	0.692	1.594	1.061	45.221	5.253E+0	4.179E-2
1.000	0.869	2.403	1.871	27.277	1.780E+1	1.618E-1
1.000	0.930	3.238	2.705	19.454	3.950E+1	3.391E-1
2.003	0.635	2.408	1.340	46.389	4.432E-1	4.070E-3
2.003	0.735	2.800	1.733	37.470	7.795E-1	5.871E-3
2.003	0.808	3.250	2.183	30.810	1.288E+0	7.869E-3
2.003	0.878	4.003	2.936	23.822	2.422E+0	2.315E-2
2.003	0.938	5.489	4.422	16.513	5.747E+0	1.365E-1
2.003	0.953	6.237	5.170	14.316	8.284E+0	8.403E-2
2.003	0.963	6.981	5.913	12.645	1.109E+1	1.054E-1
2.003	0.968	7.488	6.420	11.714	1.312E+1	3.676E-1
2.497	0.619	2.796	1.466	45.947	1.893E-1	1.719E-3
2.497	0.723	3.241	1.911	37.024	3.369E-1	2.875E-3
2.497	0.800	3.766	2.436	30.245	5.629E-1	3.569E-3
2.497	0.846	4.242	2.911	25.989	8.295E-1	7.724E-3
2.497	0.949	7.054	5.724	14.286	3.612E+0	2.736E-2
2.497	0.963	8.209	6.879	12.071	5.433E+0	9.714E-2
3.007	0.623	3.251	1.649	43.976	9.661E-2	9.355E-4
3.007	0.761	4.008	2.406	32.422	2.195E-1	1.876E-3
3.007	0.910	6.246	4.644	18.527	9.087E-1	2.316E-2
3.007	0.932	7.074	5.472	16.020	1.316E+0	1.376E-2
3.007	0.951	8.233	6.631	13.476	2.013E+0	4.797E-2

Table D.2 – Cross section values at each kinematic point used to extract the form factors.

Time (Days)	Q^2 $(GeV/c)^2$	ϵ	N_{elec} $\times 10^3$	DF	ΔDF
4.25	1.001	0.930	17.260	4.91	0.52
4.79	2.501	0.723	5.688	4.83	1.00
5.00	2.501	0.723	2.650	5.09	1.29
5.08	2.501	0.723	7.117	5.46	1.06
5.67	2.000	0.808	13.635	4.00	0.51
5.75	2.000	0.808	4.329	3.91	0.71
5.79	1.999	0.808	11.026	3.96	0.53
5.88	3.001	0.623	3.372	5.88	1.61
5.96	3.001	0.623	4.012	7.13	1.80
6.17	3.003	0.623	3.235	6.54	1.77
6.29	3.002	0.623	2.068	5.51	1.78
6.79	2.497	0.619	0.368	3.36	2.40
7.13	2.495	0.620	0.878	6.01	2.11
7.25	2.495	0.620	0.982	8.81	2.51
7.33	2.493	0.620	0.182	15.03	7.01
7.42	2.497	0.619	3.051	6.92	1.42
7.63	2.498	0.619	1.500	3.85	1.33
7.71	2.495	0.620	3.200	5.95	1.25
7.83	2.498	0.619	0.755	4.71	2.04
7.88	2.497	0.619	2.138	3.74	1.10
8.08	2.001	0.735	20.904	5.35	0.73
8.96	1.998	0.634	6.916	7.23	1.32
9.04	1.996	0.635	6.772	6.22	1.17
9.17	1.000	0.869	6.184	4.06	0.69
9.21	0.999	0.869	6.751	4.85	0.75
9.42	0.999	0.692	17.433	5.54	0.80
10.13	2.504	0.797	13.048	5.84	0.70
14.33	3.004	0.761	0.293	7.87	3.41
14.38	3.005	0.761	1.522	3.96	1.13
14.50	3.007	0.761	0.348	3.65	2.15
14.54	3.008	0.761	1.728	3.21	0.95
14.63	3.008	0.761	0.424	3.80	1.92
14.63	3.008	0.761	0.566	3.36	1.55
14.96	3.007	0.761	9.945	3.62	0.58
15.33	2.004	0.878	12.461	4.01	0.59
16.25	2.503	0.846	13.334	4.36	0.64
24.25	2.007	0.968	0.867	4.58	1.31
24.29	2.009	0.968	0.495	3.14	1.32
26.38	2.010	0.963	6.058	4.89	0.78
26.42	2.010	0.963	7.205	5.28	0.80
37.17	3.011	0.932	1.334	5.49	1.15
37.29	3.010	0.932	4.044	4.09	0.65
37.42	3.011	0.932	0.681	3.73	1.23
37.42	3.013	0.932	0.056	11.25	6.60
37.46	3.010	0.932	1.794	3.02	0.70
37.54	3.009	0.932	2.045	4.17	0.82
37.58	2.509	0.949	10.424	4.58	0.63
37.63	2.508	0.949	0.496	6.27	2.03
37.63	2.509	0.949	2.108	5.36	1.07
37.67	2.509	0.949	3.504	4.43	0.78
37.67	2.506	0.949	1.281	5.27	1.22
37.67	2.511	0.949	1.821	3.82	0.89
38.96	3.008	0.910	1.755	3.68	1.02

Table D.3 – Aluminum normalization factor (DF) for each of the elastic data runs included in the analysis before the hydrogen flow direction was corrected.

Time (Days)	Q^2 $(GeV/c)^2$	ϵ	N_{elec} $\times 10^3$	DF	ΔDF
39.00	2.008	0.953	2.879	1.81	0.45
43.63	2.502	0.797	6.487	1.68	0.39
45.25	2.008	0.953	7.162	0.86	0.20
46.96	2.007	0.938	0.501	1.71	1.07
47.00	2.009	0.938	1.385	1.63	0.70
60.33	3.014	0.951	1.917	2.17	0.83
60.42	2.514	0.963	3.241	1.75	0.42
68.38	2.423	0.808	7.360	1.63	0.36

Table D.4 – Aluminum normalization factor (DF) for each of the elastic data runs included in the analysis after the hydrogen flow direction was corrected.

D.2 Data From Other Experiments (World Fit)

Q^2 (GeV/c)^2	Q^2 (fm)$^{-2}$	E_0 GeV	E' GeV	θ deg	ε	$\frac{d\sigma}{d\Omega}$ nb/sr	$\Delta\frac{d\sigma}{d\Omega}$ nb/sr	$\Delta\frac{d\sigma}{d\Omega}$ %
0.1558	4.00	0.5590	0.4760	45.000	0.7362	3.5720E+02	1.3931E+01	3.9
0.1555	3.99	0.3680	0.2851	75.000	0.4485	9.9500E+01	3.9800E+00	4.0
0.1557	4.00	0.2590	0.1760	135.000	0.0759	2.2700E+01	8.8530E-01	3.9
0.1792	4.60	0.6030	0.5075	45.000	0.7350	2.6950E+02	1.1049E+01	4.1
0.1794	4.61	0.4740	0.3784	60.000	0.5880	1.3020E+02	5.8590E+00	4.5
0.1794	4.61	0.3990	0.3034	75.000	0.4469	7.7000E+01	3.0800E+00	4.0
0.1793	4.61	0.3510	0.2554	90.000	0.3224	4.8500E+01	2.3765E+00	4.9
0.1794	4.61	0.2970	0.2014	120.000	0.1369	2.4200E+01	1.2100E+00	5.0
0.1794	4.61	0.2820	0.1864	135.000	0.0755	1.9800E+01	7.9200E-01	4.0
0.1795	4.61	0.2750	0.1794	145.000	0.0452	1.6950E+01	6.7800E-01	4.0
0.1947	5.00	0.6900	0.5863	40.590	0.7760	2.9572E+02	1.4490E+01	4.9
0.1947	5.00	0.4180	0.3142	75.000	0.4459	7.3610E+01	3.6805E+00	5.0
0.1944	4.99	0.2960	0.1924	135.000	0.0752	1.8440E+01	9.2200E-01	5.0
0.2336	6.00	0.6900	0.5655	45.520	0.7271	1.7714E+02	8.8570E+00	5.0
0.2339	6.01	0.5500	0.4253	60.000	0.5845	8.6020E+01	3.5268E+00	4.1
0.2335	6.00	0.4640	0.3395	75.000	0.4433	4.9320E+01	2.5153E+00	5.1
0.2335	6.00	0.3310	0.2066	135.000	0.0745	1.2900E+01	5.1600E-01	4.0
0.2728	7.01	0.6000	0.4546	60.000	0.5820	6.4220E+01	2.6330E+00	4.1
0.2730	7.01	0.5080	0.3625	75.000	0.4408	3.7520E+01	1.5008E+00	4.0
0.2725	7.00	0.4340	0.2888	95.000	0.2804	1.9280E+01	9.6400E-01	5.0
0.2721	6.99	0.3640	0.2190	135.000	0.0738	9.7200E+00	3.8880E-01	4.0
0.2728	7.01	0.3560	0.2106	145.000	0.0441	9.1100E+00	4.5550E-01	5.0
0.2922	7.50	0.6240	0.4683	60.000	0.5807	5.5800E+01	2.2878E+00	4.1
0.2916	7.49	0.5280	0.3726	75.000	0.4396	3.2410E+01	1.3288E+00	4.1
0.2923	7.51	0.4680	0.3123	90.000	0.3159	2.0650E+01	1.0532E+00	5.1
0.2916	7.49	0.3990	0.2436	120.000	0.1334	1.0580E+01	5.2900E-01	5.0
0.2915	7.49	0.3800	0.2247	135.000	0.0734	8.8500E+00	3.5400E-01	4.0
0.3115	8.00	0.6900	0.5240	55.300	0.6260	5.6370E+01	2.8185E+00	5.0
0.3113	7.99	0.6470	0.4811	60.000	0.5795	4.6820E+01	2.3410E+00	5.0
0.3116	8.00	0.5490	0.3829	75.000	0.4383	2.8050E+01	1.0940E+00	3.9
0.3112	7.99	0.3960	0.2302	135.000	0.0731	7.7900E+00	3.1160E-01	4.0
0.3113	8.00	0.3870	0.2211	145.000	0.0437	7.4500E+00	3.7250E-01	5.0
0.3498	8.98	0.6920	0.5056	60.000	0.5771	3.7120E+01	1.8931E+00	5.1
0.3500	8.99	0.5880	0.4015	75.000	0.4358	2.2240E+01	8.8960E-01	4.0
0.3503	9.00	0.4270	0.2403	135.000	0.0724	6.4900E+00	2.5960E-01	4.0
0.3894	10.00	0.9000	0.6925	46.560	0.7086	5.9430E+01	2.9121E+00	4.9
0.3891	9.99	0.7360	0.5287	60.000	0.5746	3.0820E+01	1.2328E+00	4.0
0.3897	10.01	0.6270	0.4193	75.000	0.4333	1.7800E+01	7.2980E-01	4.1
0.3894	10.00	0.5570	0.3495	90.000	0.3105	1.1890E+01	5.8261E-01	4.9
0.3898	10.01	0.4790	0.2713	120.000	0.1305	6.2700E+00	3.1350E-01	5.0
0.3893	10.00	0.4570	0.2495	135.000	0.0717	5.1500E+00	2.0600E-01	4.0
0.3894	10.00	0.4470	0.2395	145.000	0.0428	4.7300E+00	2.3650E-01	5.0
0.4282	11.00	0.9500	0.7218	46.550	0.7067	4.8330E+01	2.4165E+00	5.0
0.4287	11.01	0.6640	0.4356	75.000	0.4309	1.4510E+01	7.1099E-01	4.9
0.4280	10.99	0.4860	0.2579	135.000	0.0711	4.3500E+00	1.7400E-01	4.0
0.4671	12.00	0.9500	0.7011	49.510	0.6749	3.3410E+01	1.7039E+00	5.1
0.4672	12.00	0.9000	0.6510	53.040	0.6393	2.7780E+01	1.3890E+00	5.0
0.4677	12.01	0.7000	0.4508	75.000	0.4285	1.1780E+01	4.7120E-01	4.0
0.4675	12.01	0.5150	0.2659	[illegible].000	0.0704	3.5500E+00	1.7750E-01	5.0
0.4674	12.00	0.5040	0.2549	[illegible].000	0.0420	3.2700E+00	1.6350E-01	5.0
0.4865	12.49	0.7170	0.4577	75.000	0.4273	1.0440E+01	4.1760E-01	4.0

Table D.5 – Cross sections and kinematics for $Q^2 \leq 0.5$ (GeV/c)^2 from Janssens, *et al.*, [34].

Q^2 (GeV/c)^2	Q^2 (fm)$^{-2}$	E_0 GeV	E' GeV	θ deg	ϵ	$\frac{d\sigma}{d\Omega}$ nb/sr	$\Delta\frac{d\sigma}{d\Omega}$ nb/sr	$\Delta\frac{d\sigma}{d\Omega}$ %
0.5061	13.00	0.9500	0.6803	52.520	0.6424	2.4420E+01	1.1966E+00	4.9
0.5066	13.01	0.7350	0.4650	75.000	0.4261	9.4100E+00	3.8581E-01	4.1
0.5064	13.00	0.5430	0.2732	135.000	0.0698	2.9000E+00	1.4500E-01	5.0
0.5451	14.00	0.9500	0.6595	55.600	0.6090	1.8330E+01	9.1650E-01	5.0
0.5452	14.00	0.9000	0.6095	59.800	0.5670	1.4290E+01	7.4308E-01	5.2
0.5453	14.00	0.7690	0.4784	75.000	0.4238	7.8700E+00	3.2267E-01	4.1
0.5445	13.98	0.5700	0.2798	135.000	0.0692	2.4700E+00	1.2350E-01	5.0
0.5456	14.01	0.5590	0.2683	145.000	0.0413	2.3700E+00	1.1850E-01	5.0
0.5840	15.00	0.9500	0.6388	58.750	0.5751	1.3370E+01	6.5513E-01	4.9
0.5837	14.99	0.8020	0.4910	75.000	0.4215	6.6400E+00	3.3864E-01	5.1
0.5833	14.98	0.5970	0.2862	135.000	0.0686	2.1400E+00	1.0700E-01	5.0
0.6230	16.00	0.9500	0.6180	62.000	0.5406	9.2800E+00	4.6400E-01	5.0
0.6229	16.00	0.9000	0.5680	67.000	0.4923	7.7100E+00	3.9321E-01	5.1
0.6228	15.99	0.8350	0.5031	75.000	0.4192	5.5400E+00	2.6592E-01	4.8
0.6230	16.00	0.8020	0.4700	80.000	0.3763	5.1600E+00	2.5800E-01	5.0
0.6226	15.99	0.6240	0.2922	135.000	0.0680	1.7800E+00	8.9000E-02	5.0
0.6232	16.01	0.6120	0.2799	145.000	0.0405	1.6400E+00	8.2000E-02	5.0
0.6618	16.99	0.9500	0.5974	65.360	0.5057	7.1600E+00	3.5800E-01	5.0
0.6613	16.98	0.8670	0.5146	75.000	0.4169	4.9800E+00	2.4402E-01	4.9
0.6624	17.01	0.6510	0.2980	135.000	0.0674	1.6300E+00	8.1500E-02	5.0
0.6809	17.49	0.8830	0.5202	75.000	0.4158	4.7900E+00	1.9639E-01	4.1
0.7009	18.00	0.9500	0.5765	68.890	0.4699	5.6500E+00	2.7685E-01	4.9
0.7005	17.99	0.8990	0.5257	75.000	0.4146	4.4400E+00	2.2200E-01	5.0
0.7006	17.99	0.8640	0.4907	80.000	0.3720	3.6400E+00	1.7472E-01	4.8
0.7012	18.01	0.6770	0.3034	135.000	0.0668	1.2900E+00	6.4500E-02	5.0
0.7013	18.01	0.6640	0.2903	145.000	0.0398	1.1900E+00	5.9500E-02	5.0
0.7398	19.00	0.9500	0.5558	72.580	0.4339	4.1600E+00	2.1216E-01	5.1
0.7391	18.98	0.9300	0.5361	75.000	0.4124	4.1500E+00	2.5315E-01	6.1
0.7404	19.01	0.7030	0.3085	135.000	0.0662	1.1800E+00	5.9000E-02	5.0
0.7782	19.99	0.9610	0.5463	75.000	0.4102	3.4900E+00	1.7450E-01	5.0
0.7787	20.00	0.9500	0.5350	76.470	0.3974	3.4000E+00	1.6320E-01	4.8
0.7792	20.01	0.9250	0.5097	80.000	0.3677	2.5900E+00	1.1396E-01	4.4
0.7787	20.00	0.9000	0.4850	83.800	0.3371	2.3200E+00	1.1600E-01	5.0
0.7784	19.99	0.7280	0.3132	135.000	0.0657	1.1500E+00	5.7500E-02	5.0
0.7795	20.02	0.7150	0.2996	145.000	0.0391	9.0300E-01	4.5150E-02	5.0
0.8567	22.00	1.0220	0.5655	75.000	0.4058	2.8190E+00	1.3813E-01	4.9
0.8567	22.00	0.9500	0.4935	85.050	0.3235	1.8250E+00	1.0950E-01	6.0
0.8571	22.01	0.7790	0.3223	135.000	0.0645	8.8200E-01	4.4100E-02	5.0
0.8559	21.98	0.7640	0.3079	145.000	0.0385	7.7700E-01	3.8850E-02	5.0
1.0120	25.99	0.8620	0.3227	145.000	0.0372	4.3200E-01	2.3328E-02	5.4
1.0899	27.99	0.9100	0.3292	145.000	0.0366	3.2500E-01	2.2750E-02	7.0
1.1686	30.01	0.9580	0.3353	145.000	0.0360	2.4900E-01	1.9920E-02	8.0

Table D.6 – Cross sections and kinematics for $Q^2 \geq 0.5$ (GeV/c)^2 from Janssens, *et al.*, from reference [34].

Q^2 (GeV/c)^2	Q^2 (fm)$^{-2}$	E_0 GeV	E' GeV	θ deg	ϵ	$\frac{d\sigma}{d\Omega}$ nb/sr	$\Delta\frac{d\sigma}{d\Omega}$ nb/sr	$\Delta\frac{d\sigma}{d\Omega}$ %
0.3894	10.00	3.6850	3.4775	10.000	0.9833	1.7600E+03	5.2800E+01	3.0
0.7788	20.00	5.2740	4.8590	10.001	0.9816	3.3900E+02	1.0170E+01	3.0
0.7788	20.00	4.4330	4.0180	12.003	0.9737	2.2760E+02	6.8280E+00	3.0
0.7788	20.00	3.6400	3.2250	14.799	0.9604	1.4620E+02	4.3860E+00	3.0
1.1682	30.00	5.9070	5.2845	11.101	0.9755	8.7500E+01	2.6250E+00	3.0
1.1682	30.00	4.4360	3.8135	15.100	0.9553	4.3700E+01	1.3110E+00	3.0
1.5575	40.00	5.2780	4.4480	14.799	0.9536	1.8000E+01	5.4000E-01	3.0
1.7522	45.00	5.2450	4.3113	16.002	0.9441	1.0240E+01	3.0720E-01	3.0
1.9469	50.00	5.8880	4.8505	15.003	0.9489	8.1300E+00	2.4390E-01	3.0
2.9204	75.00	5.8830	4.3268	19.502	0.9025	9.5200E-01	3.8080E-02	4.0
4.0886	105.00	5.8860	3.7073	24.999	0.8248	1.1300E-01	5.6500E-03	5.0

Table D.7 – Cross sections and kinematics from Bartel, 1966, *et al.*, from reference [37]

Q^2 (GeV/c)^2	Q^2 (fm)$^{-2}$	E_0 GeV	E' GeV	θ deg	ϵ	$\frac{d\sigma}{d\Omega}$ nb/sr	$\Delta\frac{d\sigma}{d\Omega}$ nb/sr	$\Delta\frac{d\sigma}{d\Omega}$ %
1.9469	50.00	1.7666	0.7291	75.870	0.3464	1.4100E-01	6.0630E-03	4.3
2.9204	75.00	2.3716	0.8153	75.830	0.3106	2.7600E-02	1.1868E-03	4.3
9.5594	245.50	6.1281	1.0340	75.780	0.1819	6.0400E-05	8.5164E-06	14.1

Table D.8 – Cross sections and kinematics from Albrecht, *et al.*, from reference [4]

Q^2 (GeV/c)^2	Q^2 (fm)$^{-2}$	E_0 GeV	E' GeV	θ deg	ϵ	$\frac{d\sigma}{d\Omega}$ nb/sr	$\Delta\frac{d\sigma}{d\Omega}$ nb/sr	$\Delta\frac{d\sigma}{d\Omega}$ %
0.9990	25.66	3.9960	3.4636	15.440	0.9549	6.5930E+01	9.2000E-01	1.4
0.9988	25.65	3.2960	2.7638	19.060	0.9325	4.0650E+01	6.1000E-01	1.5
0.9987	25.65	2.9980	2.4658	21.180	0.9177	3.3080E+01	5.1000E-01	1.5
1.4987	38.49	6.1970	5.3984	12.150	0.9687	3.3070E+01	4.9000E-01	1.5
1.4989	38.49	3.2960	2.4973	24.640	0.8803	6.3500E+00	1.1000E-01	1.7
1.4985	38.48	2.9980	2.1994	27.580	0.8534	4.8180E+00	7.5000E-02	1.6
1.9983	51.32	6.1970	5.1321	14.400	0.9524	8.3000E+00	1.4000E-01	1.7
1.9985	51.33	3.9960	2.9310	23.840	0.8774	2.4140E+00	3.9000E-02	1.6
1.9986	51.33	3.2960	2.2310	30.220	0.8140	1.3340E+00	3.2000E-02	2.4
1.9977	51.30	2.9980	1.9334	34.140	0.7719	9.9900E-01	1.7000E-02	1.7
2.5011	64.23	7.9090	6.5762	12.590	0.9600	4.7080E+00	6.7000E-02	1.4
2.5047	64.32	5.2530	3.9183	20.090	0.9030	1.5380E+00	2.6000E-02	1.7
2.5061	64.36	3.8020	2.4665	29.960	0.8032	5.6500E-01	1.0000E-02	1.8
2.4969	64.12	3.2940	1.9634	36.200	0.7325	3.5320E-01	6.5000E-03	1.8
2.5011	64.23	7.9090	6.5762	12.590	0.9600	4.7770E+00	6.6000E-02	1.4
2.4983	64.16	6.1970	4.8657	16.550	0.9326	2.5660E+00	5.2000E-02	2.0
2.4992	64.18	3.9960	2.6642	28.040	0.8243	6.8800E-01	1.2000E-02	1.7
2.4969	64.12	3.2960	1.9654	36.170	0.7329	3.4750E-01	6.5000E-03	1.9
2.4977	64.14	2.9980	1.6670	41.400	0.6720	2.4690E-01	4.5000E-03	1.8
3.7447	96.17	9.9980	8.0025	12.420	0.9534	9.7300E-01	1.4000E-02	1.4
3.7438	96.15	7.9110	5.9159	16.260	0.9223	5.1120E-01	8.9000E-03	1.7
3.7452	96.18	3.9960	2.0002	40.030	0.6462	4.7100E-02	9.2000E-04	2.0

Table D.9 – Cross sections and kinematics from Litt, *et al.*, from reference [40]

Q^2 $(\mathrm{GeV/c})^2$	Q^2 $(\mathrm{fm})^{-2}$	E_0 GeV	E' GeV	θ deg	ϵ	$\frac{d\sigma}{d\Omega}$ nb/sr	$\Delta\frac{d\sigma}{d\Omega}$ nb/sr	$\Delta\frac{d\sigma}{d\Omega}$ %
0.2726	7.00	1.5777	1.4324	20.000	0.9372	7.6750E+02	1.6118E+01	2.1
0.3894	10.00	1.9035	1.6960	20.000	0.9354	4.1190E+02	9.0618E+00	2.2
0.5841	15.00	2.3617	2.0505	20.000	0.9324	1.5640E+02	4.0664E+00	2.6
0.7788	20.00	2.7570	2.3420	20.000	0.9294	7.5950E+01	1.7469E+00	2.3
1.1682	30.00	3.4389	2.8164	20.000	0.9235	2.3980E+01	1.0791E+00	4.5
1.1682	30.00	3.4389	2.8164	20.000	0.9235	2.3040E+01	6.6816E-01	2.9
1.7522	45.00	4.3069	3.3732	20.000	0.9148	6.0560E+00	2.7858E-01	4.6
1.7522	45.00	4.3069	3.3732	20.000	0.9148	5.7920E+00	1.9114E-01	3.3
2.7257	70.00	5.5000	4.0475	20.153	0.8993	1.2090E+00	6.2868E-02	5.2
2.9204	75.00	6.0000	4.4438	19.050	0.9066	9.5800E-01	7.7598E-02	8.1
3.5045	90.00	6.0000	4.1325	21.670	0.8725	3.6400E-01	1.6744E-02	4.6
3.8939	100.00	5.5000	3.4250	26.280	0.8133	1.3500E-01	7.5600E-03	5.6
4.4779	115.00	6.0000	3.6138	26.268	0.8017	7.2500E-02	4.0600E-03	5.6
5.0620	130.00	6.0000	3.3025	29.277	0.7504	2.9800E-02	2.0562E-03	6.9
5.8408	150.00	6.0000	2.8875	33.754	0.6714	1.0400E-02	9.9840E-04	9.6

Table D.10 – Cross sections and kinematics from Goitein, *et al.*, from reference [42]

Q^2 $(\mathrm{GeV/c})^2$	Q^2 $(\mathrm{fm})^{-2}$	E_0 GeV	E' GeV	θ deg	ϵ	$\frac{d\sigma}{d\Omega}$ nb/sr	$\Delta\frac{d\sigma}{d\Omega}$ nb/sr	$\Delta\frac{d\sigma}{d\Omega}$ %
0.0780	2.00	0.6600	0.6184	25.250	0.9070	3.2800E+03	9.9000E+01	3.0
0.1172	3.01	0.8150	0.7525	25.250	0.9061	1.8570E+03	5.5000E+01	3.0
0.1194	3.07	0.6050	0.5414	35.150	0.8282	8.6300E+02	2.6000E+01	3.0
0.1952	5.01	1.0640	0.9600	25.250	0.9042	8.4100E+02	2.6000E+01	3.1
0.1945	5.00	0.7840	0.6803	35.150	0.8253	4.0000E+02	1.2000E+01	3.0
0.3122	8.02	1.3640	1.1977	25.250	0.9015	3.6100E+02	9.0000E+00	2.5
0.3903	10.02	1.5370	1.3290	25.250	0.8997	2.2850E+02	4.6000E+00	2.0
0.3891	9.99	1.2490	1.0416	31.740	0.8478	1.3280E+02	2.6000E+00	2.0
0.3892	10.00	1.2310	1.0236	32.270	0.8433	1.3100E+02	2.6000E+00	2.0
0.3892	10.00	1.1420	0.9346	35.150	0.8178	1.0800E+02	2.2000E+00	2.0
0.3890	9.99	0.8480	0.6407	50.060	0.6738	4.6030E+01	9.4000E-01	2.0
0.3895	10.00	0.6960	0.4884	64.720	0.5286	2.5290E+01	4.1000E-01	1.6
0.3894	10.00	0.5560	0.3485	90.270	0.3084	1.1780E+01	2.3000E-01	2.0
0.5072	13.03	1.7700	1.4997	25.250	0.8970	1.2860E+02	2.6000E+00	2.0
0.5847	15.02	1.9120	1.6004	25.250	0.8953	9.0100E+01	1.8000E+00	2.0
0.5842	15.00	1.6290	1.3177	30.240	0.8545	6.1400E+01	1.2000E+00	2.0
0.5844	15.01	1.5400	1.2286	32.270	0.8367	5.1600E+01	1.0000E+00	1.9
0.5841	15.00	1.5220	1.2107	32.700	0.8329	4.9360E+01	9.9000E-01	2.0
0.5843	15.01	1.4310	1.1196	35.150	0.8104	4.2570E+01	8.5000E-01	2.0
0.5788	14.86	1.1710	0.8626	44.480	0.7198	2.4120E+01	4.8000E-01	2.0
0.5840	15.00	1.0720	0.7608	50.060	0.6630	1.7870E+01	3.6000E-01	2.0
0.5843	15.01	1.0420	0.7306	51.960	0.6436	1.6770E+01	3.4000E-01	2.0
0.5844	15.01	0.8920	0.5806	64.170	0.5218	1.0030E+01	2.0000E-01	2.0
0.5837	14.99	0.8860	0.5749	64.720	0.5165	9.7300E+00	2.0000E-01	2.1
0.5845	15.01	0.7180	0.4065	90.080	0.2995	4.5500E+00	1.0000E-01	2.2
0.5844	15.01	0.7170	0.4056	90.270	0.2982	4.5360E+00	9.0000E-02	2.0
0.5846	15.01	0.6470	0.3354	110.300	0.1721	2.9460E+00	6.8000E-02	2.3
0.5834	14.98	0.6450	0.3341	110.720	0.1700	2.9900E+00	6.1000E-02	2.0
0.7790	20.01	1.7890	1.3739	32.700	0.8263	2.3360E+01	4.8000E-01	2.1
0.7784	19.99	1.6830	1.2682	35.150	0.8032	1.9810E+01	5.9000E-01	3.0
0.7791	20.01	1.3920	0.9768	44.480	0.7100	1.1380E+01	2.3000E-01	2.0
0.7791	20.01	1.0640	0.6488	64.170	0.5102	4.5000E+00	1.1000E-01	2.4
0.7792	20.01	0.8650	0.4498	90.080	0.2899	2.1360E+00	4.7000E-02	2.2
0.7783	19.99	0.7840	0.3693	110.130	0.1665	1.3950E+00	3.0000E-02	2.2
0.9729	24.99	1.9130	1.3945	35.150	0.7961	1.0540E+01	2.1000E-01	2.0
0.9737	25.00	1.7180	1.1992	40.210	0.7451	7.8800E+00	1.7000E-01	2.2
0.9739	25.01	1.2240	0.7050	64.170	0.4991	2.4300E+00	5.6000E-02	2.3
0.9731	24.99	1.0030	0.4844	90.080	0.2809	1.1070E+00	2.8000E-02	2.5
0.9740	25.01	0.9150	0.3960	110.130	0.1605	6.9500E-01	2.4000E-02	3.5
1.1683	30.00	1.9100	1.2874	40.320	0.7358	4.4490E+00	1.8000E-01	4.0
1.1679	29.99	1.3750	0.7526	64.170	0.4886	1.4130E+00	3.1000E-02	2.2
1.1667	29.96	1.1350	0.5133	90.080	0.2725	6.1500E-01	1.6000E-02	2.6
1.1678	29.99	1.0400	0.4177	110.130	0.1549	4.1400E-01	2.1000E-02	5.1
1.3631	35.01	1.7900	1.0636	50.060	0.6231	1.4750E+00	4.1000E-02	2.8
1.3621	34.98	1.5120	0.7862	64.720	0.4731	8.1500E-01	2.9000E-02	3.6
1.3626	34.99	1.2630	0.5369	90.270	0.2632	3.6200E-01	1.2000E-02	3.3
1.3626	34.99	1.1600	0.4339	110.720	0.1468	2.3020E-01	8.8000E-03	3.8
1.5576	40.00	1.6610	0.8310	64.170	0.4687	5.4000E-01	2.0000E-02	3.7
1.5571	39.99	1.3890	0.5593	90.130	0.2566	2.2060E-01	9.2000E-03	4.2
1.5576	40.00	1.2820	0.4520	110.130	0.1447	1.4840E-01	5.0000E-03	3.4
1.7527	45.01	1.7890	0.8550	64.720	0.4540	3.2500E-01	1.0000E-02	3.1
1.7524	45.00	1.5110	0.5772	90.270	0.2485	1.5060E-01	6.1000E-03	4.1
1.7522	45.00	1.3970	0.4633	110.720	0.1375	9.1500E-02	5.5000E-03	6.0
1.9461	49.98	1.6320	0.5949	90.130	0.2428	9.2100E-02	4.9000E-03	5.3

Table D.11 – Cross sections and kinematics from Berger, *et al.*, from reference [44]

Q^2 $(\mathrm{GeV/c})^2$	Q^2 $(\mathrm{fm})^{-2}$	E_0 GeV	E' GeV	θ deg	ε	$\frac{d\sigma}{d\Omega}$ nb/sr	$\Delta\frac{d\sigma}{d\Omega}$ nb/sr	$\Delta\frac{d\sigma}{d\Omega}$ %
0.2726	7.00	0.4489	0.3036	90.000	0.3170	2.3660E+01	7.3346E-01	3.1
0.2726	7.00	0.4489	0.3036	90.000	0.3170	2.5240E+01	7.8244E-01	3.1
0.3894	10.00	0.5570	0.3495	90.000	0.3105	1.2020E+01	3.7262E-01	3.1
0.5841	15.00	0.7180	0.4068	90.000	0.3002	4.8720E+00	2.0462E-01	4.2
0.5841	15.00	0.7180	0.4068	90.000	0.3002	4.8060E+00	1.6340E-01	3.4
0.7788	20.00	0.8651	0.4501	90.000	0.2905	2.1560E+00	7.7616E-02	3.6
0.7671	19.70	1.1051	0.6963	59.900	0.5529	5.9570E+00	2.0850E-01	3.5
1.1253	28.90	1.1077	0.5080	90.000	0.2748	7.0200E-01	3.3696E-02	4.8
1.7522	45.00	1.5975	0.6637	80.000	0.3217	2.0320E-01	1.0770E-02	5.3

Table D.12 – Cross sections and kinematics from Price, *et al.*, from reference [48]

Q^2 $(\mathrm{GeV/c})^2$	Q^2 $(\mathrm{fm})^{-2}$	E_0 GeV	E' GeV	θ deg	ε	$\frac{d\sigma}{d\Omega}$ nb/sr	$\Delta\frac{d\sigma}{d\Omega}$ nb/sr	$\Delta\frac{d\sigma}{d\Omega}$ %
0.6700	17.21	4.0980	3.7410	12.000	0.9744	3.3730E+02	6.4087E+00	1.9
0.6701	17.21	0.8047	0.4476	86.000	0.3257	3.4240E+00	9.2448E-02	2.7
1.0002	25.69	5.0580	4.5250	12.000	0.9724	1.2130E+02	2.5473E+00	2.1
1.0021	25.74	1.0480	0.5140	86.000	0.3092	1.1290E+00	3.2741E-02	2.9
1.1690	30.02	5.2870	4.6641	12.500	0.9690	6.8200E+01	1.2958E+00	1.9
1.1690	30.02	1.1370	0.5141	90.000	0.2729	6.2040E-01	1.6751E-02	2.7
1.1673	29.98	1.1620	0.5400	86.000	0.3016	6.7800E-01	1.6950E-02	2.5
1.5005	38.54	6.2730	5.4734	12.000	0.9695	3.3710E+01	6.7420E-01	2.0
1.5007	38.54	1.3830	0.5833	86.000	0.2873	2.8390E-01	9.6526E-03	3.4
1.7505	44.96	6.5610	5.6282	12.500	0.9653	1.7370E+01	4.1688E-01	2.4
1.7508	44.96	1.5120	0.5790	90.000	0.2504	1.4470E-01	4.6304E-03	3.2
1.7525	45.01	1.5440	0.6101	86.000	0.2774	1.5990E-01	3.9975E-03	2.5
2.0002	51.37	6.3600	5.2941	14.000	0.9549	8.4420E+00	1.7728E-01	2.1
2.0006	51.38	1.6990	0.6329	86.000	0.2683	9.4410E-02	2.6435E-03	2.8
2.0006	51.38	1.6990	0.6329	86.000	0.2683	9.5610E-02	2.2946E-03	2.4
2.3306	59.85	6.5020	5.2600	15.000	0.9455	4.0480E+00	1.0525E-01	2.6
2.3307	59.86	1.9010	0.6590	86.000	0.2571	5.2850E-02	1.6912E-03	3.2
2.3356	59.98	1.9040	0.6594	86.000	0.2569	4.9540E-02	1.2880E-03	2.6
3.0004	77.05	6.4980	4.8991	17.660	0.9180	1.0070E+00	2.1147E-02	2.1
3.0003	77.05	2.3000	0.7012	86.000	0.2369	1.6980E-02	6.6222E-04	3.9
3.0003	77.05	2.3000	0.7012	86.000	0.2369	1.7030E-02	4.5981E-04	2.7

Table D.13 – Cross sections and kinematics from Bartel, 1973, *et al.*, from reference [3]

Q^2 $(\mathrm{GeV/c})^2$	Q^2 $(\mathrm{fm})^{-2}$	E_0 GeV	E' GeV	θ deg	ε	$\frac{d\sigma}{d\Omega}$ nb/sr	$\Delta\frac{d\sigma}{d\Omega}$ nb/sr	$\Delta\frac{d\sigma}{d\Omega}$ %
0.9990	25.66	3.9960	3.4636	15.440	0.9549	6.5900E+01	1.2000E+00	1.8
1.4987	38.49	6.1970	5.3984	12.150	0.9687	3.3060E+01	5.9000E-01	1.8
1.9983	51.32	6.1970	5.1321	14.400	0.9524	8.2900E+00	1.7000E-01	2.1
2.5011	64.23	7.9090	6.5762	12.590	0.9600	4.7550E+00	7.6000E-02	1.6
3.7557	96.45	9.9930	7.9916	12.450	0.9531	9.4800E-01	1.9000E-02	2.0
5.0751	130.34	10.7000	7.9955	13.990	0.9315	1.8560E-01	4.0000E-03	2.2
9.9839	256.40	13.3300	8.0097	17.590	0.8449	3.6200E-03	1.4000E-04	3.9

Table D.14 – Cross sections and kinematics from Kirk, *et al.*, from reference [13]. Only selected Q^2 values are included.

Q^2 $(\mathrm{GeV/c})^2$	Q^2 $(\mathrm{fm})^{-2}$	E_0 GeV	E' GeV	θ deg	ε	$\frac{d\sigma}{d\Omega}$ nb/sr	$\Delta\frac{d\sigma}{d\Omega}$ nb/sr	$\Delta\frac{d\sigma}{d\Omega}$ %
2.8830	74.04	5.4830	3.9467	21.031	0.8886	7.9400E-01	2.7500E-02	3.5
3.6460	93.63	5.4830	3.5401	25.031	0.8329	1.9200E-01	7.2100E-03	3.8
5.0280	129.13	7.6400	4.9606	20.987	0.8572	6.9200E-02	2.2200E-03	3.2
5.0080	128.61	6.6760	4.0073	24.988	0.8079	4.5100E-02	1.5700E-03	3.5
5.0320	129.23	5.5070	2.8255	33.039	0.7006	2.0400E-02	7.6200E-04	3.7
7.3340	188.35	9.6250	5.7168	21.036	0.8247	1.0800E-02	4.5000E-04	4.2
9.6560	247.98	11.4700	6.3244	21.022	0.7951	2.5100E-03	1.0000E-04	4.0

Table D.15 – Cross sections and kinematics from Sill, *et al.*, from reference [50]. Only selected Q^2 values are included.

Q^2 $(\mathrm{GeV/c})^2$	Q^2 $(\mathrm{fm})^{-2}$	E_0 GeV	E' GeV	θ deg	ε	$\frac{d\sigma}{d\Omega}$ nb/sr	$\Delta\frac{d\sigma}{d\Omega}$ nb/sr	$\Delta\frac{d\sigma}{d\Omega}$ %
0.4900	12.58	0.5041	0.2430	180.000	0.0000	2.4967E+00	4.4398E-02	1.8
0.6200	15.92	0.5921	0.2618	180.000	0.0000	1.4206E+00	2.3288E-02	1.6
0.8300	21.32	0.7275	0.2852	180.000	0.0000	6.3371E-01	1.0190E-02	1.6
1.0100	25.94	0.8391	0.3009	180.000	0.0000	3.5682E-01	8.2186E-03	2.3
1.0800	27.74	0.8817	0.3062	180.000	0.0000	2.9407E-01	6.0238E-03	2.0
1.1700	30.05	0.9360	0.3125	180.000	0.0000	2.1422E-01	3.5357E-03	1.7
1.2300	31.59	0.9719	0.3164	180.000	0.0000	1.8051E-01	5.5809E-03	3.1
1.3100	33.64	1.0194	0.3213	180.000	0.0000	1.4337E-01	2.6420E-03	1.8
1.4600	37.49	1.1076	0.3296	180.000	0.0000	9.7431E-02	1.8611E-03	1.9
1.6000	41.09	1.1890	0.3364	180.000	0.0000	6.8208E-02	1.2449E-03	1.8
1.7500	44.94	1.2755	0.3430	180.000	0.0000	4.8225E-02	9.2033E-04	1.9

Table D.16 – Cross sections and kinematics from Katramatou, *et al.*, from reference [54]

References

[1] J. D. Bjorken, S. D. Drell, *Relativistic Quantum Mechanics*, (1964)

[2] F. Halzen, A. D. Martin, *Quarks and Leptons*, (1984)

[3] W. Bartel, *et al.*, Nuclear Physics **58**, 429 (1973)

[4] W. Albrecht, *et al.*, Phys. Rev. Lett. **18**, 1014 (1967)

[5] SLAC proposal E140, *A Proposal to Measure the* x *and* Q^2 *Dependence of* $R=\sigma_L/\sigma_T$ (1984)

[6] S. Dasu, *et al.*, Phys. Rev. Lett. **61**, 1061 (1988)

[7] S. Dasu, *et al.*, Phys. Rev. Lett. **60**, 2591 (1988)

[8] R. B. Neal, *The Stanford Two-Mile Accelerator*, (1968)

[9] NPAS Users Guide, SLAC-269, UC-28, (1984)

[10] J. Mark, *Advances in Cryogenic Engineering* v. 30, Plenum, New York (1984)

[11] S. Dasu, PhD thesis, University of Rochester (1988)

[12] See, for example, L. Mo and C. Peck, SLAC-TN-65-29, (1965)

[13] P. N. Kirk, *et al.*, Phys. Rev. **D8**, 63 (1973)

[14] D. H. Coward, *et al.*, Phys. Rev. Lett. **20**, 292 (1968); see also ref. [13]

[15] A. F. Sill, *et al.*, SLAC-NPAS-TN-86-1 (1986), and references therein

[16] L. Clogher, *et al.*, SLAC-PUB (in preparation for submission to Nucl. Ins. Meth.)

[17] L.W. Whitlow, PhD thesis, (in preparation), Stanford University

[18] Particle Data Group, *Particle Properties Data Booklet* (1986)

[19] P. Bosted and A. Rahbar, SLAC-NPAS-85-1, (1985)

[20] J. Gomez, *Shower Counter for the SLAC 8 GeV/c Spectrometer*, SLAC-PUB (number unknown) (1984)

[21] J. S. Beale, *et al.*, Nucl. Inst. Meth. **117**, 501 (1974)

[22] S. E. Rock, private communication

[23] A. Bodek and J. L. Ritchie, Phys. Rev. **D23**, 1070 (1981)

[24] L. S. Rochester, *et al.*, Phys. Rev. Lett. **36**, 1284 (1976)

[25] D. H. Potterveld, PhD thesis, California Institute of Technology, (1988)

[26] K. L. Brown, F. Rothacker, D. C. Carey, and Ch. Iselin, SLAC 91, Rev. 2 (1977)

[27] S. Dasu, private communication

[28] G. Höhler, *et al.*, Nucl. Phys. **B114**, 505 (1976)

[29] Y. S. Tsai, Phys. Rev. **122** 1898 (1961)

[30] S. D. Drell and S. Fubini, Phys. Rev. **113**, 741 (1959)

[31] J. Mar, *et al.*, Phys. Rev. Lett. **21**, 482 (1968)

[32] L. W. Mo and Y. S. Tsai, Rev. Mod. Phys. **41**, 205 (1969)

[33] S. E. Rock, private communication

[34] T. Janssens, *et al.*, Phys. Rev. **142**, 922 (1966)

[35] J. Schwinger, Phys. Rev. **76**, 790 (1949)

[36] H. A. Bethe and J. Ashkin, *Experimental Nuclear Physics*, 272 (1953)

[37] W. Bartel, *et al.*, Phys. Rev. Lett. **17**, 608 (1966)

[38] N. Meister and D. R. Yennie, Phys. Rev. **130**, 1210 (1963)

[39] W. Albrecht, *et al.*, Phys. Rev. Lett. **17**, 1192 (1966)

[40] J. Litt, *et al.*, Phys. Rev. **31B**, 40 (1970)

[41] L. Eyges, Phys. Rev. **76**, 264 (1949)

[42] M. Goitein, *et al.*, Phys. Rev. **D1**, 2449 (1970)

[43] J. D. Bjorken, Ann. Phys. (NY) **24**, 201 (1963)

[44] Ch. Berger, *et al.*, Phys. Lett. **35B**, 87 (1971)

[45] Chr. Berger, *et al.*, Phys. Lett. **28B**, 276 (1968)

[46] See eq. C.11 of ref [32]

[47] W. Heitler, *The Quantum Theory of Radiation*, 378 (1954)

[48] L. E. Price *et al.*, Phys. Rev. **D4**, 45 (1971)

[49] D. R. Yenni, S. C. Frautschi, and H. Suura, Ann. Phys. (NY) **13**, 379 (1961)

[50] A. Sill, PhD thesis, The American University (1986)

[51] R. G. Arnold, *et al.*, Phys. Rev. Lett. **57**, 174 (1986)

[52] Y. S. Tsai, SLAC-PUB-848, (1971)

[53] A. T. Katramatou *et al.*, SLAC-PUB-4419 (1987); to be submitted to Nucl. Inst. and Meth.

[54] G. G. Petratos, PhD thesis, The American University (1988)

[55] Y. Nambu, Phys. Ref. **106**, 1366 (1957)

[56] J. J. Sakurai, Ann. Phys. (N.Y.) **11**, 1 (1960)

[57] F. Iachello, A. D. Jackson, and A. Lande, Phys. Lett. **43B**, 191 (1973)

[58] W. R. Frazer and J. R. Fulco, Phys. Rev. **117**, 1609, (1960)

[59] S. J. Brodsky and G. F. Farrar, Phys. Rev. **D11**, 1309 (1975)

[60] M. Gari and W. Krümplemann, Z. Phys. A. **322**, 689 (1973)

[61] S. J. Brodsky and B. Chertok, Phys. Rev. **D14**, 3003 (1976)

[62] S. Rock, *et al.*, Phys. Rev. Lett. **49**, 1139 (1982)

[63] J. Napolitano, *et al.*, Phys. Rev. Lett **61**, 2530 (1988)

[64] G. Höhler and E. Pietarinen, Nucl. Phys. **B95**, 210 (1975)

[65] G. Höhler and E. Pietarinen, Nucl. Phys. **B216**, 334 (1983)

[66] W. Grein and P. Kroll, Nucl. Phys. **A338**, 332 (1980)

[67] U. Kaulfub and M. Gari, Nucl. Phys. **A408**, 507 (1983)

[68] M. Gari and U. Kaulfub, Phys. Lett. **136B**, 139 (1984)

[69] A. V. Radyushkin, Acta Phys. Polo. **B15**, 403 (1984)

[70] V. M. Belyaev and B. L. Ioffe, Zh. Eksp. Teor. Fiz. **83**, 876 (1982)[Sov. Phys. JETP **56**, 493 (1982)]

[71] V. M. Belyaev., Phys. Lett. 127B, 254 (1983)

[72] P. R. Cameron, *et al.*, Phys. Rev. **D32**, 3070 (1985)

[73] M. Anselmino, P. Kroll, and B. Pire, Z. Phys. C. **36**, 89 (1973)

[74] Y. S. Tsai, Rev. Mod. Phys. **46**, 815 (1974)

[75] L. Landau, Journal of Phys., **VIII**, 201 (1944)

[76] W. Bartel, *et al.*, Nucl. Phys. **B37**, 86 (1972); plus references [3,52]

[77] See, for example, ref [76] for a discussion of this effect

[78] This correction is from the computer code DELVAC written by D. Yu. Bardin and is attributed to Burkhard, Tasso Note 192, 1982. The fit was found to be equivalent, in the allowed Q^2 regime, to using quark masses: $M_d = 0.08$, $M_u = 0.08$, $M_s = 0.3$, with the equation for the muon loop contributions weighted by the quark charges and number of colors

[79] J. Schwinger, Phys. Rev. **76**, 790 (1949)

[80] C. Marchand, PhD thesis, L'Université de Paris-SUD, Centre D'Orsay, (1987); in French

[81] A. T. Katramatou, SLAC-NPAS-TN-86-8 (1986)

[82] R. M. Sternheimer and R. F. Peierls, Phys. Rev. **B3**, 3681 (1971)

[83] A. Crispin and G. N. Fowler, Rev. of Mod. Phys. **42**, 290 (1970)

[84] E. J. Moniz, *et al.*, Phys. Rev. Lett. **26**, 445 (1971)

[85] D. B. Day, *et al.*, Phys. Rev. Lett. **59**, 427 (1987)